SPATIO-TEMPORAL VARIABILITY OF AEROSOLS IN THE TROPICS RELATIONSHIP WITH ATMOSPHERIC AND OCEANIC ENVIRONMENTS

A Thesis
Presented to
The Academic Faculty

by

Manuel D. Zuluaga-Arias

In Partial Fulfillment
of the Requirements for the Degree
Doctor of Philosophy in the
School of Earth and Atmospheric Sciences

Georgia Institute of Technology
August 2011

SPATIO-TEMPORAL VARIABILITY OF AEROSOLS IN THE TROPICS RELATIONSHIP WITH ATMOSPHERIC AND OCEANIC ENVIRONMENTS

Approved by:

Dr. Peter J. Webster, Advisor
School of Earth and Atmospheric Sciences
Georgia Institute of Technology

Dr. Carlos D. Hoyos, Co-Advisor
School of Earth and Atmospheric Sciences
Georgia Institute of Technology

Dr. Judith A. Curry
School of Earth and Atmospheric Sciences
Georgia Institute of Technology

Dr. Irina Sokolik
School of Earth and Atmospheric Sciences
Georgia Institute of Technology

Dr. Sharon E. Nicholson
Department of Earth, Ocean and Atmospheric Science
Florida State University

Date Approved: 22 June 2011

To my family

ACKNOWLEDGEMENTS

I would like thank Dr. Peter Webster and Dr. Carlos Hoyos for their innumerable ideas and guidance through the development of this work, and for all the support they provide me in my time at Georgia Tech.

Thanks to the members of my committee for taking the time to read the thesis and for their useful comments and suggestions.

I want to extend my gratitude to my fellow peers, Violeta, Hye-Mi, Fernando, James, Hai-Ru, Mattew and Vincent for the constant help and support.

Thanks to my dear friends; Yuley, Lina, Sara, Paola and Paula for the support and friendship they gave me in all the time not only in Georgia Tech but also in "El Posgrado" in Colombia.

Thanks to Tara, my girlfriend who has become an important part of my life. Thanks for to her for sharing company, support and happiness in the last couple of years.

Thanks to my mom, dad, brothers and sisters for happen to be the most special part of my life and made me what I am right now.

TABLE OF CONTENTS

LIST OF TABLES

LIST OF FIGURES

SUMMARY

Earth's radiation budget is directly influenced by aerosols through the absorption of solar radiation and subsequent heating of the atmosphere. Aerosols modulate the hydrological cycle indirectly by modifying cloud properties, precipitation and ocean heat storage. In addition, polluting aerosols impose health risks in local, regional and global scales. In spite of recent advances in the study of aerosols variability, uncertainty in their spatio-temporal distributions still presents a challenge in the understanding of climate variability. For example, aerosol loading varies not only from year to year but also on higher frequency intraseasonal time scales producing strong variability on local and regional scales. An assessment of the impact of aerosol variability requires long period measurements of aerosols at both regional and global scales.

The present dissertation compiles a large database of remotely sensed aerosol loading in order to analyze its spatio-temporal variability, and how this load interacts with different variables that characterize the dynamic and thermodynamic states of the environment. Aerosol Index (AI) and Aerosol Optical Depth (AOD) were used as measures of the atmospheric aerosol load. In addition, atmospheric and oceanic satellite observations, and reanalysis datasets is used in the analysis to investigate aerosol-environment interactions. A diagnostic study is conducted to produce global and regional aerosol satellite climatologies, and to analyze and compare the validity of aerosol retrievals. We find similarities and differences between the aerosol distributions over various regions of the globe when comparing the different satellite retrievals. A nonparametric approach is also used to examine the spatial distribution of the recent trends in aerosol concentration. A significant positive trend was found

over the Middle East, Arabian Sea and South Asian regions strongly influenced by increases in dust events.

Spectral and composite analyses of surface temperature, atmospheric wind, geopotential height, outgoing longwave radiation, water vapor and precipitation together with the climatology of aerosols provide insight on how the variables interact. Different modes of variability, especially in intraseasonal time scales appear as strong modulators of the aerosol distribution. In particular, we investigate how two modes of variability related to the westward propagating synoptic African Easterly Waves of the Tropical Atlantic Ocean affect the horizontal and vertical structure of the environment. The statistical significance of these two modes is tested with the use of two different spectral techniques. The pattern of propagation of aerosol load shows good correspondence with the progression of the atmospheric and oceanic conditions suitable for dust mobilization over the Atlantic Ocean. We present extensions to previous studies related with dust variability over the Atlantic region by evaluating the performance of the long period satellite aerosol retrievals in determining modes of aerosol variability. Results of the covariability between aerosols-environment motivate the use of statistical regression models to test the significance of the forecasting skill of daily AOD time series. The regression models are calibrated using atmospheric variables as predictors from the reanalysis variables. The results show poor forecasting skill with significant error growing after the 3^{rd} day of the prediction. It is hypothesized that the simplicity of linear models results in an inability to provide a useful forecast.

CHAPTER I

INTRODUCTION

A major challenge for climate science is the accurate representation of the water cycle and the exchange of heat between the atmosphere, the ocean, the land surfaces and space. Both the water cycle and global energy distribution are highly coupled to the large-scale atmospheric circulation pattern, which in turn is strongly modulated by the distribution of clouds and rainfall. Clouds and rainfall influence regional circulations by redistributing energy. The feedbacks between clouds and the large-scale circulation, complicated by the impacts of aerosols on radiation budget and cloud properties, represent one of the largest sources of uncertainty for future climate projections (Stephens 2005). These uncertainties, relating to direct and indirect aerosol effects, remain large owing to high spatial and temporal aerosol load variability and heterogeneous distribution of aerosol species (Kaufman et al. 2002; IPCC 2007). A major thrust of this research is to determine the impact of aerosols in climate.

Atmospheric aerosols refer to solid and liquid particles that are suspended in air. Different types of processes produce aerosols with natural (e.g., wind-blown sea spray, dusts and volcanic debris) and anthropogenic (such as smokes, fumes and pollution) sources that, through mobilization, place aerosols on both the troposphere and the stratosphere. Aerosols modulate the radiation budget and the hydrological cycle both directly and indirectly and, thus, have the potential of playing an important role in weather and climate variability (Ramanathan et al. 2001). Greenhouse gases primarily influence the long-wave radiation budget through absorption and re-radiation, while the primary radiation impact of aerosols is on the incoming and reflected solar radiation stream (Haywood and Boucher 2000). But aerosols also

influence cloud microphysics indirectly impacting both the longwave and solar radiation streams through altering the size and growth rates of clouds. Thus, there are two distinctly different roles that aerosols play in weather and climate.

The first aerosol effect, known as the direct effect, modifies the energy balance of the Earth-Atmospheric system through scattering and absorption of solar radiation. Scattering redistributes the incoming solar energy enhancing the amount of radiation reflected back to space, therefore increasing the atmospheric albedo and cooling the Earths surface (e.g., Charlson et al. 1992). Absorption of both solar and infrared radiation transforms radiative energy into internal energy of the absorbing particles which in turn heats the atmosphere (Haywood et al. 1999). The second aerosol effect, called the indirect aerosol effect, modifies the abundance and properties of clouds by acting as cloud condensation (CCN) and ice nuclei. The droplet number concentration is increased with the amount of aerosols particles available for CCN. This growth in droplet number leads to an increase of cloud reflection, possibly leading to a climate cooling (Twomey 1977; Twomey et al. 1984). Additionally, if the amount of moisture is not altered inside the cloud, the droplet radius will decrease as the aerosol concentration increases resulting in a reduction of the precipitation efficiency. This so-called second indirect radiative forcing (Albrecht 1989), leads in some cases to increases in cloud lifetime and, in turn, the amount of clouds, further increasing the reflection of solar radiation.

Both the direct and indirect aerosol effects induce changes in the energy radiation budget and affect the global circulation and climate. However, there are aerosol related effects that occur on shorter timescale and on regional scales. For example, the reduction in surface solar radiation imposed by aerosols (e.g., from dust plumes) produces a very strong convective suppressing inversion, usually in the lower levels of the atmosphere. The growth of an inversion changes the vertical atmospheric temperature gradient (i.e., cooling the surface and heating the boundary layer), limiting

precipitation throughout stabilization of the air column and reducing surface shortwave radiation (Coakley and Cess 1985; Miller and Tegen 1998; Evan et al. 2009), further affecting the hydrological cycle. Evidence suggests that this aerosol variability could even inhibit the formation and reduce the intensity of tropical cyclone activity (e.g., Dunion and Velden 2004; Lau and Kim 2007).

Aerosol effects are also significant in non-climate related issues, such as those related to local, regional, and global air pollution. Large-scale biomass burning and boreal forest fire events often cast huge smoke plumes thousands of kilometers away from their sources, causing serious air quality and health related problems (Torres et al. 2002). Volcanic ash plumes can interrupt aviation and impose health risks associated with the inhalation of volatile particles (e.g., Gislason et al. 2011). Furthermore, dust aerosols have numerous impacts on the productivity of agriculture and marine biology (e.g., Jickells et al. 2005), and even on visibility disrupting aviation (Westphal et al. 2009).

All the aforementioned aerosol effects occur on different time and spatial scales. An assessment of the impact of aerosol variability effects on the radiation and hydrological cycles requires long period measurements of aerosols at both regional and global scales. With the use of the absorbing aerosol detection in the ultraviolet wavelength by the Total Ozone Mapping Spectrometer (TOMS) and Ozone Monitoring Instrument (OMI), flying on several platforms since 1978, it had become possible to compile a long-term aerosol record. Although the TOMS-OMI instruments were designed originally for remote sensing of ozone, they have been used to monitor absorbing aerosol transport over land and ocean (Herman et al. 1997). The global features of aerosol distribution using the TOMS-OMI satellite platforms have been used extensively to document aerosol variability and its effects on climate (e.g., Torres et al. 1995; Prospero et al. 2002; Jeong and Li 2005; Lau and Kim 2006; Torres et al. 2007; George et al. 2008; Tian et al. 2008; Li et al. 2009).

More recently, the TOMS/OMI data has been complemented by the launch to the space of the Moderate Resolution Imaging Spectroradiometer (MODIS) and the Multiangle Imaging Spectroradiometer (MISR) sensors that were designed specifically for aerosol retrievals. The information provided by these two platforms have expanded the near-infrared aerosol detection to include non-absorbing aerosols and several others aerosol properties with greater accuracy (Remer et al. 2005; Diner et al. 1998). MODIS data has expanded the global aerosol depiction with the ability of size detection (Remer et al. 2008), while MISR aerosol retrievals supplement MODIS observations by incrementing the accuracy in aerosol properties, especially over land (Kalashnikova and Kahn 2006). The global aerosol picture is complemented with the launch in 2006 of the Cloud-Aerosol Lidar and Infrared Pathfinder Satellite Observations (CALIPSO) which is an aerosol lidar profiler able to retrieve columnar aerosol type and load (Winker et al. 2003).

Global and regional climatologies have been produced mainly using TOMS (e.g., Hsu et al. 1996; Herman et al. 1997; Seftor et al. 1997; Chiapello et al. 1999; Cakmur and Miller 2001; Prospero et al. 2002; Torres et al. 2002; Torres et al. 2005; Gao and Washington 2009; Li et al. 2009) and MODIS (e.g., Hongbin et al. 2003; Remer et al. 2008; Papadimas et al. 2008; Liu and Mishchenko 2008; Mishchenko et al. 2009; Torres et al. 2010; Zhang and Reid 2010) satellite based aerosol information to provide an overall depiction of the global sources and the aerosol spatial and temporal distribution. Two main products from these platforms have been used to characterize aerosol distribution: TOMS-Aerosol Index as a qualitative measure of the amount of absorbing aerosols from mineral dust, biomass burning and volcanic ash present on the atmosphere and MODIS-Aerosol Optical Depth as a quantitative measure of the transparency of the column integrated aerosol content across the atmosphere. A more descriptive definition with benefits and shortcomings in these two aerosol

datasets is explained in more detail in Chapter 2. All this datasets produced a qualitatively similar view of the Earths aerosol system. However, quantitative analysis reveals significant differences in mean aerosol optical depth and other aerosol parameters retrieved from satellite (Mishchenko et al. 2007; 2009). Resolving quantitative differences between satellite-derived aerosol products is an ongoing challenge for the research community (Remer et al. 2008).

Some studies have also used satellite aerosol retrievals and numerical model simulations to explain the interannual and intraseasonal variability of aerosol distributions and their relationship with the large-scale circulation and the global climatology. For example, Karyampudi et al. (1999) used Meteosat satellite overpasses and reanalysis data to describe a detailed synoptic situation for the conditions suitable for dust mobilization in the Tropical Atlantic Ocean. This analysis validated many of the characteristic features of the Saharan dust plume conceptual model (Carlson and Prospero 1972) describing how an aerosol dust layer emerges from West Africa within a series of large-anticyclonic eddies and how this layer is elevated to mid-levels of the atmosphere. However, Karyampudi et al. study was based on a single week of data, limiting the characterization of the time-scale variation of the phenomena. Huang et al. (2010) using five years of MODIS and CALIPSO data, characterized the properties of evolution of major aerosol outbreaks associated with Saharan dust mobilization. This study identified pathways of dust and their relationship with winds and humidity, characterizing a westward propagation speed of 1000 km/day of dust disturbances. Some others (e.g., Knippertz and Todd 2010; Jury and Santiago 2010) have used TOMS, MODIS and reanalysis data to characterize the role of synoptic African disturbances (i.e., African Easterly Waves, Burpee 1972) in generating desert dust from North Africa and transporting it across the Atlantic. Their work confirmed some key features (e.g., westward propagation with alternating geopotential height anomalies) of the conceptual model of the Saharan dust plume and how the plume propagates

with a speed of about 800 km/day (i.e., similar speed than a climatological African Easterly Wave).

In the present study, we have compiled a large database of remotely sensed aerosol loading in order to analyze its spatio-temporal variability, and how this load interacts with different variables that characterize the dynamic and thermodynamic states of the environment. We used different satellite retrievals to characterize the longest records of aerosol distribution in tropical regions. The diversity of this database relies on the different satellite product retrieval technique and calibration procedure that provide a synergistic approach to complement the analysis. In addition, we have used the European Centre for Medium-Range Weather Forecasts (ECWMF) reanalysis dataset and satellite observations of oceanic and atmospheric data to investigate aerosol-environment interaction. A description of the aerosol datasets and oceanic/atmospheric information used throughout the document is presented in Chapter 2. A diagnostic study, presented in Chapter 3, was conducted to produce an aerosol satellite climatology using the TOMS, OMI, MODIS and MISR datasets to analyze and compare the validity of aerosol satellite retrievals. The climatology includes a comparison of aerosol time series over different regions of the globe, reporting their annual and seasonal cycles. Chapter 3 includes an analysis of the global spatial distribution of aerosol trends based on longest available satellite datasets.

In Chapter 4, we investigate how atmospheric processes modify the aerosol load over the Tropical Atlantic region and how the environment, in turn, is impacted by the aerosol variability. We focus the analysis on the spectral representation of the maximum aerosol load events as retrieved by the satellite datasets. With this type of analysis we present some extensions to previous studies in this matter (e.g., Karyampudi et al. 1999; Huang et al. 2010; Knippertz and Todd 2010; Jury and Santiago 2010). We aim to evaluate the performance of the long series of satellite aerosol retrievals into the determination of the different modes of variability that

aerosol load presents over the Tropical Atlantic region. We also use reanalysis and satellite observations of atmospheric and oceanic variables to show how two modes of variability (i.e., in relation with African Easterly Waves activity) of the aerosol events affect the horizontal and vertical structure of the environment and how those impacts are represented in the proposed models for aerosol variability over the Atlantic Ocean (e.g., Carlson and Prospero 1972). The analysis is complemented with the study of CALIPSO overpasses that help to characterize the vertical extent of the aerosol maxima over the region.

The results presented in Chapter 4 suggest the existence of coherent evolution pattern between the aerosol load and the dynamics of the atmosphere and ocean. We use the connections found in Chapter 4 to construct different forecasting models based on statistical relationships between aerosols and atmospheric variables. Chapter 5 presents different tests conducted to estimate the predictive skill of the forecasting models of aerosol load. A brief summary and conclusions are included in Chapter 6. A sensitivity analysis of the sampling patterns of MODIS aerosol retrievals is presented in Appendix A. The validity of the aerosol modes of variability found in Chapter 4 was tested using an alternative technique to the spectral analysis and is presented in the Appendix B.

CHAPTER II

DATA

Datasets used in this study include a compilation of seven satellite derived aerosol products and numerical climatic reanalysis information. Additional oceanic and atmospheric data were obtained from satellite observations. Aerosol datasets includes information from the TOMS-Nimbus 7, TOMS-Earth Probe, OMI, MODIS-Terra, MODIS-Aqua, MISR and CALIPSO satellite missions. Atmospheric variables from the ECMWF reanalysis, sea surface temperature (SST), outgoing longwave radiation (OLR), rainfall intensity and water vapor were also compiled in order to relate aerosol distributions with the circulation and thermodynamic state of atmosphere and ocean. The following paragraphs describe in detail the definitions, sources and capabilities of each of this datasets.

2.1 Aerosol Data

2.1.1 TOMS-OMI Aerosol Index

The TOMS-OMI Aerosol Index (AI), one of the longest aerosol records available, is a measure of the amount of backscattered UV radiation from an atmosphere containing aerosols (i.e., observations) differs from the backscatter of a pure molecular atmosphere (i.e., model calculations) (Herman et al. 1997). The approach to retrieve aerosol properties using TOMS-OMI measurements in the UV spectral region is based on the measurement of the backscattered radiance at two wavelengths in the range of 330–380 nm. For a more detail in the computation of the AI the reader is referred to read Torres el al. 1998; 2005. The AI is proportional to the aerosol optical thickness and is mostly sensitive to the aerosol absorption, particle size, aerosol vertical distribution and clouds. The AI is positive for absorbing aerosols such as mineral dust,

elevated biomass burning smoke, and volcanic ash. However, the AI cannot detect non-absorbing aerosols such as sea salt and sulfates. The AI has aerosol detection capabilities over all types of land and ocean surfaces although it is affected by sub-pixel cloud contamination and by the altitude of the aerosol layer, as it is incapable of detecting absorbing aerosols below elevations of 2 km (Herman et al. 1997). Although the AI is a qualitative characteristic, it is helpful in identifying dust sources and transport routes (Sokolik et al. 2001).

The TOMS-OMI data used in this study is the most recently reclassified and recalculated version (Version 8). The dataset is composed of an ensemble of daily records from three satellite mission retrievals namely: Nimbus 7 (N7T, 1978–1993), Earth Probe (EP, 1996–2005) and OMI satellite (2004–2009). Periods of data from 2000–2005 for EP and 2008–2009 for OMI were removed from the AI records. Data was removed because EP present a calibration drift produced by sensor degradation affecting the retrieval (Kiss et al. 2007) and because OMI present an obstruction in the sensors field of view causing stripes of bad data (see http://macuv.gsfc.nasa.gov/, 2010 for details). In addition, AI values less than 0.5 are treated as missing values because contamination of the variable by sea-glint and water-leaving radiances (O. Torres 2009, personal communication). The entire compilation of TOMS-OMI AI was obtained from the NASA Atmospheric Composition web page (http://macuv.gsfc.nasa.gov/) covering the tropical band between 45°N and 45°S in a 1° x 1.25° latitude-longitude resolution.

2.1.2 MODIS Terra and Aqua Aerosol Optical Depth

Aerosol optical depth (AOD) data from MODIS sensor aboard the NASA Earth Observing System (EOS) Aqua and Terra platforms were used. The AOD is a measure of the transparency of an atmosphere containing aerosols and can be compared to the amount of aerosols in the atmosphere. The retrieval of AOD from MODIS sensor

is done with three independent algorithms using seven of the sensor spectral bands between 0.47 and 2.130 μm that are sensitive to aerosol content in the atmospheric column. The first two algorithms are based on the "dark target" approach and were designed to retrieve AOD over ocean and non-bright land surfaces (Kaufman et al. 1997; Tanré et al. 1997). The latter, called "Deep Blue", is able to retrieve AOD over bright land surfaces (Hsu et al. 2004). Whereas TOMS-OMI AI is only capable of retrieving absorbing aerosols, MODIS AOD measurements are sensitive to both absorbing and non-absorbing aerosols. In addition, MODIS sensors are capable of providing additional and much more accurate aerosol properties (i.e., scattering angle, Angstrom exponent, etc) because it uses a multiple wavelength retrieval technique and cloud masking procedures (Remer et al. 2005).

This work use two sets of MODIS data downloaded from the NASA Atmosphere Archive and Distribution System (LAADS, http://ladsweb.nascom.nasa.gov/). We retrieved daily and monthly AOD data at 0.55 μm for February 2000 to December 2009 from the Terra platform (MOD08_D3 version 5) and for July 2002 to December 2010 from the Aqua platform (MYD08_D3 version 5.1). The data covers the entire globe at an equal-angle latitude-longitude grid with a horizontal resolution of 1° x 1°. In order to use the most recent, advanced and available MODIS AOD data we utilized the "dark target" algorithms for ocean and land regions within the Terra dataset, whereas the "dark target" for oceanic regions and the "Deep Blue" for land regions within the Aqua datasets.

2.1.3 MISR Aerosol Optical Depth

Additional AOD data was retrieved from the MISR sensor mounted on the EOS-Terra satellite to complement the analysis. The MISR sensor comprises a set of nine cameras placed at different angles pointed to the earth surface enhancing the aerosol properties recognition, in special for sun glint areas (Kahn et al. 2009). The MISR

instrument acquires measurements at four spectral resolution bands between 0.44 to 0.87 μm. The aerosol retrieval is based on prescribed lookup tables of forward radiative calculations that are then compared with the MISR observations to determine AOD and other properties (Diner et al. 1998). While MODIS provides information on aerosol concentrations with approximately 2-day global coverage, MISR repeats coverage every 7 to 9 days. This lengthy cycle limits the use of MISR data for high temporal analysis, but the high accuracy of the retrieved data over bright deserts provides the necessary additional synergistic information to supplement the study.

The MISR AOD data was obtained in monthly resolution from NASA Atmospheric Science Data Center (http://eosweb.larc.nasa.gov/) at a 0.5° x 0.5° spatial resolution with global coverage from February 2000 to December 2009.

2.1.4 CALIPSO Aerosol Extinction Coefficient

The nadir-pointing lidar system of the Cloud-Aerosol Lidar and Infrared Pathfinder Satellite Observations (CALIPSO) platform was used to provide a view of the vertical structure of atmospheric aerosol loading. The two-wavelength polarization-sensitive lidar is able to provide vertical profiles of aerosol extinction coefficient at 0.532 μm. This extinction coefficient can be used as a measure of atmospheric vertical distribution of aerosol loading. Details on the CALIPSO science products are given by Winker et al. (2009).

The CALIPSO aerosol profiles are retrieved on a single 5-km along-track horizontal and multiple 60-m vertical resolutions up to 200 hPa. Despite this very high vertical resolution, CALIPSO provides transects of the vertical distribution of aerosols over an approximately 2000–2500 km horizontal interval at mid-latitudes which makes it difficult to capture the continuous spatial structure of the vertical distribution of aerosols. Aerosol extinction coefficient profiles (Lidar level 2 version 3.1) at different times of the day from June 2006 to July 2009 were acquired from the NASA

Atmospheric Science Data Center (http://eosweb.larc.nasa.gov/).

2.2 Atmospheric and Oceanic Data

Three-dimensional hourly data for zonal, meridional and vertical wind components, along with geopotential height, potential temperature, and specific humidity were obtained from the European Center for Medium-Range Weather Forecasts (ECMWF). Both reanalysis datasets ERA40 (Uppala et al. 2005) and ERA interim (Berrisford et al. 2009) were used to characterize large-scale atmospheric circulation. Specifically, 12:00 local time data was archived to match the satellite overpass (i.e., TOMS-MODIS platforms). Data at 1° x 1° horizontal resolution and at seven atmospheric levels from 1000 hPa to 200 hPa were used. These two reanalysis datasets were used separately to cover the TOMS and MODIS periods from July 1978 to July 1993 for the first set of aerosol products and from January 2002 to December 2009 for the second set.

This study also employed daily SST data from the National Oceanic and Atmospheric Administration (NOAA) Optimum Interpolation (OI) dataset version 1.0. These data were obtained from the NOAA NCDC website and correspond to daily SST analysis on a 0.25° latitude-longitude grid (re-interpolated to 1° x 1° to match the grid in aerosol datasets). SST data is computed based on the AVHRR satellite and in situ observations from ships and buoys (Reynolds et al. 2007). In conjunction with SST, interpolated daily OLR data at a 2.5° x 2.5° global grid resolution (Liebmann and Smith 1996) were downloaded from the Climate Diagnostics Center (CDC) from the NOAA ESRL web page (http://www.esrl.noaa.gov/). These SST and OLR datasets were compiled for each of the periods of TOMS and MODIS datasets.

In addition, both the MODIS Near-Infrared Total Precipitable Water Vapor column over clear-sky (Gao and Kaufman 2003), and the daily rainfall intensity from the Global Merged Precipitation analysis (GPCP; Huffman et al. 2001) of the Global Energy and Water Cycle experiment (GEWEX, www.gewex.org/gpcp.html) were used

in this study. Because of the limited period covered by the water vapor and rainfall datasets (i.e., from 2002 to 2010), only data collocated over the MODIS Aqua period with a horizontal resolution of 1° x 1° were used.

CHAPTER III

CLIMATOLOGY OF AEROSOLS: A SATELLITE PERSPECTIVE

3.1 Global Aerosol Distribution

Satellite observations are one of the most efficient ways of producing global aerosol climatologies because they can deliver continuous, homogeneous and globally available datasets, in comparison with studies using surface-based networks of aerosol measurements (e.g., Holben et al. 2001). Measures of aerosol loading retrieved using passive sensors on board satellites have been available since the late 1970s. Early studies using the Advanced Very High Resolution Radiometer (AVHRR, Husar et al. 1997) and the TOMS Nimbus 7 datasets gave the first global distribution of aerosol optical depth. Modern satellite sensors including OMI, MODIS and MISR have also been used to complement the global and regional view of aerosols, their sources and seasonal distributions (Yu et al. 2003; Jeong and Li 2005; Remer et al. 2008; Li et al. 2009; Kahn et al. 2005).

Figure 1 shows model simulation results of dominant aerosol sources across the globe for December–February (DJF) and June–August (JJA) (Chin et al. 2004; Aerosol Center, NASA, http://aerocenter.gsfc.nasa.gov/). During most of the year, the tropical Atlantic Ocean, North Africa and Middle East are affected by desert dust; while Central and East China and the east coast of North America are affected by aerosols derived from industries and pollution. Meanwhile, the Amazon and South African regions experience seasonal aerosol production by biomass burning during the JJA season. A region with a particularly strong seasonal aerosol distribution is south Asia, affected by almost every type of aerosol during different times of the

year. Contrasting Figure 1, Figure 2 presents a depiction of the seasonal distribution of aerosols as seen by some of the available remote sensing platforms. The Figure 2 is constructed averaging monthly data for DJF and JJA seasons of AI and AOD as seen by TOMS-N7T from 1978 to 1993 and MODIS-Aqua from 2002 to 2010, respectively. The distribution of maximum values of aerosols over the globe bears a close resemblance to the location of main aerosol sources shown in Figure 1, especially for those regions affected by dust and biomass burning. Regions where urban and industrial pollution appears in Figure 1 are scarcely represented in Figure 2. Those differences are going to be explored in more detail in subsequent paragraphs.

Both TOMS AI and MODIS AOD show similar distributions of aerosol loading over the Eastern Tropical Atlantic, South Africa, Middle East and South Asia (Figure 2). The most striking characteristic is the presence of a region, spanning from West Africa towards the Tropical Atlantic Ocean with the highest AI and AOD values during JJA. This region is highly affected by dust outbreaks from the Saharan desert and is usually referred to as the "dust corridor" (Prospero and Carlson 1972). The structural features of this dusty region have been illustrated in the Saharan Air Layer (SAL) model proposed by Prospero and Carlson (1972). Aerosol distribution over the Middle East, Arabian Sea and the South Asian region also peaks during the boreal summer. During the pre-monsoon season, air masses carry dust particles towards the Arabian Sea and the Indo-Gangetic Plains where they accumulate and interact with the large flux of regional pollutants and biomass burning aerosols (Ramanathan et al. 2001; Bollasina et al. 2008). The burning of tropical savannas also emits large amounts of carbonaceous particles resulting in a peak in AI and AOD during DJF season over central Africa and Gulf of Guinea (Eva and Lambin 1998; Yu et al. 2003).

The greatest difference in aerosol distribution between both the AI and AOD datasets is seen over South Asia and Eastern China. The high diversity of aerosols

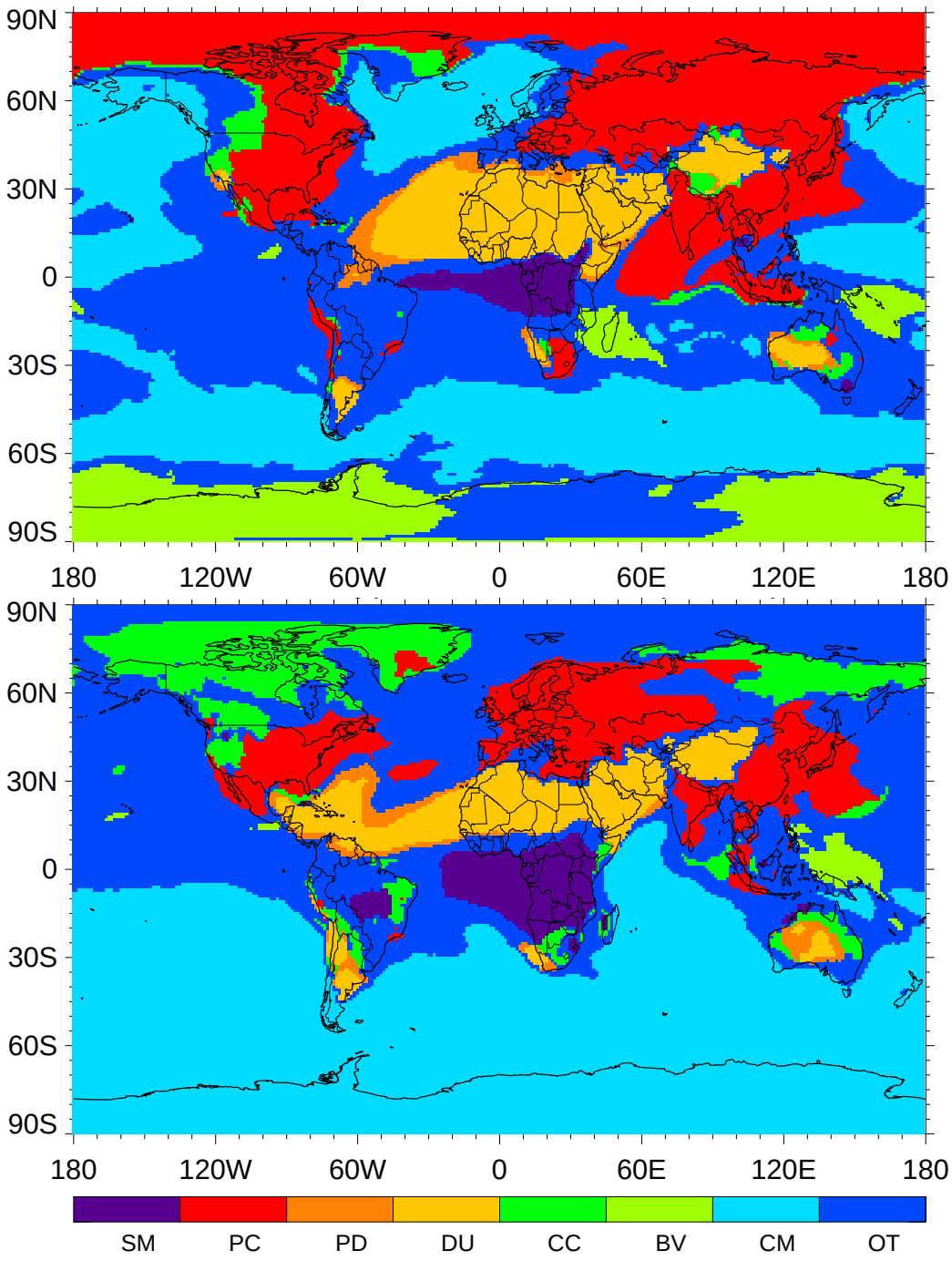

Figure 1: Global distribution of dominant aerosol types during December–February (top) and June–August (bottom) seasons. The distribution is derived from the Goddard Ozone Chemistry Aerosol Radiation and Transport (GOCART) model simulations of monthly AOD. The letters on the caption correspond to smoke (SM), polluted continental (PC), polluted dust (PD), dust (DU), clean continental (CC), biogenic or volcanic (BV), clean marine (CM) and other (OT) (Figure courtesy of M. Chin).

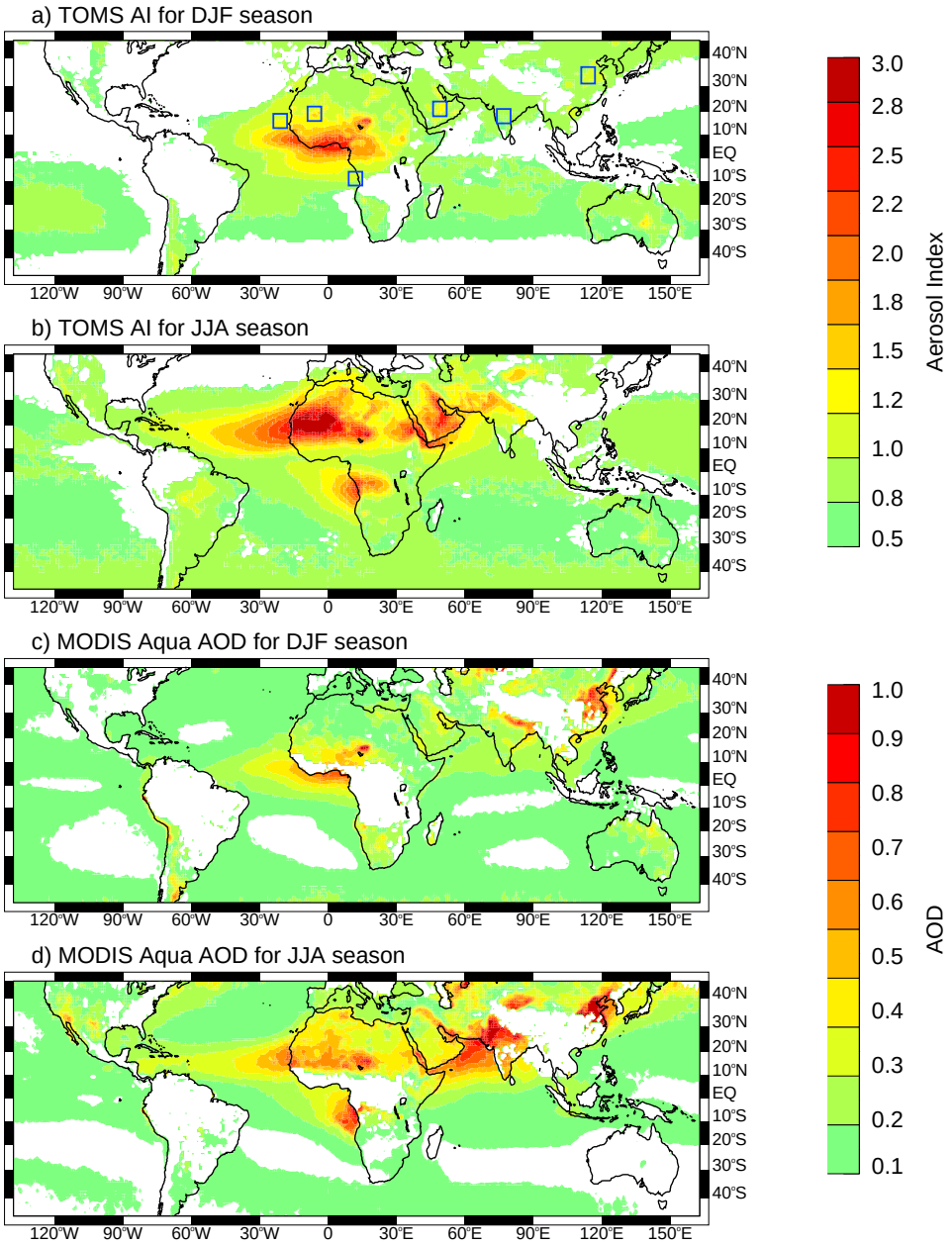

Figure 2: December–February and June–August seasonally averaged AI from TOMS Nimbus 7 (a, b) and AOD from MODIS Aqua (c, d) datasets, respectively. Shading is relative to the scale bar at the right of figures. The TOMS data was averaged for 1978–1993 and the MODIS Aqua for 2002–2010 periods. The blue boxes in (a) correspond to selected regions for regional comparisons.

affecting the region (i.e., atmospheric smoke from coal consumption, dust from surrounding deserts and industrial pollution) is perhaps why the datasets do not agree. While AI from TOMS is only sensitive to absorbing aerosols (e.g., dust and biomass

burning), AOD from MODIS is sensitive to absorbing and non-absorbing (e.g., pollution) aerosols (Torres et al. 2002; Remer et al. 2005). Furthermore, large regions of the globe are left blank in these climatologies because of poor retrieval, including missing values caused by cloud contamination, sun glint (over oceans), or other unsuitable surfaces.

Another striking characteristic that can be seen in Figure 2 is a pronounced asymmetry in latitudinal distribution of aerosols between the Northern and Southern Hemispheres. Figure 3 shows longitudinal zonally-averaged AI and AOD using TOMS-N7T, OMI and MODIS Aqua and Terra datasets for the different time spans of each platform. All datasets agree that the Northern hemisphere has a higher AI than the Southern hemisphere, even considering the difference in retrieval technology and data period used. There are generally three reasons for this asymmetry: 1) the Northern hemisphere has a lower water-to-land ratio than the Southern hemisphere, 2) the worlds largest deserts are located in the Northern hemisphere, and 3) the Northern hemisphere comprises most of the worlds major industrialized countries (Kishcha et al. 2007). Of particular interest is the peak in AI around 20°N and a broad maximum region shown by AOD from MODIS platforms from 10°N to 40°N. The peak in AI is produced by the location of absorbing aerosols from the desert belt located near this latitude. The broad peak in AOD is also related with aerosols produced by deserts but additionally those values are affected by mixture of aerosols (i.e., absorbing and non-absorbing) over South Asia, East China and North America, which are not retrieved by the AI.

Despite the generally reasonable qualitative agreement between aerosol retrievals from satellites (e.g., Jeong and Li 2005), there has been a slow progress to reconcile the quantitative differences in global aerosol climatologies made using these satellite products (Mishchenko et al. 2007). The factors involved not only include the retrieval

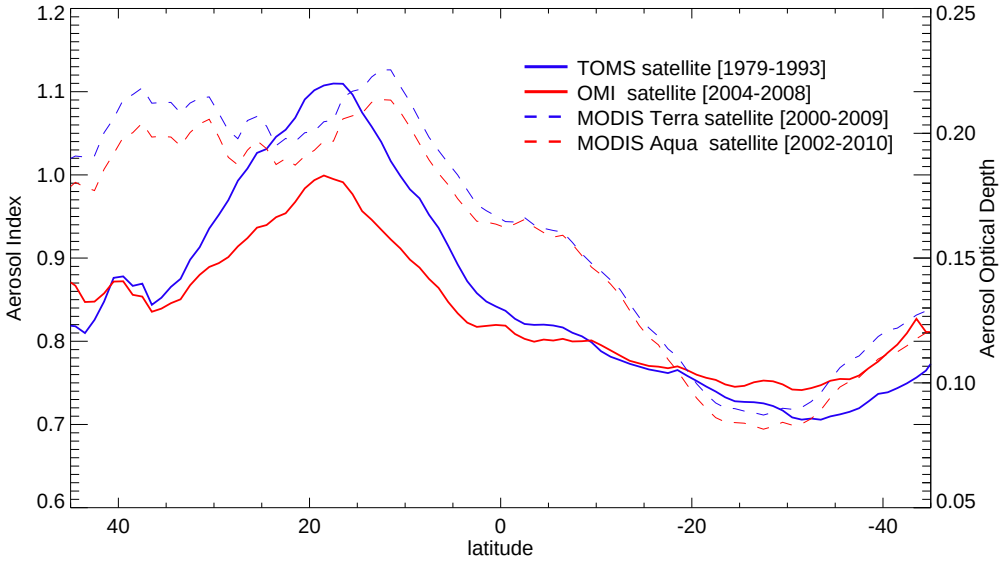

Figure 3: Latitudinal distribution of AI (solid lines) and AOD (dash lines) averaged over all longitudes for the aerosol datasets and time period presented in the inside caption. Notice the different $y-$axis in the diagram for AI and AOD.

technique (i.e., differences between AI and AOD) but also differences in cloud masking, treatment of surface boundary conditions, assumptions of aerosol microphysical properties and instrument calibration between the same type of sensor (Li et al. 2009). This diversity in the retrieval technologies used to detect aerosols in the atmosphere has produced gaps among datasets (Torres et al. 2002; Kiss et al. 2007; Mishchenko et al. 2007). The climatology presented in this work does not try to reconcile these issues; rather, it uses the strength of each dataset to provide a general picture of how aerosols vary across different regions around the world. Analyses performed in this study were done individually for each satellite dataset, taking into account the sensor used (i.e., MODIS-TOMS-MISR), the type of aerosol retrieved (e.g., absorbing, non-absorbing) and the length of the time series.

3.2 Regional time series comparisons

In this study, we have selected six regions (blue boxes in Fig. 2) to compare the spatio-temporal variability of aerosol distributions provided by the aerosol datasets. The AI

and AOD time series show high interannual and intraseasonal variability, with a strong annual cycle over the North and South Africa and Middle East regions (Figure 4). Dust outbreaks originating from the Saharan desert during the boreal spring provide the necessary amount of aerosol to produce large values of AI. Of particular interest is how the AI and AOD in Figure 4 for the common period between November 2004 and December 2008 are notably similar over the Tropical Atlantic Ocean, Middle East and South Africa, but not so similar over South Asia and East China.

Table 1 shows correlation coefficients calculated between OMI AI and MODIS Terra, Aqua and MISR AOD for the common data period. High correlations ($\sim 90\%$) are seen for the Tropical Atlantic Ocean, Middle East and South Africa and low values ($< 60\%$) for the East China and South Asia regions. Regions with high correlation correspond to areas affected mostly by dust and biomass burning. Regions with low correlation among datasets, such as East China, are often affected by a diverse set of aerosols (see Fig. 1). This difference among retrievals confirms that in continuous long-term retrieval of aerosol distributions, it is critical to select the proper aerosol retrieval technique over the region of interest. Without such selection, discrepancies may arise even with the use of more advanced aerosol retrieval techniques, such as those used by the MODIS and the MISR sensors.

Table 1: Correlation coefficients calculated between the OMI AI and MODIS-Terra, MODIS-Aqua, and MISR AOD time series for the common period between November 2004 and December 2008.

Region	MODIS Terra	MODIS Aqua	MISR
Tropical Atlantic Ocean	0.93	0.87	0.82
North Africa	—	0.82	0.94
South Africa	0.93	0.94	0.95
Middle East	—	0.79	0.95
South Asia	0.54	0.64	0.10
East China	0.01	0.12	–0.05

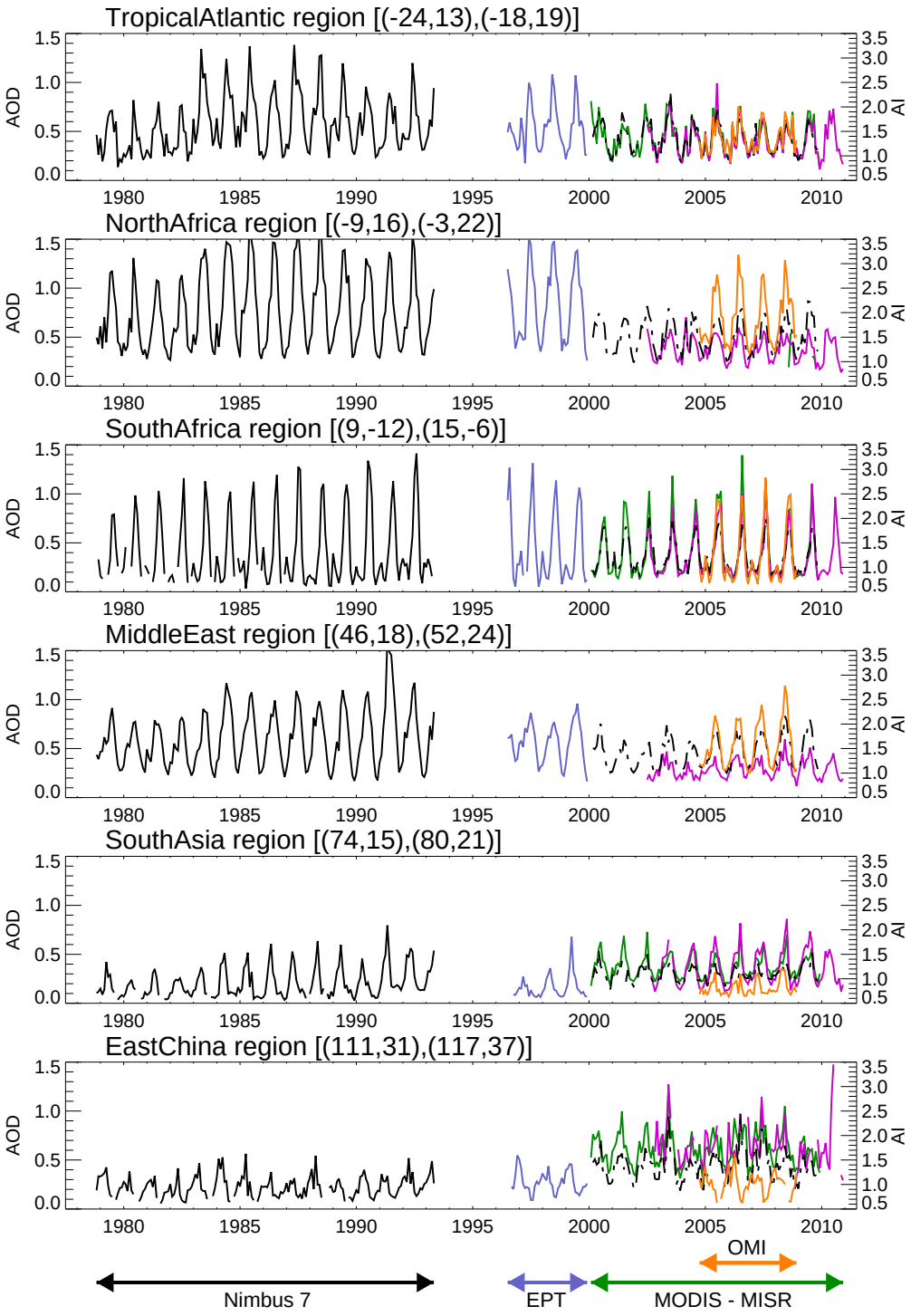

Figure 4: Monthly time series of AI and AOD averaged over the six regions marked in blue boxes in Fig. 2a. Black line corresponds to TOMS-Nimbus 7, blue to TOMS-Earth Probe, yellow to OMI, green to MODIS-Terra, red to MODIS-Aqua and black dotted to MISR datasets. Notice the different $y-$axis for AI and AOD at each side of the figures and the time-span of each platform marked with arrows at the bottom.

3.3 Annual and seasonal aerosol cycles

Figure 5 shows the mean annual cycle of AI and AOD for each of the regions defined in Figure 4. The longest datasets, TOMS-N7T and OMI for AI and MODIS Terra and Aqua for AOD, were used to compute annual cycles. North Africa and Middle East regions are not represented using the MODIS Terra dataset because data could not be retrieved over bright desert surfaces. The Tropical Atlantic, North Africa and Middle East regions show a unimodal aerosol annual cycle with maximum values during boreal summer for most of the aerosols dataset used. South Africa has a strong peak on late boreal summer associated with the biomass burning (Remer et al. 2008). MODIS AOD and TOMS-OMI AI data do not agree in the peak of maximum aerosol for the North Africa, South Asia and China regions. This discrepancy might be attributed to the variety of aerosol type affecting South Asia and China. South Asian aerosols have been reported to peak on a broad aerosol season spanning the period March to July (Remer et al. 2008; Bollasina et al. 2008) concurrent with the pre-monsoon season. The TOMS AI annual cycle shows a peak during April concurrent with the springtime maxima attributed to a mixture of dust outbreaks and biomass burning occurring across the South Asia (Yu et al. 2003) whereas MODIS Terra and Aqua AOD both peak in July in the same region. These patterns of aerosol distribution are attributed to a combination of the dust outbreaks with anthropogenic aerosols (sulfates) from pollution (Bao et al. 2009).

A Fourier spectrum calculated using daily data shows that a strong annual cycle dominates all six study regions (central panel in Fig. 5). The significance of the spectrum is compared to a red noise process with a 95% of confidence level. Results show that both the annual and semi-annual periods as well as the shorter variability periods are significant in the time series. The spectrum calculated retaining band periods shorter than 60 days in the right panel of Fig. 5 depicts high intraseasonal variability across all six regions. The usual shorter residency time of aerosols in the atmosphere

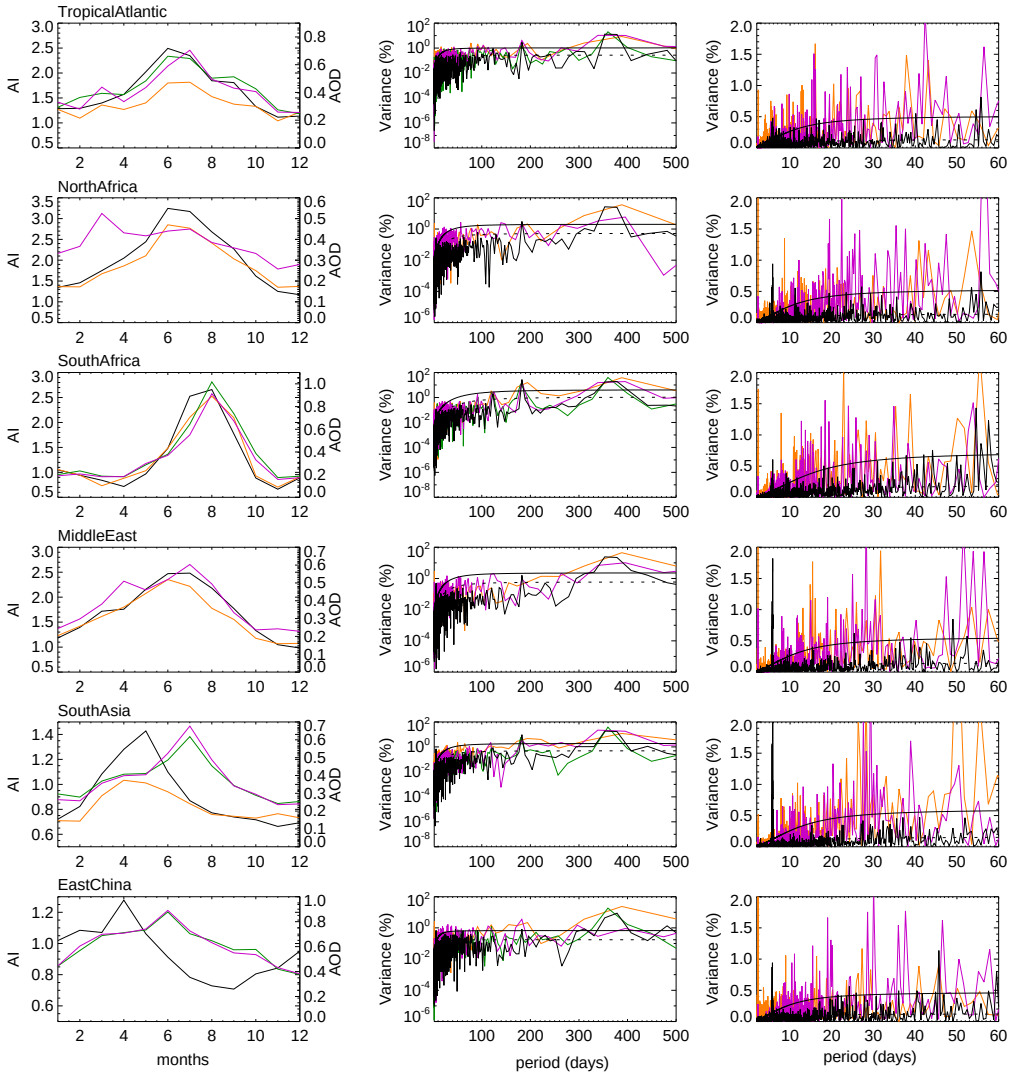

Figure 5: Mean annual cycle (left panel) and Fourier spectrums (center and right panel) of AI and AOD for the same regions shown in Fig. 4. Black line corresponds to TOMS-N7T, yellow to OMI, green to MODIS-Terra and red to MODIS-Aqua. The right panel presents a Fourier spectrum retaining the 2–60 day band periods of the series and the significance of each spectrum is compared to a red noise process with a 95% of confidence level (continuous black line).

and the influence of synoptic disturbances on biomass burning and dust outbreaks give the characteristic of shorter periodicity. For example, North Africa and Tropical Atlantic ocean regions are highly influenced by variability produced by Easterly Waves (Prospero and Carlson 1972), whereas South Africa and Eastern China are influenced by intraseasonal variability related to the Madden-Julian Oscillation (Tian

et al. 2008). This topic is explored in more detail in the next the chapter.

3.4 Tendencies in the aerosol datasets

Several studies have tried to use satellite datasets to investigate trend patterns in aerosol distribution. For example, Herman et al. (1997) reported an increase in absorbing aerosols attributed to biomass burning over the Amazon since 1978 using radiances from the TOMS instrument. In a more recent study using AOD from the AVHRR satellite, Koren et al. (2007; 2009) reported a declining trend in biomass burning since 2006 in the Amazon region. Further analysis using OMI AI and MODIS extinction optical depth indicate a reduction in the number of fires during 2008–2009, supporting the decline in the biomass-burning trend (Torres et al. 2010). Based on TOMS data, Massie et al. (2004) reported a large increase in AOD between 1979 and 2000 over East China and the Ganges River basin in India during the winter months of November to February. The same positive trends over eastern China have been also reported in MODIS AOD from 2000 to 2006 (Bao et al. 2009; Zhang and Reid 2010) and in TOMS AOD from 1997 to 2001 (Xie and Xia 2008). Meanwhile, George et al. (2008) reported a decrease in AOD between 1986 and 1999 and then a rise from 1999 to 2004 over the North Indian Ocean, consistent with the Massie et al. (2004) findings. Over the Mediterranean basin and North America, two studies found a decreasing linear tendency in MODIS AOD from 2000 to 2006 (Papadimas et al. 2008; Zhang and Reid 2010). The trends in aerosol reductions over those two regions agree with legislative reductions in the anthropogenic emissions of sulfur and black carbon in many developed nations (Streets et al. 2009). This trend has been also reported in AOD from AVHRR satellite data after 1990 (Mishchenko et al. 2007; Zhao et al. 2008), which may have contributed to the concurrent upward trend in surface solar fluxes and a global "brightening" (Wild 2009). At the same time, there is a statistically negligible change in AOD over regions such as the global oceans,

Australia and North Asia (Wang et al. 2009; Zhang and Reid 2010).

While these studies have focused on the analysis of regional or global average trends, none of them look at the spatial distribution of aerosol trends. The use of an average trend can be misleading in both understanding and documenting the trend since the distribution of aerosols is spatially heterogeneous. In this section, we use the longest in each of the satellite aerosol datasets to document the global spatial distribution of aerosol trends. The distribution of the tendencies is presented for the 45°N to 45°S latitudinal band, which is the center of the satellite aerosol retrievals. To compute trends, we generated monthly AI and AOD anomalies as deviations from the monthly mean in each of the time periods of each platform (i.e., 1979–1992 for TOMS-N7T, 2005–2008 for OMI, 2000–2009 for MODIS-Terra, 2003–2010 for MODIS-Aqua and 2001–2010 for MISR). The Mann-Kendall technique (Hirsch et al. 1982) was used to compute the trends. The technique goes beyond the traditional methods of linear regression analysis because it is non-parametric and does not depend on a specific distribution of the anomalies. The procedure is based on a ranking test suitable to detect monotonic trends during a particular time interval that does not necessarily have to be linear. The Mann-Kendal statistic Z and the seasonal Kendall slope estimator B were computed. For detailed explanation see Hirsch et al. (1982). The statistic Z tests the hypothesis of positive, zero or negative tendency comparing to a standard normal distribution with an assumed probability (e.g., 95% confidence). A positive value of Z indicates a significant upward tendency and a negative Z a downward trend. A greater absolute value of Z indicates higher probability of rejecting the null hypothesis of randomness. These sets of tests have been used for atmospheric and hydrologic data analysis with good performance (e.g., Hirsch et al. 1982, Molnar and Ramirez 2001, Agudelo and Curry 2004). For comparison purposes, tendencies were also computed using traditional methods of trend analysis (i.e., Ordinary Least Squares (OLS), Least Absolute Deviation (LAD) and Chi-Square error statistic (CHI),

for a detailed explanation of the methods see Wilks 2006).

Figures 6 and 7 show the standard normal statistic Z obtained using the Mann-Kendal technique for TOMS-N7T and OMI AI and MODIS-Aqua and MISR AOD, respectively. The technique was applied separately to each of the satellite dataset periods of registry. In the case of the TOMS-N7T dataset, tendencies were estimated during the initial and final 7 years of registry. This was done for two reasons: 1) to have a similar length of data to make inter-comparisons because all aerosol datasets have a data lifetime of around 7 years, and 2) the period covered 1988–1990 corresponding to the reversal in global aerosol tendencies reported in previous studies (Mishchenko et al. 2007; Zhao et al. 2008). Figure 6 shows a considerable positive AI tendency from 1979 to 1984 over much of the tropics, particularly over the Tropical Atlantic Ocean, Northern and Central Africa and Middle East and South Asia. From 1987 to 1992, AI shows positive tendencies for Central and South Africa, Middle East, South Asia and Australia; whereas there are negative AI tendencies for the Tropical Atlantic Ocean and Northern Africa. Over the Mediterranean Ocean there are some small negative tendencies but they are not significant. These negative tendencies continue to be seen over Northern Africa and the Mediterranean Ocean and Europe when calculated using AOD from MODIS and MISR during the 2000s (Figure 7). This increasing trend during early 1980s and then decreasing after 1990s has been related to the "dimming" and "brightening" in solar radiation reaching the surface attributed, along with others factors, to an anthropogenic contribution through changes in aerosol emissions governed by economic developed nations and air pollution regulations (Wild 2009). A striking feature in Figure 6 and Figure 7 is the significant positive tendency that AI and AOD are experiencing over the Middle East, Arabian Sea and South Asia. This characteristic positive tendency is occurring over the whole period of registry from 1980 up to 2010.

To quantify the amount of AI and AOD increase or decrease, the seasonal Kendall

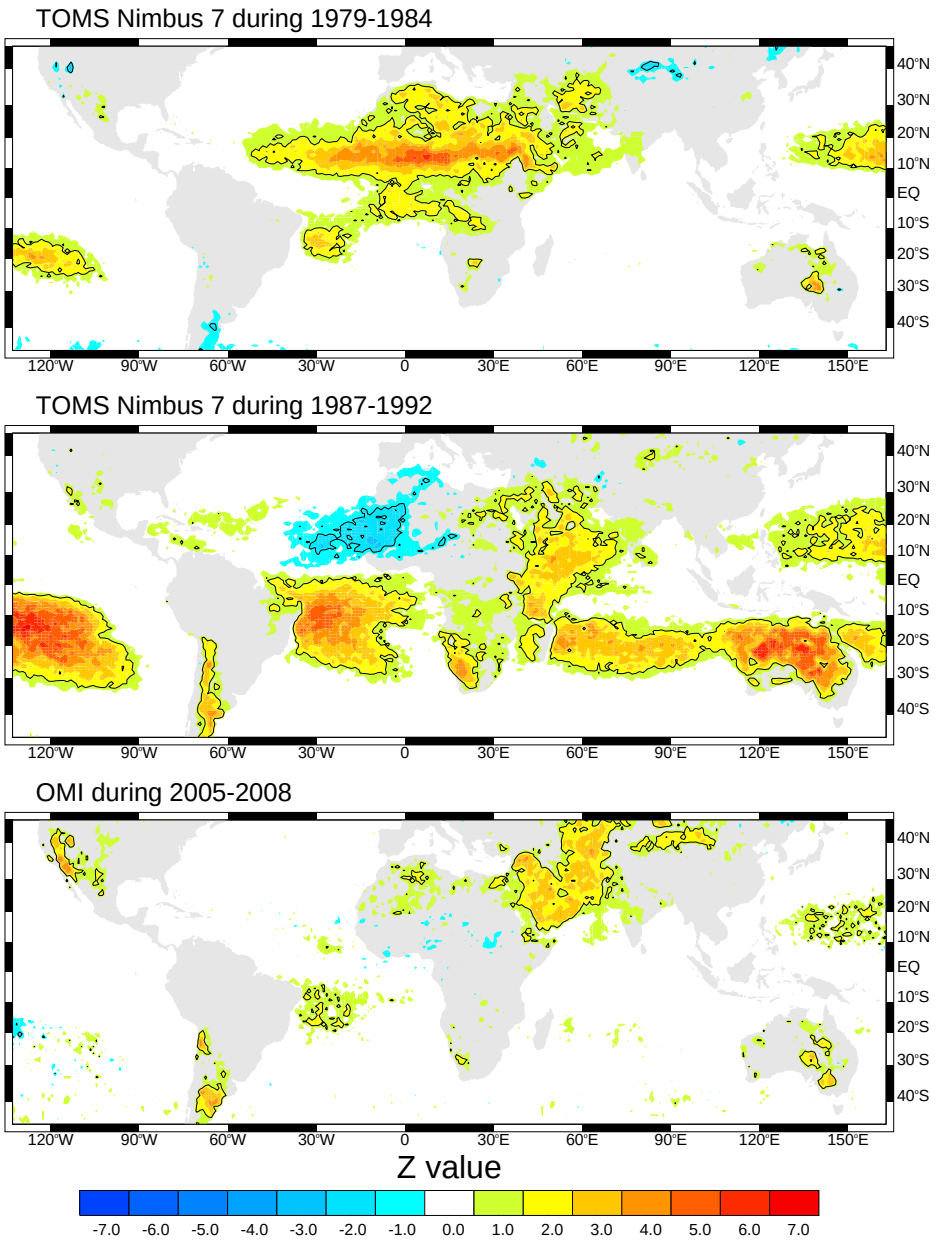

Figure 6: Spatial distribution of the standard normal statistic Z obtained using the Mann-Kendal technique for the time series of AI from TOMS-N7T during 1979–1994 (top) and 1987–1992 (center), and from OMI during 2005–2008 (bottom) periods. The color shading is relative to the scale bar at the bottom of the figure and the black contour encloses regions with trend significance level greater than 95%.

slope estimator for the respective tendencies was calculated for TOMS-N7T and OMI datasets (Figure 8) and for MODIS and MISR datasets (Figure 9). In general, the sign of the tendency slopes in Figs. 8–10 are similar to the sign described previously for all

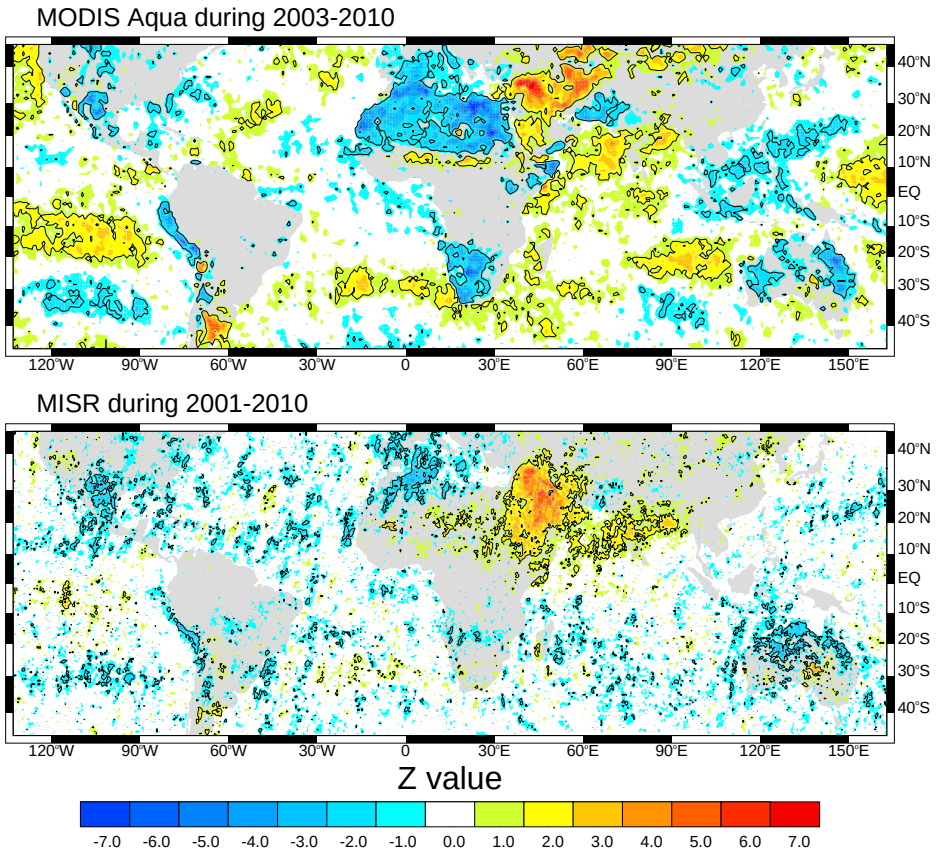

Figure 7: Same as Fig. 6, but for the time series of MODIS-Aqua (top) and MISR (bottom) AOD during 2003–2010 and 2001–2010 periods, respectively.

the aerosol regions in Figs. 6 and 7. Significant values up to +0.1 year^{-1} in AI can be seen over the Middle East, Arabian Sea and South Asia. Figure 6 shows a tendency in AI values higher than +0.1 year^{-1} over the Tropical Atlantic Ocean and North Africa from 1979 to 1984. Then, the tendency reverses down to AI values of around –0.1 year^{-1} from 1987 to 1992, significantly over the west of Northern Africa and Atlantic Ocean. The tendencies found using the OMI dataset for the period 2005–2008 in Fig. 8 do not reach statistically significant values to provide a distinguishable tendency over Northern Africa and the Atlantic Ocean. From the more recent aerosol datasets (e.g., MODIS and MISR in Fig. 9), significant AOD negative tendencies around –0.15 year^{-1} are seen again over Northern Africa and Mediterranean Ocean. AOD values up to +0.2 year^{-1} occur over the Middle East and some regions over South Asia.

This increase in AOD values in the past ten years over South Asia and Middle East is reported to have been strongly influenced by dust events (Zhang and Reid 2010).

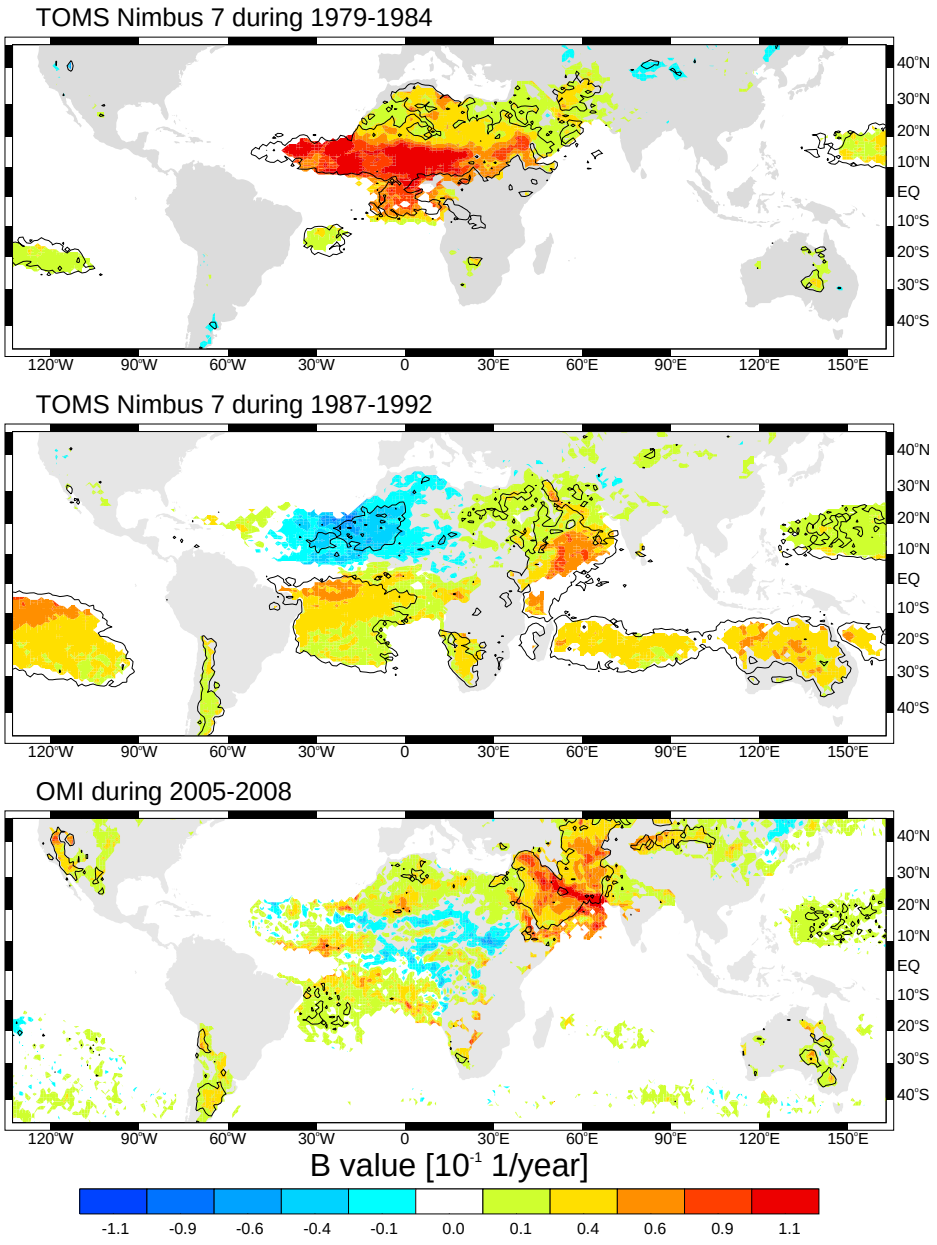

Figure 8: Spatial distribution of the seasonal Kendall slope estimator B calculated for the time series of AI from TOMS-N7T during 1979–1994 (top) and 1987–1992 (center), and from OMI during 2005–2008 (bottom) periods. The black contour encloses regions with trend significance level greater than 95%.

Other regions over the globe, such as East China, the east coast of North America, the Amazon region and central Africa do not appear to have significant trends.

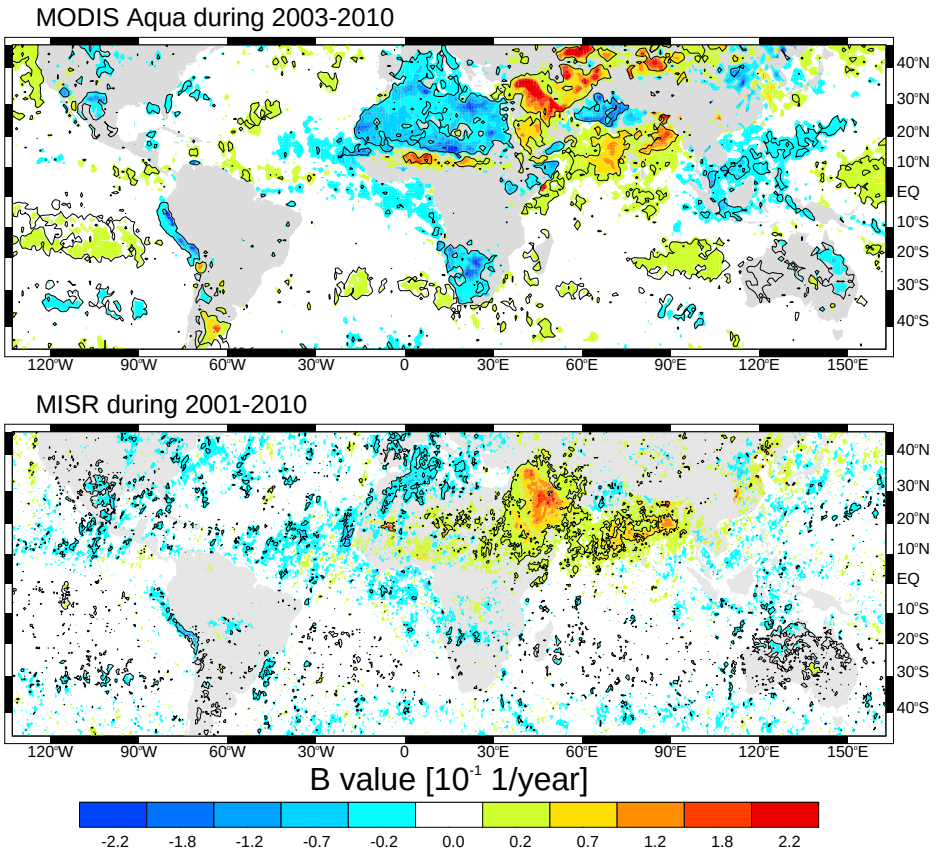

Figure 9: Same as Fig. 8, but for the time series of MODIS-Aqua (top) and MISR (bottom) AOD during 2003–2010 and 2001–2010 periods, respectively.

Neither AI nor AOD datasets in Figures 8 and 9 suggest a noteworthy tendency in aerosol loading among those regions. Considerable amount of missing values in all datasets over these regions prevent the technique from providing a unique tendency value.

Finally, we computed the tendency slopes using OLS and LAD estimators to compare the robustness of the trends calculated using the Mann-Kendall methodology (Figure 10). At first glance, Fig. 10 represents very similar tendencies to those shown in Fig. 8. Significant values up to +0.1 year^{-1} in AI can be seen over the Middle East, Arabian Sea and South Asia for trends estimated using both methodologies. The reversal in tendencies over the west of Northern Africa and adjacent Atlantic Ocean is also seen in Figure 10. There are no significant differences between the

results from the Mann-Kendall methodology and traditional techniques.

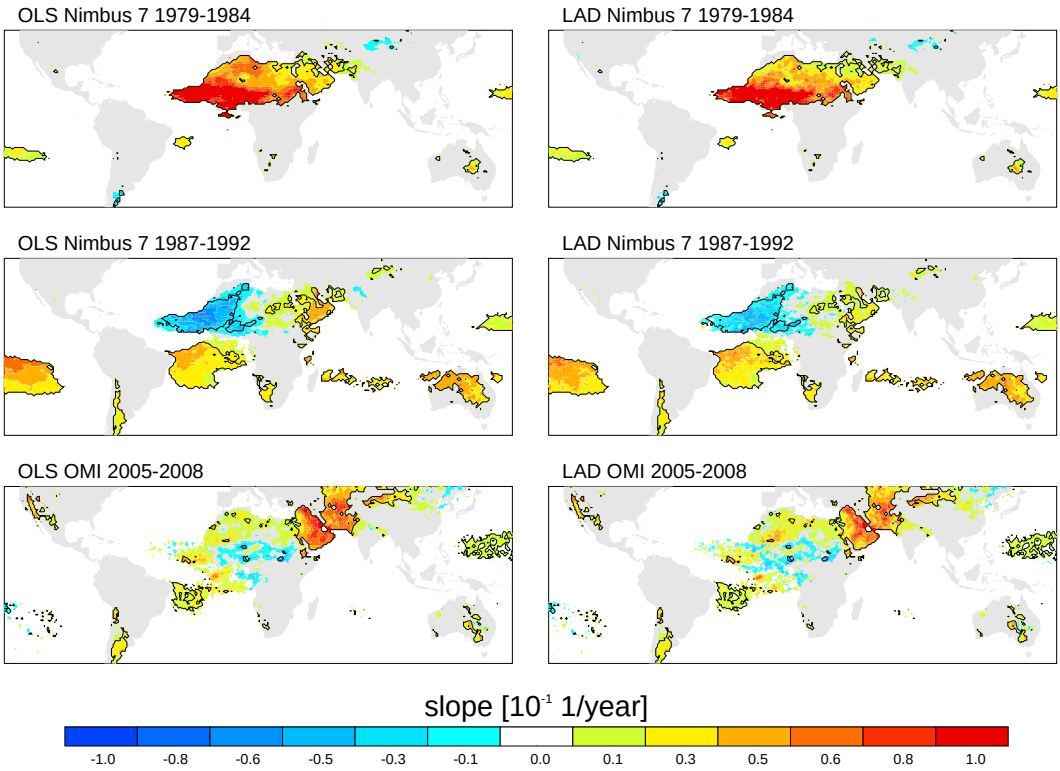

Figure 10: Spatial distribution of the AI trend computed with the ordinary least square (OLS) and least absolute deviations (LAD) techniques for the same datasets and periods as Fig. 6. The black contour encloses regions with trend significance level greater than 95%

CHAPTER IV

VARIABILITY OF AEROSOLS IN THE TROPICAL ATLANTIC OCEAN

Dust is by far the most abundant and ubiquitous aerosol type. North Africa is recognized as the largest dust source providing around the 50% of the global annual mass (e.g., Prospero et al. 2002). Dust originating from the Bodélé Depression and the Western Sahara is the most significant source thought to impact ecosystems off the American coast (Washington and Todd 2005; Prospero et al. 2010) and even alter biogeochemical cycles in the Amazon Basin (Swap et al. 1992). Westward intrusion of dust-laden air from the African continent into the tropical North Atlantic Ocean is a frequent phenomenon during the boreal summer (Carlson and Prospero 1972). The entrainment of large quantities of dust into the atmosphere require two sets of conditions; a supply of surface sediment and strong surface winds. These conditions are well matched in the region where thick layers of sediment are exposed and provide the unlimited source of material to be eroded. Surface wetness, vegetation cover and rainfall are characteristically low in the region, which makes perfect environmental factors to favor dust mobilization and transport over the region (Prospero et al. 2002).

The synoptic to local atmospheric processes involved have been characterized into conceptual models (e.g., Carlson and Prospero 1972; Karyampudi and Carlson 1988) describing the meteorological conditions suitable for dust mobilization. In synthesis, the model describes how this dust-laden heated air emerges from West Africa within a series of large-scale anticyclonic eddies. This dusty air moves above the cool and moist trade-wind inversion layer elevating the dust air mass to 600–800 hPa layer (Carlson and Prospero 1972; Karyampudi and Carlson 1988). The vertical and horizontal

structure of this dust plume, usually referred as Saharan Air Layer (SAL), has been extensively studied and verified using *in situ* and satellite observations and numerical modeling (e.g., Karyampudi et al. 1999). The dust plume appearing in large-scale outbreaks, spanning from North Africa towards and over the Atlantic Ocean (Fig. 2) has been widely recognized as a climatological feature of the summer aerosol distribution over the region (e.g., Karyampudi et al. 1999; Huang et al. 2010; Knippertz and Todd 2010).

The rate of the westward incursion of dust into the Atlantic Ocean is modulated by African Easterly Waves (AEW, Burpee 1972) that propagate from the interior of North Africa across the west coast and towards the Atlantic Ocean (Jones et al. 2003). Two AEW regimes have been recognized (Carlson 1969; Burpee 1972; Reed et al. 1977; Viltard et al. 1997; Diedhiou et al. 1998; 1999). The first regime has a period of 3-5 days (phase velocity of 7-8 degree longitude per day, deg/day) and a second, which strongly modulates the zonal wind component, has a 6-9 days period or 5 deg/day. The extension of these synoptic-scale disturbances has a wavelength of about 2500–3000 km for the first regime and about 6000 km for the second (Diedhiou et al. 1998).

Whereas a number of different studies have recognized the role of AEWs in the modulation of African desert dust transport (Barkan et al. 2004; Jones et al. 2004a; Washington and Todd 2005; Knippertz and Todd 2010; Huang et al. 2010; Jury and Santiago 2010) in this chapter we propose a number of significant extensions. The objective of those extensions is to document how a "typical" AEW modifies the dust aerosol burden in the SAL and how the environment is modified by these aerosol intrusions. The uniqueness of this work is the use of the long-term satellite aerosol retrievals to determine modes of aerosol variability in relation to the two forms of AEW. Furthermore, we use reanalysis and satellite retrievals of atmospheric and oceanic variables to document how the atmosphere and the ocean are impacted by

dust aerosol variability and how these impacts compare with those in the Carlson and Prospero (1972) model of dust transport over the Atlantic Ocean.

4.1 Spectral Analysis

In order to characterize the temporal and spatial evolution of aerosols relative to AEW variability and their relationship with atmospheric variables, a region near to the coast of Africa in the center of the climatological dust corridor was selected (15°N–17°N, 22°W–20°W; box Fig. 2a). Daily time series of averaged TOMS-N7T AI (simply 'AI', hereafter) and MODIS-Aqua AOD (simply 'AOD', hereafter) over the selected region were computed. The time periods used for this analysis are 1979–1993 and 2002–2010, respectively. To obtain a representative sampling of aerosol data, a 3-day running mean over both gridded satellite datasets was applied to minimize the impact of missing data due to sensor swath coverage. Filtered time series were computed using a band-pass Fourier filter retaining time-band periods in 5 to 15 and 10 to 30 days range to match the two modes of variability of AEW over the region. Positive values greater than +1 standard deviation were selected on the filtered time series and the date of the maximum value in each period was chosen as the day 0 to compute the composites. To construct the composites, anomalies of gridded AI and AOD data were computed with respect to a 30-day running mean of the daily climatology in each of the analyzed periods. In addition, wind velocity and direction, geopotential height, potential temperature, specific humidity, SST and OLR anomalies were computed for periods matching the aerosol data sets. For the TOMS daily data, 161 days of maximum AI were found in the 5-15 day period and 80 days in the 10-30 day band. In similar way, MODIS indicated 76 and 44 days of maximum AOD in the 5-15 and 10-30 day period, respectively.

Sensitivity analyses were performed in order to test that the aggregation of AOD data would not introduce spurious modes of variability on the aerosol time series.

The results of these analyses are presented in the Appendix A of this document. In addition, to validate the significance of the variability modes calculated by the Fourier analysis, the Empirical Mode Decomposition technique was applied to the AI and AOD data. An analysis determining the statistical significance of the modes is presented in Appendix B.

4.2 Horizontal composite analysis

Figure 11 shows a longitude-time plot of TOMS AI and MODIS AOD anomalies for the 5-15 day and 10-30 day period bands. Day 0 in each plot represents a maximum in aerosol loading over the selected study region and composites were created by averaging the AI and AOD anomalies from –8 to 8 days around day 0. Additionally, positive geopotential height anomalies at 700 hPa are also plotted as solid contours in the same figure. Two modes of westward aerosol propagation are evident in both datasets, one with a period near 5-7 days (for the 5-15 day band filter) and another with a period near 9-11 days (for the 10-30 day band filter). There is good relationship between positive 700 hPa geopotential height anomalies with the positive aerosol anomalies and negative heights with negative aerosol anomalies. These two regimes represent the wave speeds of the two AEW forms crossing the region. The aerosol anomalies in Figure 2 using AI show a wave speed of approximately 8 deg/day (5-15 day band top left panel) and 6 deg/day (10-30 day band, right top panel) very similar to the AOD anomalies (right hand panels).

Figure 12 and 13 show the extension of the analyses to the longitude-latitude plane. Composites are constructed in the same way as in Figure 11 and show the horizontal distribution of aerosol anomalies using AI (Fig. 12) and AOD (Fig. 13) analyses for dates with the minimum and maximum values. Wind vectors and geopotential height anomalies at 700 hPa using ERA-40 and ERA-interim are also shown for the same composite time for the TOMS and MODIS periods, respectively. The

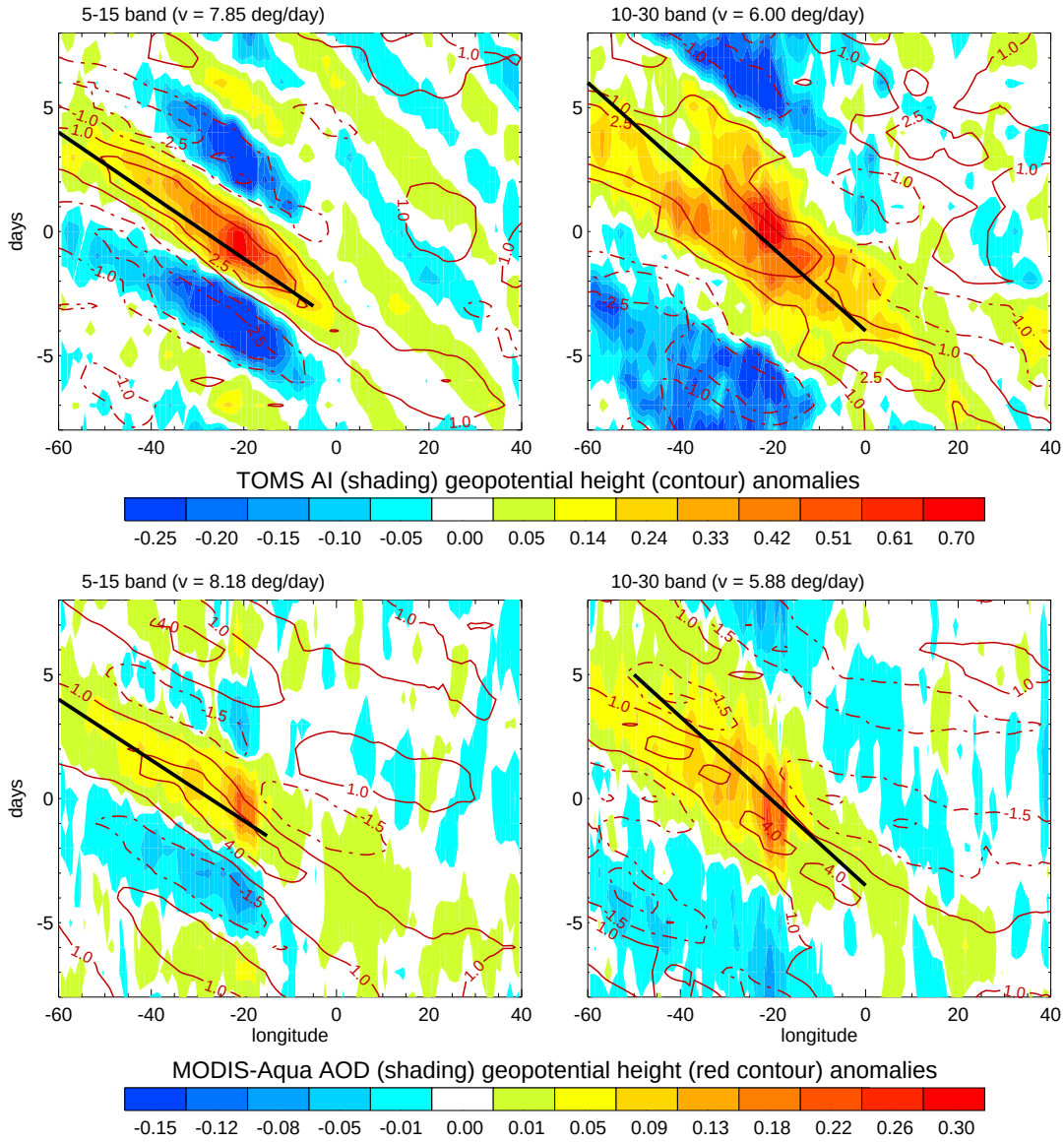

Figure 11: Longitude-time plots of aerosol (shading, relative to the color palette) and geopotential height (contours in [m], continuous line positive values) anomalies averaged between 15°N and 20°N. Upper panel corresponds to TOMS-AI variability composites in the 5-15 day (left) and 10-30 day (right) band. Lower panel corresponds to MODIS-AOD in the in the 5-15 day (left) and 10-30 day (right) band. For each plot a black solid line represent the mean average propagation of the positive aerosol anomalies and the speed of this propagation is indicated in the top of each diagram.

700 hPa level was selected because the average transportation of the dust takes place above the humid trade wind air in the 600–800 hPa layer and because AI is mostly sensitive to aerosols over 2 km. From the top to the bottom in Fig. 12, negative

AI anomalies are seen over the study region at 4 days before the aerosol loading maximum (for the 5-15 day band) and 6 days before (for the 10-30 day band) with collocated cyclonic winds and negative geopotential height anomalies. As time progresses towards the maximum in AI at day 0, the aerosol, wind and geopotential height anomalies move westward with a notable increase in magnitude. This composite progression displays westward propagation of aerosols with anticyclone wind and positive geopotential height anomalies, consistent with the results of the Carlson and Prospero (1972) model of dust transport over the Atlantic Ocean. At day 0, a discernible anticyclone circulation is apparent in both composites over the coast of West Africa. As the anticyclonic circulation moves eastward, the aerosol loading diminishes moving toward AI negative anomalies over the reference region. This occurs after 4 days in the 5-15 day band and 6 days in the 10-30 day band with a considerable reduction in geopotential height anomalies as well as a reversal in wind anomaly direction. The progression in MODIS AOD anomalies in Fig. 13 is remarkably similar to the progression of AI anomalies shown in Figure 12. The timing of the change between negative to positive AOD and geopotential height anomalies over the region match the timing of changes evident in the AI anomalies for both bands of the analysis. These similarities reaffirm the progression of the aerosol phenomena in accord with the synoptic variability and the speed of the two AEW regimes.

As the dust is transported over the desert surface towards the ocean, the air layer in which the aerosols are embedded is warmer and drier than the normal tropical atmosphere (Carlson and Prospero 1972). The aerosol layer helps to produce a very strong suppressive inversion above the moist trade wind air limiting precipitation, humidity and reducing surface shortwave radiation (Miller and Tegen 1998; Foltz and McPhaden 2008; Evan et al. 2009). To calculate the environmental impact produced by the variation of aerosol loading on the surrounding atmosphere and ocean, SST and OLR anomalies were calculated for the common periods of TOMS and MODIS

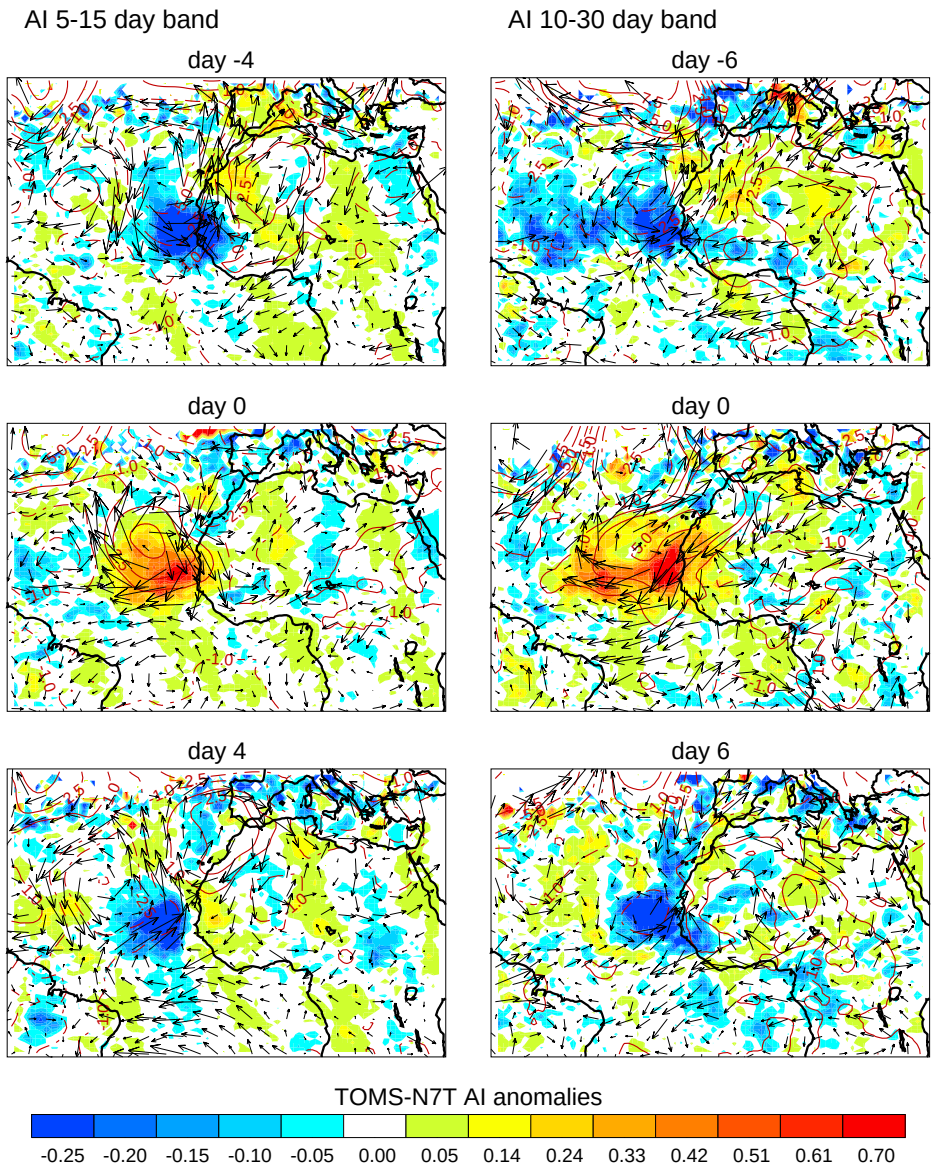

Figure 12: Composites of TOMS-N7T AI (shading, relative to the color palette), horizontal wind (vectors) and geopotential height (contours in [m], continuous line positive values) anomalies. ERA-40 data at 700 hPa is used to calculate wind and geopotential height anomalies. The composites are constructed based on the maximum in aerosol loading at day 0 over the reference region. The left panels correspond to composites based on the 5-15 day band and right panel to 10-30 day band.

datasets. Atmospheric water vapor and GPCP precipitation anomalies were used only for the MODIS period. Figure 14 shows composites of SST and OLR for –6 and 0 days of the maximum in MODIS AOD over the study region. The composites were calculated using the aerosol time series with a Fourier filter in the 10-30 day

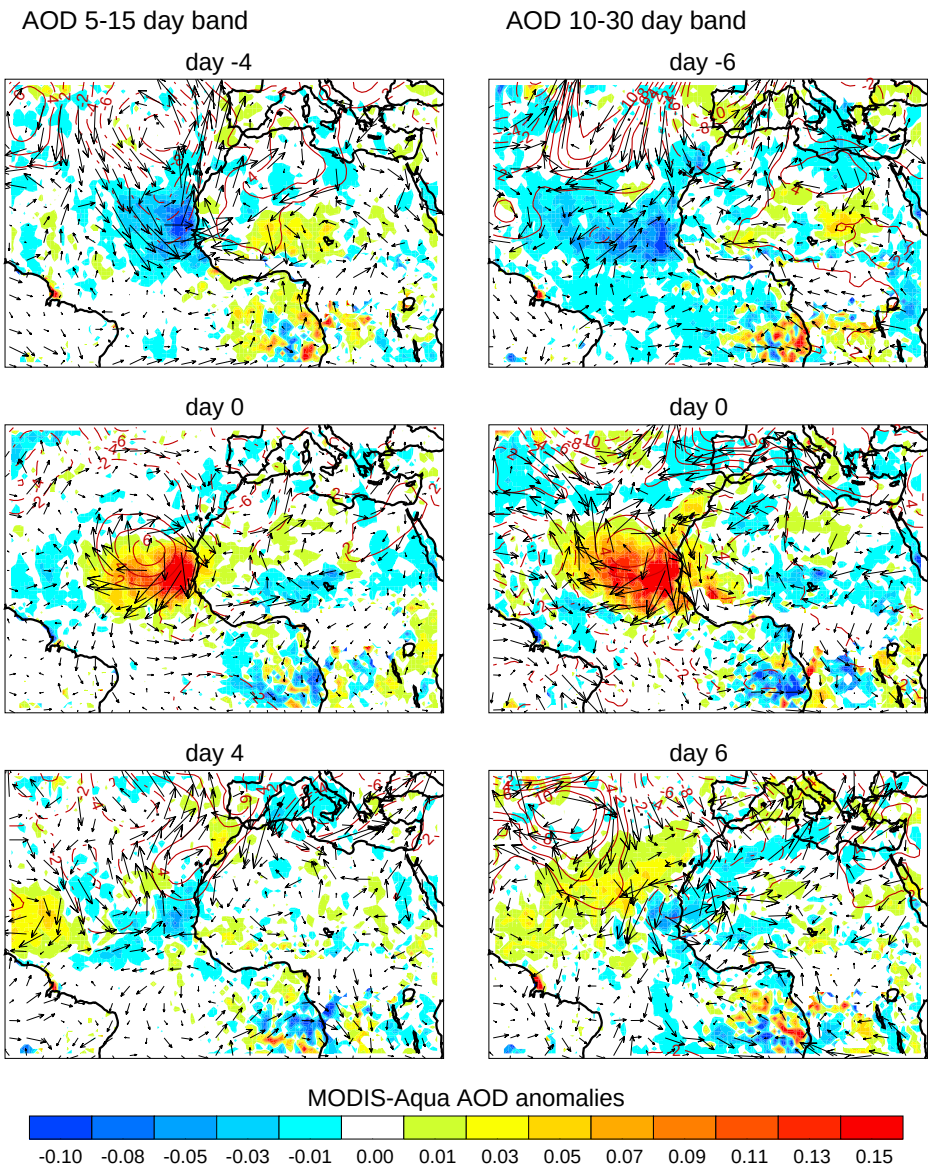

Figure 13: Same as Fig. 12, but for MODIS-Aqua AOD, ERA-interim horizontal wind and geopotential height anomalies.

band. The same composites were also calculated using TOMS for 5-15 day and 10-30 day bands (not shown). For each composite a contour representing positive and negative anomalies of AOD is also plotted. Six days prior to the maximum in AOD over the west coast of Africa, positive anomalies of SST and negative of OLR appear concurrently with negative aerosol anomalies in the reference region. At the time of maximum aerosol anomalies near to the coast of Africa, the SST has declined up

possessing negative anomalies and the OLR anomalies increases to positive values. The high solar absorption in the dust layer reduces shortwave radiation, which would otherwise be absorbed by the land and the upper ocean. After the aerosol anomalies start to decline, there is a recovery and SST anomalies become positive at day 6. It is important to note that the negative SST anomalies travel westward in phase with positive aerosol anomalies as the dust is carried westward by the anticyclone. Figure 15 shows composites of GPCP rainfall and precipitable water vapor as the aerosol anomalies change between minimum and maximum during –6 and 0 days of the maximum in MODIS AOD. There is a general correspondence between reduced precipitation, reduced precipitable water vapor and an increase in aerosol anomalies during the day 0 of the composites.

The latter observations in the composites presented in Figure 14 and Figure 15 are consistent with a negative radiative forcing at the surface imposed by absorbing aerosols. This forcing is being balanced by a reduction in upward thermal radiation associated with a decreased surface temperature. A reduction of turbulent fluxes of sensible and latent heating into the atmosphere produces a stabilization of the air column within which vertical motion is inhibited thus reducing precipitation (Coakley and Cess 1985; Miller and Tegen 1998). Time series of composite anomalies of aerosol loading, zonal wind, geopotential height, SST, OLR, water vapor and GPCP rainfall anomalies are plotted in Figure 16 for the two aerosol datasets. The left panel shows the evolution of anomalies in the 5-15 and 10-30 day bands based on TOMS AI data. The right panel is based on MODIS AOD dataset. Similar patterns emerge for all of the anomaly evolution time series. As positive anomalies of aerosol loading increase towards day 0 (maximum aerosol loading), there is a reversal from easterly to westerly in zonal wind direction, a change of sign from negative geopotential height values (low pressure) to positive values (high pressure) and an increase towards a maximum in wind speed. There is also a decrease towards minimum values of SST, water vapor

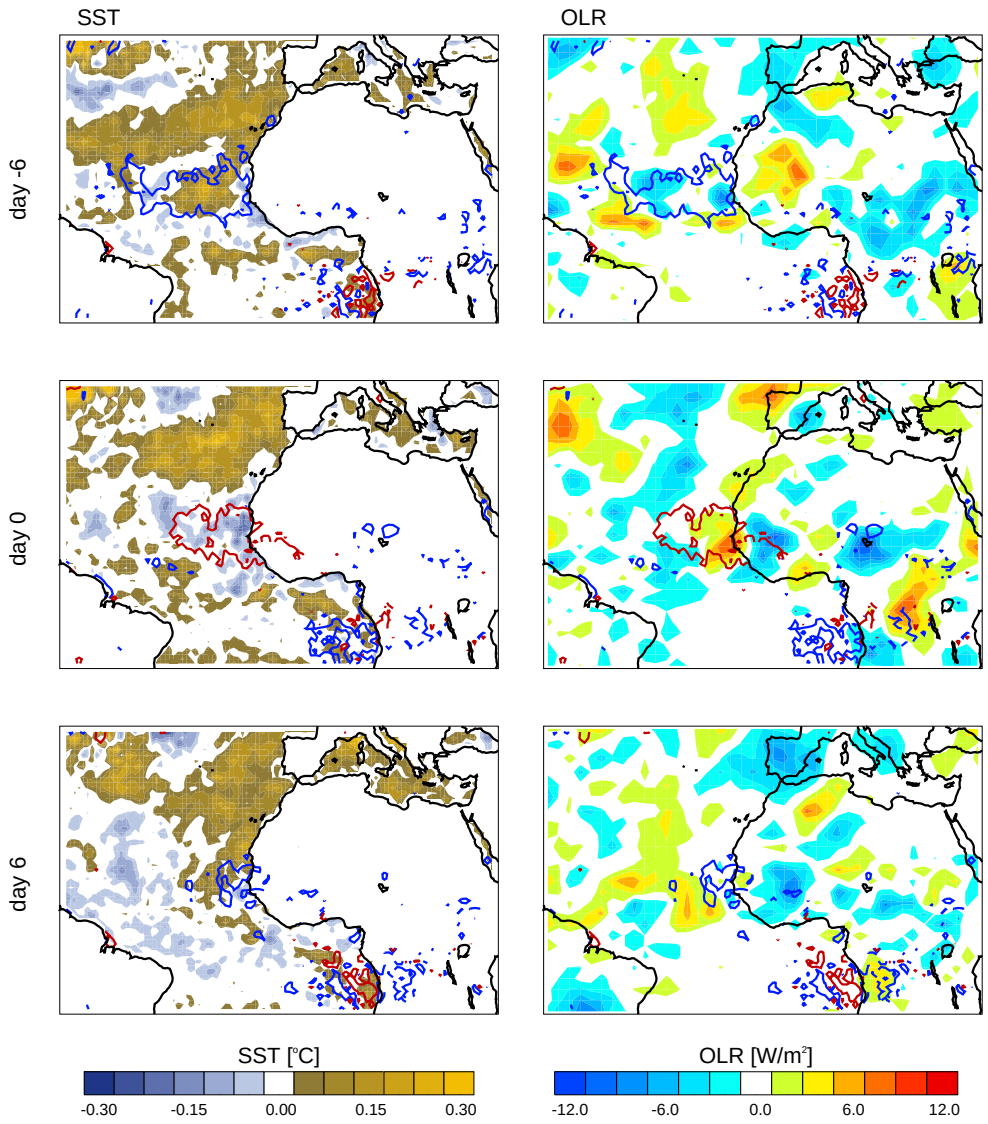

Figure 14: Composites of SST and OLR anomalies (shading, relative to the color palette) during the minimum and maximum in aerosol loading over the reference region for the MODIS AOD dataset within the 10-30 day variability band. The red contour in each plot corresponds to positive AOD anomalies and the blue contour to negative AOD anomalies in each time period.

and rainfall rate and towards a maximum in OLR as aerosol loading increases.

4.3 Vertical composite analysis

In order to analyze the vertical state of the atmosphere during the evolution of aerosol loading, composite analysis of the latitude-height structure of zonal, meridional, and

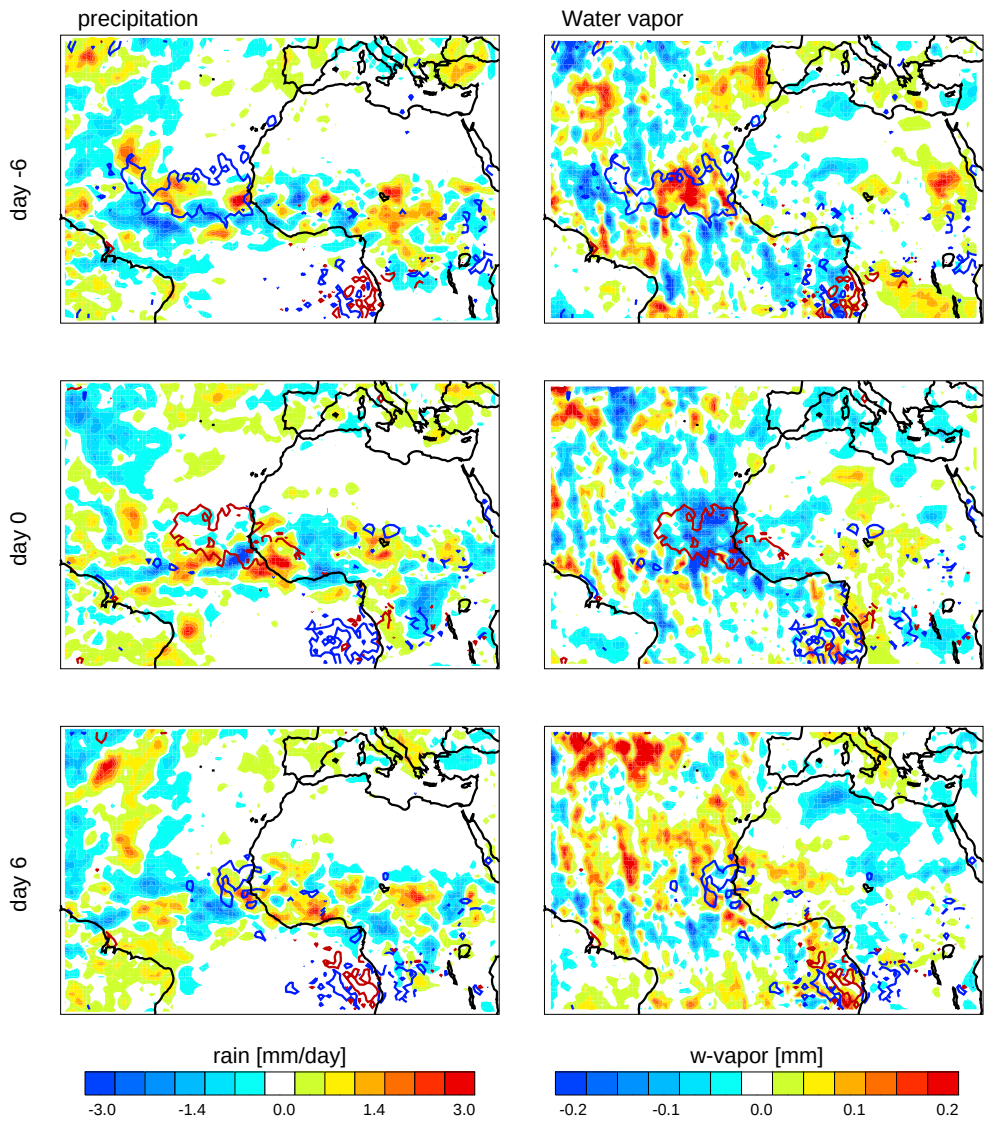

Figure 15: Same as Fig. 14, but for GPCP rain and MODIS Near-Infrared total precipitable water vapor anomalies.

vertical wind speed, geopotential height, potential temperature and humidity anomalies are constructed. Figures 17 and 18 show composites from ERA-40 and ERA-interim for the TOMS and MODIS periods averaged over the 40°W to 10°W longitude band for day –4 and day 0 relative to the maximum in AI and AOD over the study region (i.e., 15°N–17°N, 22°W–20°W), respectively. Composites in Figures 17 and 18 were calculated based on AI and AOD in the 5-15 day band and the vertical wind is exaggerated 1000 times to allow a comparison with the horizontal wind. Four days

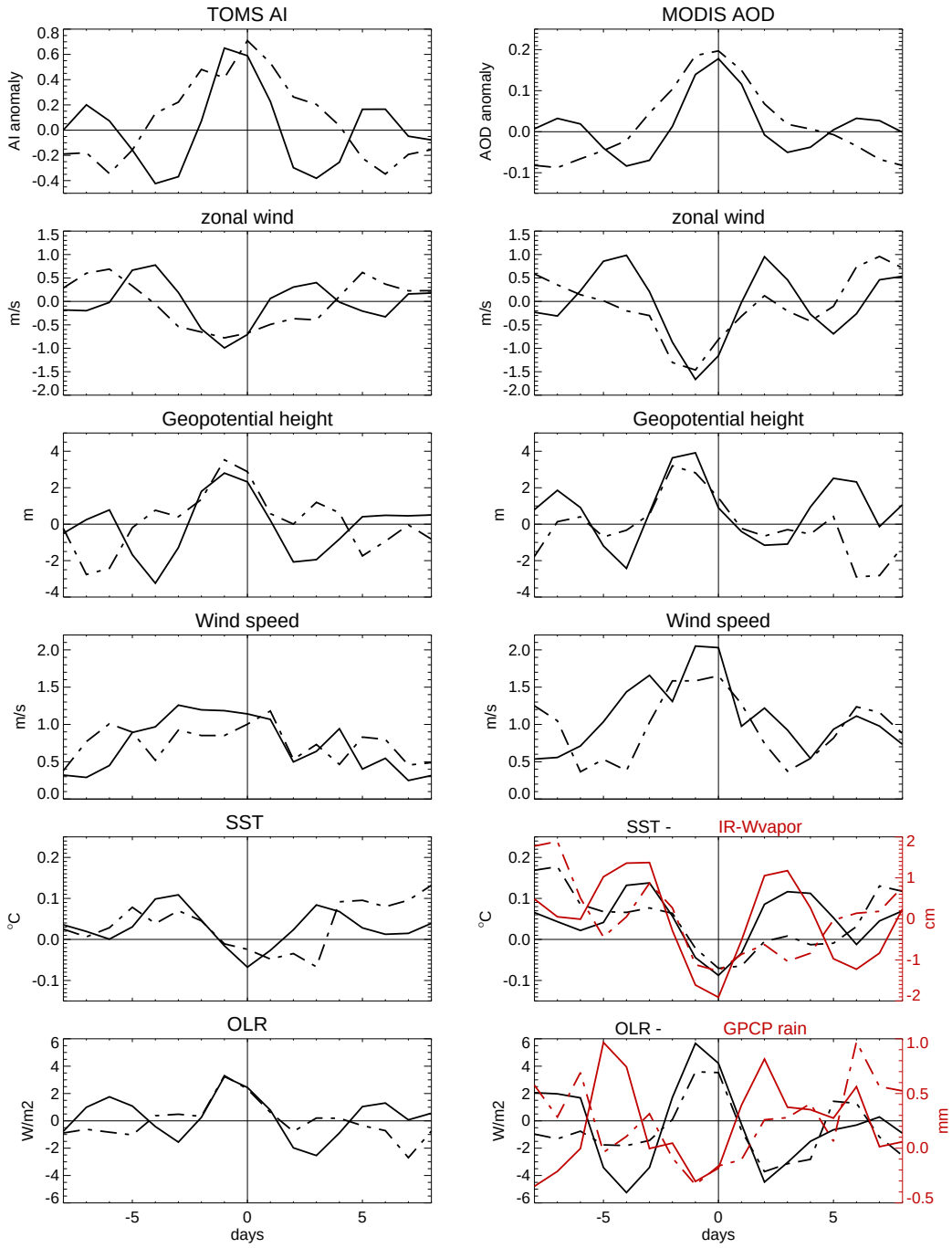

Figure 16: Evolution in time of TOMS-N7T AI and MODIS-Aqua AOD, zonal wind in [m/s], geopotential height in [m], wind speed in [m/s], SST in [°C], OLR in [W/m^2], IR-atmospheric water vapor in [mm] and GPCP rainfall rate in [mm] averaged over the reference region from –8 to +8 days around the aerosol maxima. Left panel is based on TOMS AI and right panel on MODIS AOD variability day band. Solid line corresponds to anomalies for 5-15 day and dash-dot line to 10-30 day variability band.

before the maxima in aerosol (aerosol minima, see black line in Fig. 17b), there is a prominent middle troposphere cyclone centered around 20°N with associated negative geopotential anomalies. We hypothesize that the subsidence near 20°N acts to prevent aerosol to build up. There is a minimum in potential temperature in the lower troposphere around 850 hPa and a maximum in the boundary layer specific humidity (Fig. 17b) both displaced northward from the minimum in AI anomalies. At the time of the aerosol maximum loading the zonal wind reverses towards an anticyclonic circulation and a maximum in geopotential height. The presence of a strong middle level easterly jet (centered around 14°N) between the upstream trough and downstream ridge axis of an AEW is a common characteristic of the SAL (Karyampudi et al. 1999). There is noticeable upward motion between 12°N and 22°N (i.e., the dust corridor) with a collocation of anomalously warm and dry air mass forming a temperature inversion around 875 hPa near the base of the SAL and over a moist boundary layer. The inversion between the marine mixed layer and the base of the SAL (i.e., 850 hPa) is identified by a rapid increase in potential temperature with height. The negative anomaly in specific humidity near the base of the SAL indicates a dry and stable atmosphere, inhibiting cloud formation (Karyampudi and Carlson 1988). Figure 18, constructed in the same way as Figure 17 but based on MODIS AOD, displays the same characteristics of wind, geopotential height, potential temperature and specific humidity anomalies as discussed before. Those similarities reaffirm once again the good agreement given by both aerosol satellite based datasets of the physical phenomena.

A common feature of the SAL is that intense radiative heating accompany dust transport over the desert surface as hot and dry air emerges from the west coast of Africa. The emergence of dusty, anomalously warm and dry air is viewed better in the latitudinal composites averaged between 10°N and 20°N shown in Figures 19 and 20. Four days prior to the maximum in aerosol loading anomalies in the study region

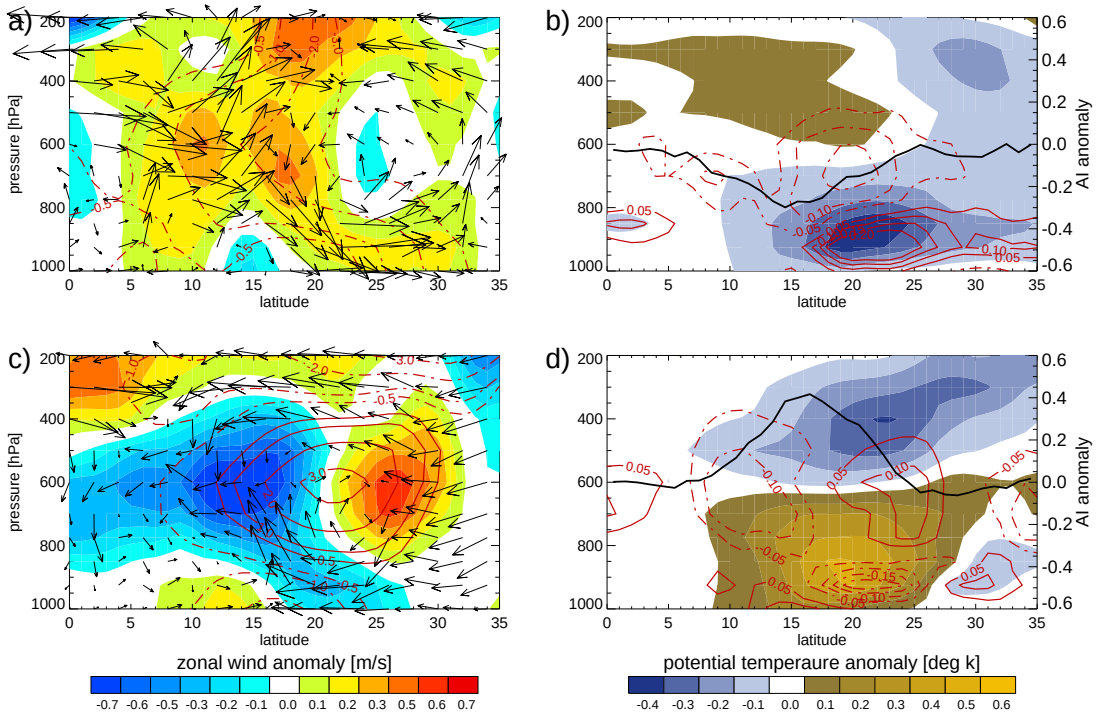

Figure 17: Longitudinal-averaged composites of zonal wind (shading), geopotential height (red contours in [m]) and meridional-vertical wind (vectors) anomalies for four days (a) and zero days (c) of the maximum in TOMS-N7T AI over the reference region and within the 5-15 day variability band. Longitudinal averaged potential temperature (shading), specific humidity (red contours in [g/kg]) and AI horizontal profile (black line) anomalies for four days (b) and zero days (d) of the maximum in TOMS-N7T AI.

there is middle level zonal wind convergence favoring sinking motion in the lower levels of the troposphere near 18°W. There are humid and cool temperatures over a diminished aerosol layer (around 30°W–15°W, in Fig. 19b). At the same time, over the Saharan desert (5°W–10°E) there is an upper level trough and upward motion accompanying the hot and dry air emerging from the African desert. The center of positive potential temperature anomalies decreasing with height over North Africa (around 0°) favors instability from the surface to the mid-troposphere creating a favorable environment for the African dust to be eroded from the Saharan desert. At day 0, the time of maximum aerosol loading, the meridional wind reverses and the zonal wind becomes easterly with hot and dry air that has moved over the region

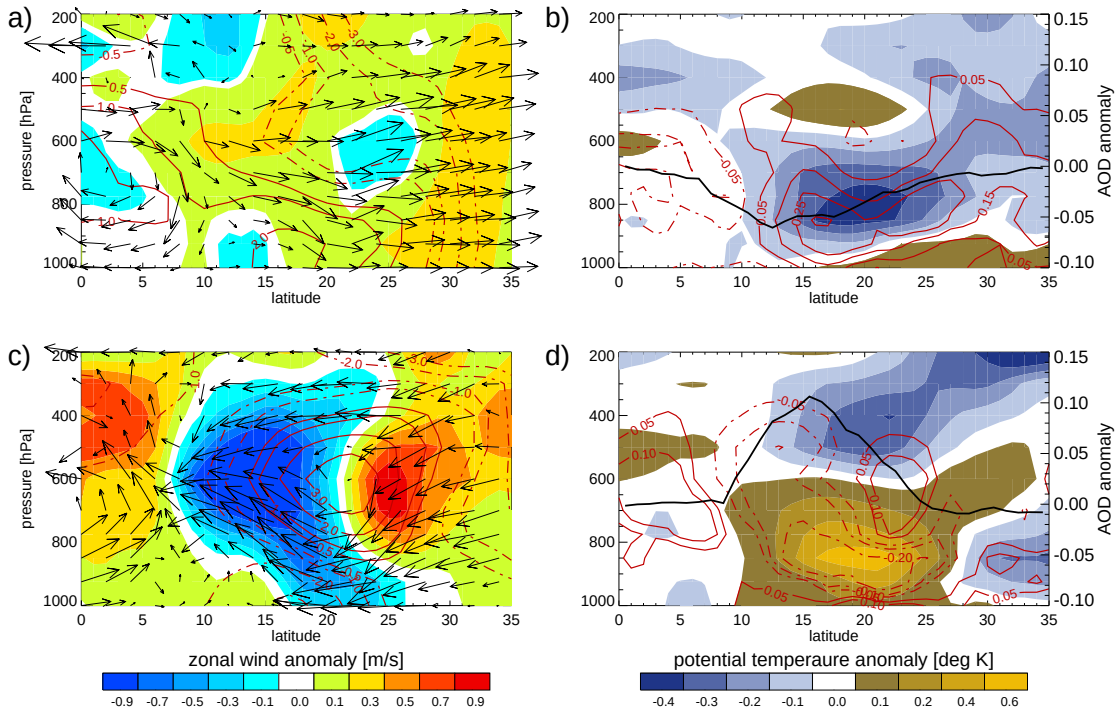

Figure 18: Same as Fig. 17, but based on MODIS-Aqua AOD and within the 5-15 day variability band.

of maximum aerosol loading (Figs. 19c and 19d). This warm and dry air is located over humid and cooler air favoring the maintenance of the African dust plume located in the lower to middle troposphere above the moist trade-wind (Carlson and Prospero 1972; Karyampudi and Carlson 1988; Knippertz and Todd 2010). Similar characteristic motion and atmospheric state, as presented in Figures 17–20, were also found for the 10-30 day band variability modes within the AEW analysis using the both satellite and reanalysis datasets (not shown). The only noticeable difference was that the temperature and humidity anomalies in the analysis of the longest variability mode possessed a greater longitudinal extension. This is coincident with a greater wave extension within the longer period of variability in similar way as the difference in wave extension in Figure 2.

Figure 21 and Figure 22 show the evolution of the vertical profiles of zonal and vertical wind, potential temperature and humidity anomalies through the composite

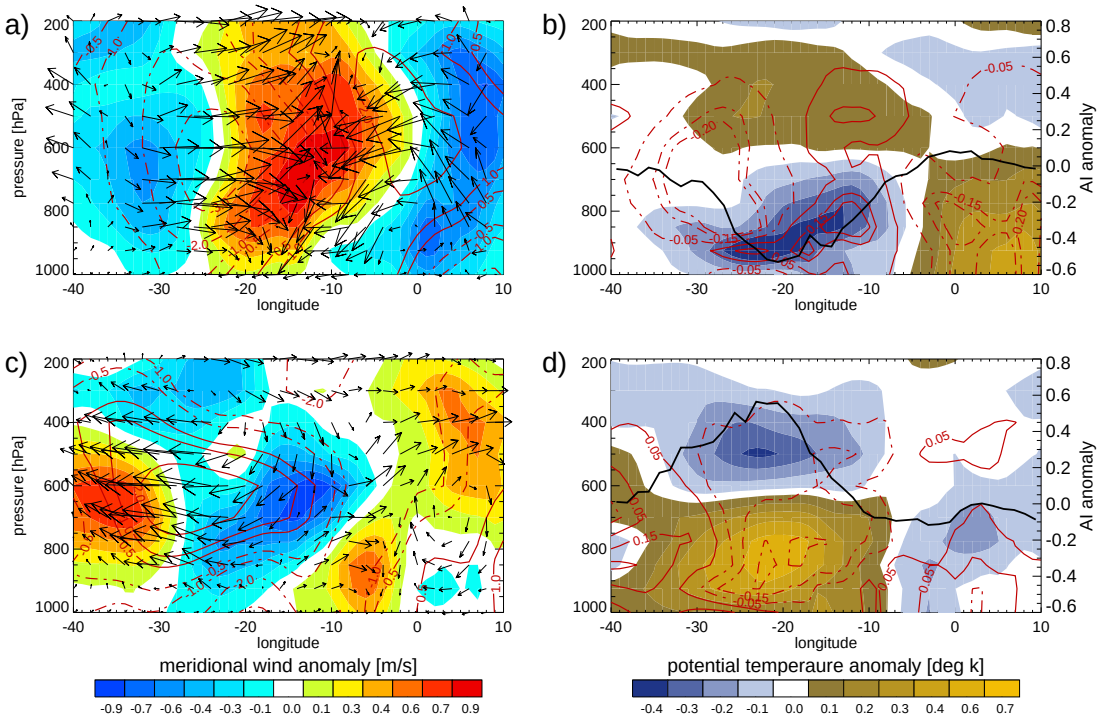

Figure 19: Latitudinal-averaged composites of meridional wind (shading), geopotential height (red contours in [m]) and zonal-vertical wind (vectors) anomalies for four days (a) and zero days (c) of the maximum in TOMS-N7T AI over the reference region and within the 5-15 day variability band. Longitudinal averaged potential temperature (shading), specific humidity (red contours in [g/kg]) and AI horizontal profile (black line) anomalies for four days (b) and zero days (d) of the maximum in TOMS-N7T AI.

period within the 5-15 day band variability associated with the AI and AOD anomalies. The composite profiles are constructed by averaging each variable horizontally over the study region, locating the day zero as the day of maximum aerosol loading and computing averages of –6 to +6 days from the dates about this maximum. Figures 21a and 22a show that about 4 days before day zero, low level easterly wind anomalies start to increase in height reaching a maximum near day –1 and forming the middle level easterly jet. The increase in vertical velocity (i.e., increasing negative anomalies) near the day 0 is also favoring conditions resulting in dust mobilization. In addition, there is an increment of positive anomalies of geopotential height from the surface towards the middle troposphere (not shown). Figures 21b and 22b show a

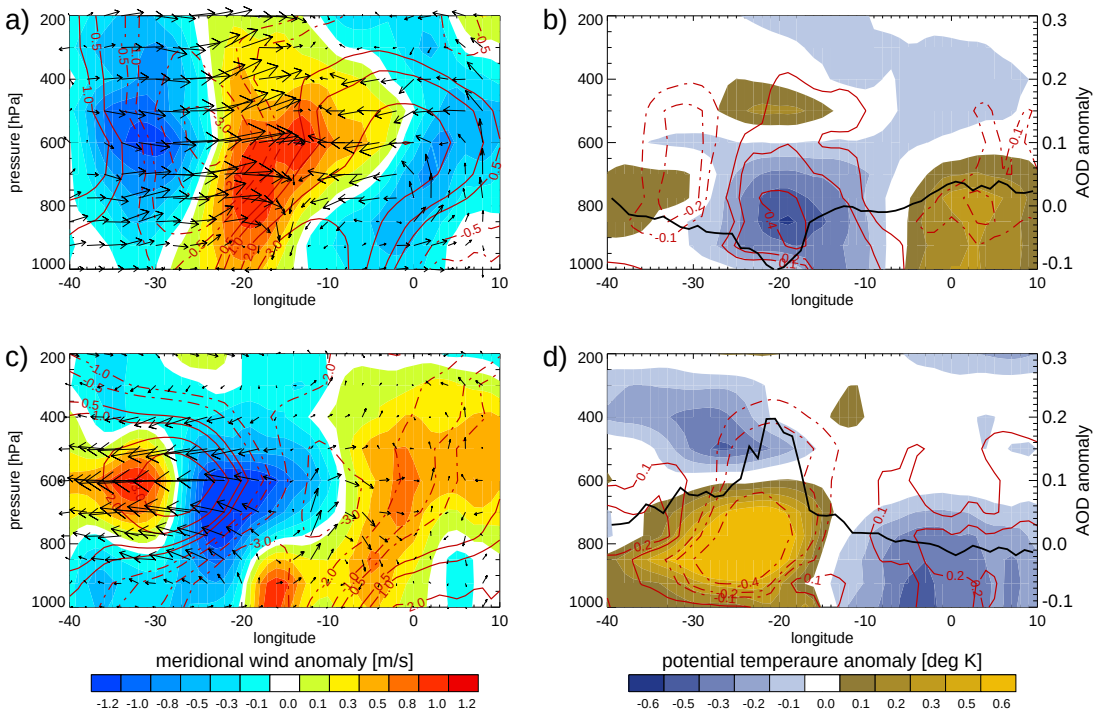

Figure 20: Same as Fig. 19, but based on MODIS-Aqua AOD and within the 5-15 day variability band.

warming and drying in the lower to middle troposphere towards day zero corresponding to the dust-laden heated air emerging from West Africa and moving across the region as the AI and AOD anomalies increases (i.e., black line in Figs. 21b and 22b). Three days later, the situation reverses to positive vertical wind anomalies and a cool and humid atmospheric state as aerosol loading decreases towards its minimum.

4.4 CALIPSO vertical profiles

The Carlson and Prospero (1972) model of the SAL states that after the passage of the heated dust-laden air from the Saharan desert towards the tropical Atlantic Ocean, the mass of air containing dust is elevated towards the 600–800 hPa layer. Using the CALIPSO lidar, profiles of aerosol extinction coefficient at 532 nm (k532, hereafter) were analyzed for the dates of maximum and minimum in aerosol loading within the 5-15 day band variability band as found in the MODIS-Aqua AOD data. It is important to mention that CALIPSO sensor retrieves aerosol profiles in a single trajectory during

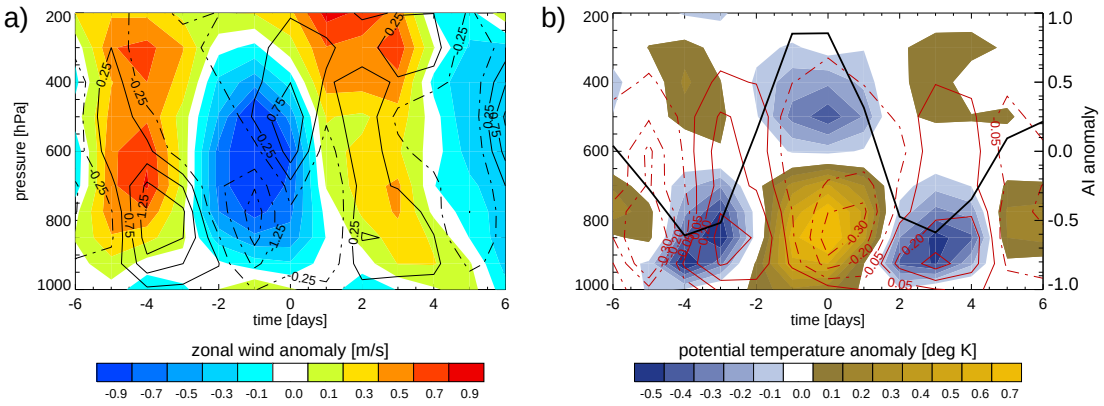

Figure 21: (a) Evolution in time of vertical profiles of zonal wind (shading, relative to the color palette) and vertical wind (contours in [Pa/s], solid line positive value) anomalies from –6 to 6 days around the TOMS-N7T AI maxima in the reference region within the 5-15 day variability band. (b) Similar to (a) but for potential temperature (shading) and specific humidity (contour in [g/kg], solid line positive value). The black line in (b) represent the evolution of AI anomalies over the reference region.

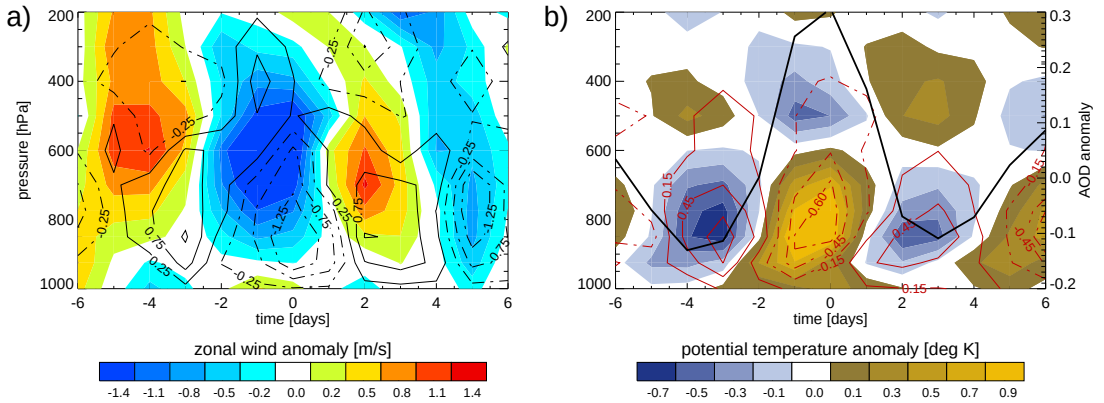

Figure 22: Same as Fig. 21, but based on MODIS-Aqua AOD and within the 5-15 day variability band.

orbit thus limiting horizontal coverage. For this reason, those satellite trajectories in the day of maximum AOD crossing longitudes between 35°W and 15°W closer to the main study region were selected. In general, just one CALIPSO overpass is found per day to correspond to the location of the reference region. A total of 46 CALIPSO sensor overpasses were found during the dates corresponding to the maximum aerosol loading in the period 2006 to 2009. In 40 of those 46 overpasses, an aerosol plume is recognizable up to 400 hPa in height. In the majority of this cases a maximum

concentration is located around 700 hPa. In comparison, the overpasses for four days before the dates of the maximum in aerosol show, in general, smaller values of k532 than in the maximum cases, representing the lower concentration of aerosol dust in the atmosphere prior a high dust event.

Figure 23 shows MODIS AOD anomalies for an example of a case where there is a maximum in aerosol loading occurring in June 23, 2009 together with a minimum in aerosol anomalies on June 19, 2009, four days before. The respective ERA-interim horizontal wind and geopotential height anomalies matching the daily AOD are also shown. Figure 23 also shows the k532 values from CALIPSO overpasses near the study region for the same dates as the MODIS AOD anomalies. Four days before the maximum in AOD (Fig. 23a), there are negative anomalies of AOD and geopotential height that produces cyclonic wind over the region consistent with a low concentration of dust aerosol in the atmospheric column (Fig. 23b). During the day of maximum aerosol loading (Fig. 23c), the anomalies shift to positive AOD and geopotential height values associated now with an anticyclonic circulation. The CALIPSO profile (Fig. 23d) shows a large increase in aerosol loading up to the 600 hPa level with a maximum centered near 700 hPa. This case illustrates where the aerosol plume concentration is located in the vertical during the day of maximum dust over the reference region. The shift between low to high aerosol concentration based on the timing of maximum AOD within the 5-15 day band displays the characteristic progression of dust as discussed before and characterize the elevation of the dust plume up to middle levels of the troposphere.

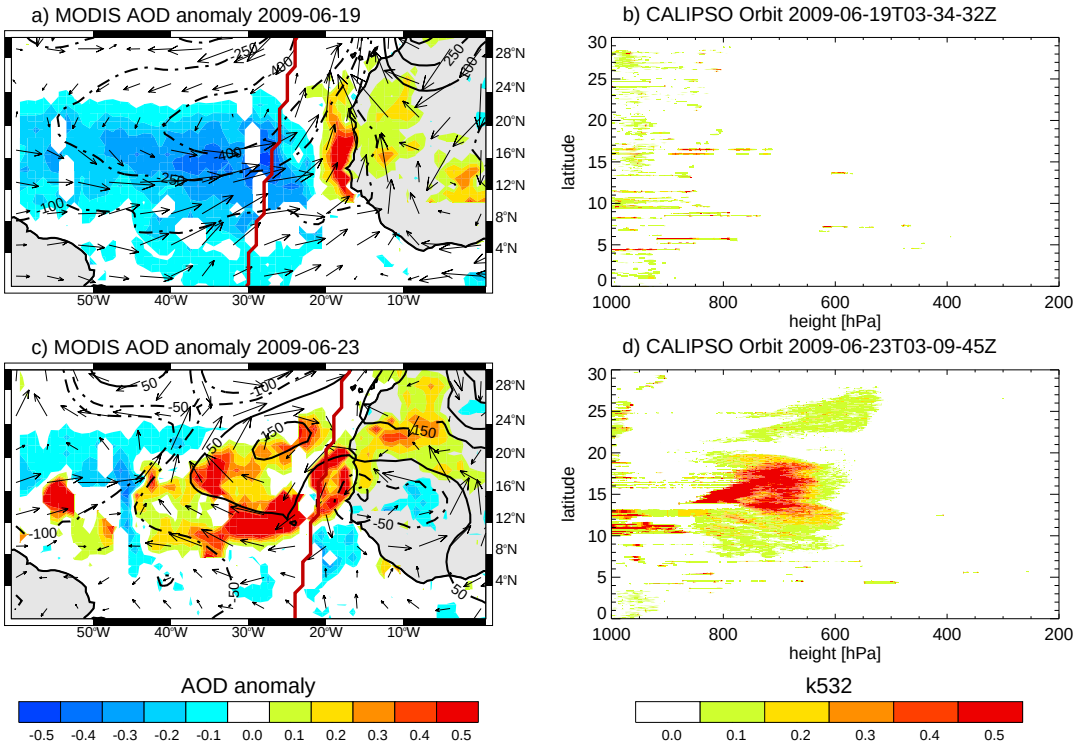

Figure 23: MODIS-AOD anomalies (shading, relative the color palette) and ERA-interim horizontal wind (vectors) and geopotential height (contours in [m], continuous line positive values) anomalies for (a) four days before and (c) during the maximum in aerosol loading for the event of June 23, 2009. (b) and (d) Aerosol extinction coefficient profiles from the CALIPSO lidar for the matching day in (a) and (c), respectively. Notice the path of the sensor trajectory depicted with a red line in (a) and (c) and the shifting of the plot-axis (i.e., height in the bottom axis) in (b) and (d) to match the latitudinal extension in the graphics.

CHAPTER V

EXPERIMENTAL STATISTICAL FORECAST MODEL OF AEROSOL OPTICAL DEPTH

Modeling and prediction of aerosol load are important challenges for the climate community because of its impact on climate and human health. Chemical transport models, in conjunction with general circulation models, have been used to provide different spatial and temporal representations of aerosols distributions on regional and global scales (Jacobson 1997; Tegen and Miller 1998; Chin et al. 2002; Shao et al. 2003; Al-Saadi et al. 2005; Hollingsworth et al. 2008; Heinold et al. 2009; Colarco et al. 2010; Mangold et al. 2011). Several experiments have been proposed to explore diversity in global modeling on the path towards improved aerosol distributions and temporal variability. Among others is the AEROCOM (e.g., Kinne et al. 2006; Huneeus et al. 2010), which deals with the documentation and the assistance of aerosol component modules of global models in order to assemble datasets for model evaluation. While most of these studies have provided good representation of aerosol distributions in seasonal to interannual time scales, the great majority have provided limited representation of aerosol load on shorter time scales such as daily distributions. This lack of temporal resolution limits the possibility of an operational predictive model of aerosol load (Westphal et al. 2009).

The purpose of this chapter is to determine whether or not a statistical forecasting scheme would be useful to represent aerosol loading over the Tropical Atlantic region on daily time scales. In general, AOD (as a measure of aerosol loading) over the Tropical Atlantic Ocean exhibits a coherent pattern of evolution, highly modulated by the large-scale interaction with wind, pressure and temperature, as was described

in Chapter 4. The use of statistical relationships between AOD and atmospheric variables poses a good and simple measure to test the significance of an aerosol forecast skill simulation. The use of a forecast model rather than a traditional chemistry-climate model approach provides a different measure of the AOD simulation skill, allowing a direct comparison of the forecast with an observed event. Statistical prediction models based on regression schemes that couple the joint probability density function between atmospheric processes have been shown to provide useful results. Examples of successful process prediction are the Madden-Julian oscillation (Jones et al. 2004b; Hoyos 2006), hurricanes (Kim and Webster 2010) and river discharges (Webster et al. 2010).

5.1 Methodology

The following section describes in detail the steps involved in the construction of a statistical forecast scheme designed to provide aerosol loading outlooks over the Tropical Atlantic Ocean. The forecast objective variable is the daily MODIS-Aqua AOD during the summer season and over a region close to the coast of North Africa (i.e., 14°N–18°N, 23°W–19°W, box in Fig. 24a). This region is located in the center of the climatological dust corridor, highly influenced by the timing of the westward incursions of African Easterly Waves (see Chap. 4). We use MODIS-Aqua AOD, not only because its ability to represent the aerosol loading over the region, but also because it is a satellite product that is accessible in near real-time. This accessibility provides a potential of an operational forecast scheme of aerosol loading.

The proposed forecast scheme is comprised of a series of regression analyses between atmospheric variables and the MODIS-Aqua AOD time series spatially averaged over the reference region ('AOD time series', hereafter). The regression analysis is motivated by the covariability of large-scale wind, pressure, humidity and temperature anomalies and the aerosol loading over the region discussed on Chapter 4.

The ERA-interim reanalysis is used as a source of predictor variables (i.e., zonal and meridional wind, pressure, humidity and temperature). These predictor variables are selected based on the significance of linear relationships with the observed AOD time series.

5.1.1 Selection of the predictor variables

Correlation coefficient maps were calculated between the averaged daily AOD time series and potential temperature, geopotential height, zonal and meridional wind and humidity observations from the ERA-interim reanalysis at different atmospheric levels (e.g., 925 hPa, 700 hPa, 500 hPa) and with different lag times (e.g., 1 day, 2 day, etc). Figure 24 shows four correlation maps between the AOD time series and potential temperature, zonal wind and geopotential height observations. Summer periods (June–September) over the time span of MODIS-Aqua data were used to compute the correlations. To obtain a representative sampling of the aerosol data, a 3-day running mean of the MODIS and ERA-interim gridded variables was applied to minimize the impact of missing data in AOD retrievals due to sensor swath coverage (see appendix A). Significant positive correlations were found between the AOD time series and potential temperature at 700 hPa over the reference region representing an increase in the mid-level atmospheric temperature as the aerosol load increases, as was discussed in Chap. 4. Figure 24b shows significant negative correlations between 700 hPa zonal wind and the AOD time series south of the center of the maxima in AOD (i.e., between 5°N and 15°N). These negative correlations represent the direct relationship between easterly wind and higher aerosol concentration over the region. Figure 24c shows that the correlation is positive between geopotential height at 700 hPa and AOD over the reference region with a maximum off the coast of North Africa. High pressure systems crossing the region help the dust mobilization as was explained in the composite analysis in Chapter 4. The maximum correlation centered

at [20°N, 20°W] for lag 1 indicates that the linear relationship is maximized in that location when the geopotential height lags the AOD value by one day. In a similar way, the correlations between temperature at 925 hPa and the AOD time series are greatest over the Saharan Desert when the temperature lags the AOD by 3 days. This indicates a warming of the desert surface 3 days prior the increase in aerosol concentration over the reference region. Table 2 shows the center of the locations where the highest correlation coefficient between AOD time series and ERA-interim variables was found.

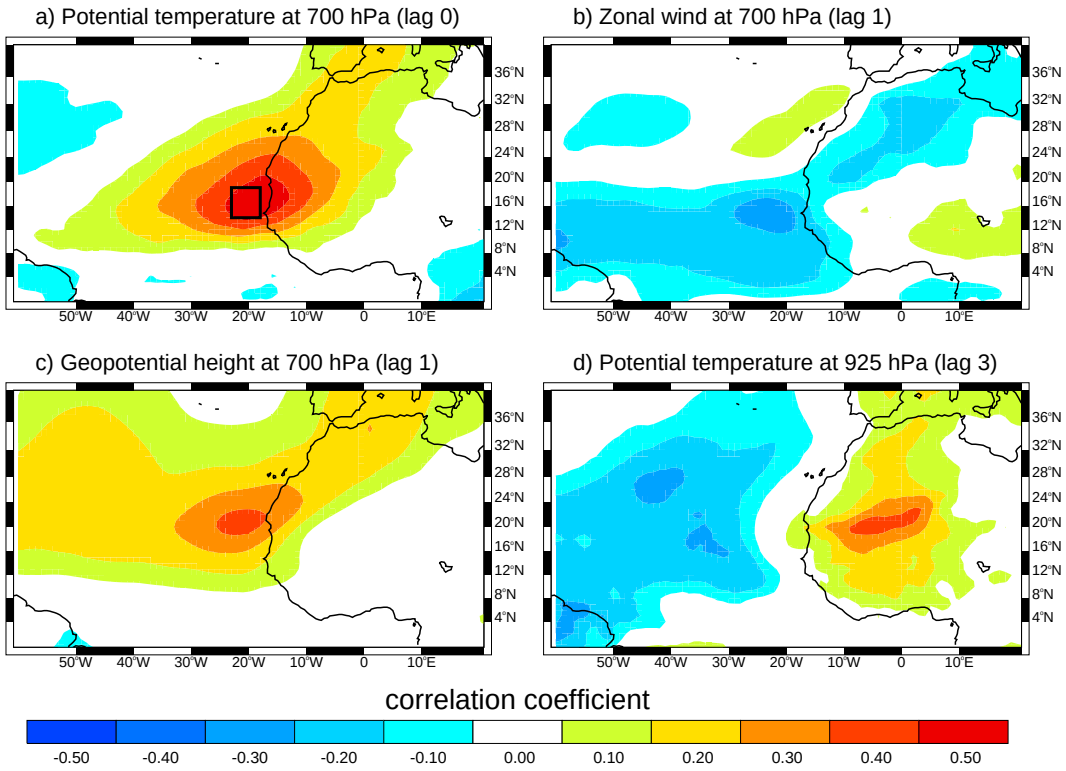

Figure 24: Spatial distribution of the correlation between the AOD time series averaged in the box in Fig. 24 and gridded ERA-interim reanalysis (a) potential temperature, (b) zonal wind, (c) geopotential height and (d) potential temperature time series. The atmospheric level and number of days used to lag each of the ERA-interim variables is indicated in the top caption of each map. Only correlations $> 99\%$ significance level are plotted.

The results of the analysis presented in Figure 24 and Table 2 helps to identify

Table 2: Coordinates of location centers where the correlation between an AOD time series averaged over the reference region and ERA-interim reanalysis variables is maximized. The lag represents how many days the ERA-interim time series is lagged to obtain a maximum correlation.

Location center	Variable	Level (hPa)	Lag (days)	Correlation
(20°W, 17°N)	Potential Temperature	700	0	+0.57
(20°W, 20°N)	Geopotential height	700	1	+0.46
(20°W, 13°N)	Zonal wind	700	1	–0.48
(26°W, 15°N)	Zonal wind	500	0	–0.44
(27°W, 20°N)	Geopotential height	500	0	+0.44
(2°W, 19°N)	Potential Temperature	700	3	+0.45
(22°W, 18°N)	Potential Temperature	500	0	–0.42
(21°W, 22°N)	Meridional wind	925	0	–0.46
(0°, 21°N)	Potential Temperature	925	3	+0.43
(42°W, 26°N)	Geopotential height	925	0	+0.41
(18°W, 20°N)	Potential Temperature	925	0	+0.40
(20°W, 18°N)	Meridional wind	700	0	–0.44
(5°W, 25°N)	Geopotential height	500	3	+0.37

locations and time-lags where the linear correlations between each ERA-interim variable and the AOD time series are maximized (or minimized). We use these locations and lags to identify geographic positions to construct time series of ERA-interim variables to be used as predictor variables in the regression analysis.

5.1.2 Regression analysis models

Five different statistical regression models were used to test the skill of daily forecasts of the MODIS AOD over the reference region. A combination of ERA-interim variables over certain regions and with different time-lags, selected in the previous section were used as dependent variables for the regression models. A brief description of each regression model is provided below:

5.1.2.1 Autorregressive Model

An autoregressive (AR) model of order n can be written as:

$$AOD(t+1) = \sum_{j=1}^{n} \phi_n AOD(t-j+1) + \varepsilon_{t+1} \quad (1)$$

where the left-hand side is the future value of AOD at time $t+1$, ϕ_n are the autoregressive parameters determined by the Yule-Walker equations, n is the order of the AR model and ε is a random component (Wilks 2006). The first four orders of the model were used to validate the AOD forecast.

5.1.2.2 Multiple Regression Model

A multiple regression model (MRM) can be written as:

$$AOD(t+1) = \sum_{p=1}^{n} B_p X_p(t+1) \quad (2)$$

where the left side is the future value of AOD at time $t+1$ and the right side is composed of a combination of n variables selected using the ERA-interim predictors, as explained before. Fitted B_p regression parameters using Eq. 2 are used to forecast AOD at the time $t+1$.

A variation of the MRM is also used and can be written as:

$$AOD(t+1) = \sum_{j=0}^{m} A_j AOD(t-j) + \sum_{p=1}^{n} B_p X_p(t+1) \quad (3)$$

where the left side is the future value of AOD at time $t+1$ and the right side is composed of a combination of n variables based on ERA-interim predictors and additional m parameters regressed from AOD values for previous times. The addition of the regressed AOD into Eq. 2 helps to invoke the memory (i.e., autocorrelation) contained in the AOD time series.

5.1.2.3 Empirical orthogonal function analysis

The use of the Empirical Orthogonal Function (EOF) analysis relies on the decomposition of any large number of variables into a set of fewer new variables, called

Principal Components (PC). These new variables are linear combinations of the original variables, and these linear combinations are chosen to represent the maximum possible fraction of the temporal variability contained in the original data (Wilks 2006). The advantage of this technique is that the original data can be reconstructed by selecting a set of PCs that represent the maximum temporal variability of the physical process. We constructed a set of PCs coming from a combined EOF analysis (for a detailed explanation of the method see Wilks 2006) between the AOD time series and ERA-interim predictors. These PCs describe the time variability of the combined process. We use regression analysis to forecast new realization of PCs that describe the maximum variability. Two types of regression analyses were used. The first, based on an autoregressive model can be written as:

$$PC_k(t+1) = \sum_{j=1}^{m} \phi_j PC_k(t-j+1) + \varepsilon_{t+1} \tag{4}$$

where the left side is the future value of the k^{th} PC, ϕ_j are the autoregressive parameters, m the order of the AR model and ε is a random component as in Equation 1. The second is based on multiple linear regressions of the previous values of PCs, that is:

$$PC_k(t+\tau) = \sum_{p=1}^{m} \sum_{j=1}^{\lambda} B_{pj}(\tau) PC_p(t-j+1) \tag{5}$$

where the left side is the future value of the k^{th} PC for a lead-time τ, λ is the number of lags and m is the number of PCs used in the regression analysis. Notice that there is one forecast equation for each PC obtained from the EOF analysis. Sensitivity analysis can be done by selecting a different numbers of PCs to test the validity of the forecasted AOD.

Finally, after selecting the number of PCs that represent the highest variance of the process and forecasting each PC, the forecasted AOD can be reconstructed as:

$$Y(t+\tau) = \sum_{k=1}^{m} PC_k(t+\tau) EOF_k(Y) \tag{6}$$

where Y represent the AOD forecast for a time τ and EOF_k is the k^{th} EOF associated with PC_k. Notice that the statistical model based on Eq. 5 provides additional forecast for the rest of the ERA-interim variables involved in the construction of the combined EOF. In this work, we only focus on the forecast of the AOD time series.

5.1.3 Experimental setup

The experimental setup allows an assessment of forecast skill of AOD time series using the regression models described in the previous section. Time series of MODIS-Aqua AOD for the 2002 to 2009 summer periods (i.e., June–September) were used as independent variables in each regression model. In addition, time series for different ERA-interim variables selected for the locations shown in Table 2 were used as dependant variables for the multiple regression models. These ERA-interim variables were averaged in daily time series for the 2002 to 2009 period, and within a box of 4° x 4° centered at the location shown in Table 2, to match period and reference region as the AOD time series. The regression model parameters were calibrated using the dependent-independent variable setup (i.e., the model development period) previously described. We reserved the summer period of 2010 for the validation period. The parameters calibrated during the development period are used in the regression models to forecast AOD during the 2010 season. Series of 10-day forecast are initialized each day consecutively during the validation period. The 10-day forecast is compared with the original data during the 2010 validation period in order to assess the error of the simulations. This set of experiments allowed a detailed study of the error growth and the propagation as function of time (Hoyos 2006). The application of this type of experiment has been used extensively and with great success to make precise assessments of the forecasting skill of different models (Jones et al. 2004b; Hoyos 2006; Agudelo et al. 2009; Kang and Kim 2010). Finally, different combinations of predictors, day-lags and the use of the anomalies of the AOD and ERA-interim predictors

were used to test the sensitivity of the forecast to a different combination of model arrangements. The sensitivity test will be described later with the results of this section.

Two different statistics are used to compute the forecast skill of the different regression models. Correlation and root mean square error (RMSE) at different lead times are estimated in order to evaluate the phasing of each model results relative to the observations, and the deviation of the integrations from the observations (i.e., absolute error), respectively. The RMSE estimation used here is scaled by the standard deviation of the observations. In this way, when the scaled RMSE is equal to one for certain lead-time, the magnitude of the forecast errors is equal to the amplitude of the signal and after that lead-time there is no subsequent skill in the forecast (Hoyos 2006). Both statistical metrics are estimated for the raw and for the anomalies of the observational data, and with the different combination of model arrangements in order to evaluate the extended forecasting skill.

5.2 Analysis of the forecasting skill

Figure 25 shows the correlation and standardized RMSE for MODIS-Aqua AOD at different forecasting lead times using the AR model described in Eq. 1. Two model runs are presented for autoregressive order of 1, 2, 3 and 4 to compare the statistical significance of the AR forecast model. In both cases, the correlation decreases rapidly with the increase of the forecast lead-time. The correlation of the forecast for the 1^{st} day is related linearly with the observations only in 60%, and after the 2^{nd} day the correlation decreases down to values below statistical significance. Similarly, the standardized RMSE grows rapidly for larger lead-time and is minimum for only the 1^{st} day of forecast (i.e., around 0.8). After the 2^{nd} day, the RMSE grows beyond the one unit value indicating poor skill in the forecast. Figure 25 also shows that with an increase in the order of the AR model there is no improvement in the RMSE

skill of the predictions. The only improvement is that the correlation between the observations and the forecast for different lead times increases as the order of the model increases. The increment in the correlation is only produced by the increase of the statistical memory that the higher AR model order provides.

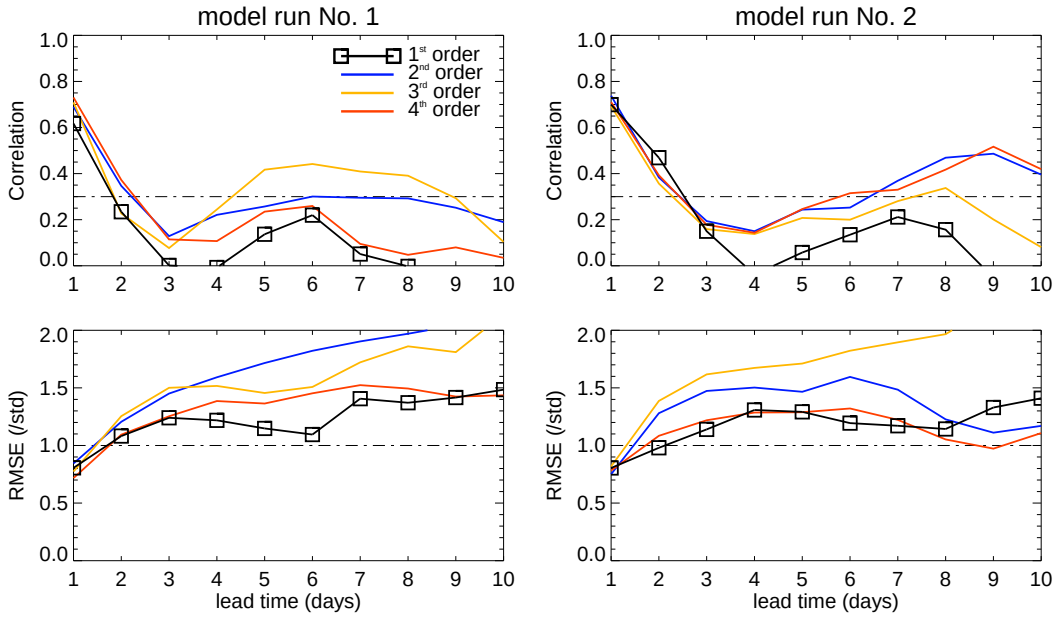

Figure 25: Correlation and standardized root mean square error for MODIS-Aqua AOD at different forecasting lead times using an autoregressive model. Two model runs are presented, one shown in the left panels and the other in the right panels. The continuous black, blue, yellow and red lines correspond to AR model of order 1, 2, 3 and 4, respectively. The RMSE is standardized by the observational standard deviation during the forecasting period. The horizontal dashed line in the correlation diagram corresponds to the 99% significance level.

Figure 26 shows the correlation and standardized RMSE of the AOD forecast using an autoregressive model of PCs forecast calculated from Equations 4 and 6. Different combinations of ERA-interim predictors were used in the calculation of the PCs using EOF analysis. Figure 26 shows two cases, one using the first three time series shown in Table 2 (i.e., potential temperature, geopotential height and zonal wind at 700 hPa) and the second case using the first ten time series in Table 2. In addition, the forecast skill was tested using a different number of PCs in each EOF analysis (i.e., varying the value of k in Eqs. 4 and 6). The correlation is not significant

and RMSE is greater than the unity value for almost all the lead times in Fig. 27. Poor forecasting skill is apparent even when increasing the number of predictors or the number of PCs. In contrast, the correlation and the RMSE were improved when multiple linear regressions of the previous values of PCs were used using Equations 5 and 6. Figure 27 shows the forecast skill using multiple linear regressions with the same arrangement as Fig. 26 (i.e., using 3 and 10 predictors and 5 and 10 PCs). The use of PC forecast based on linear regression of previous PCs provided better forecast skill compared to those presented in Figures 25 and 26. It can be noticed that the increase in number of predictors and PCs (e.g., 10 predictors and 10 PCs) results in an increase in correlation and a decrease in RMSE for up to the 3^{rd} lead-day (right panel in Fig. 27). The inclusion of lagged PCs in the regression forecast (i.e., increasing λ in Eq. 5, colored lines in Fig. 27) gives a small positive increment in the correlation and a small decrease in the RMSE.

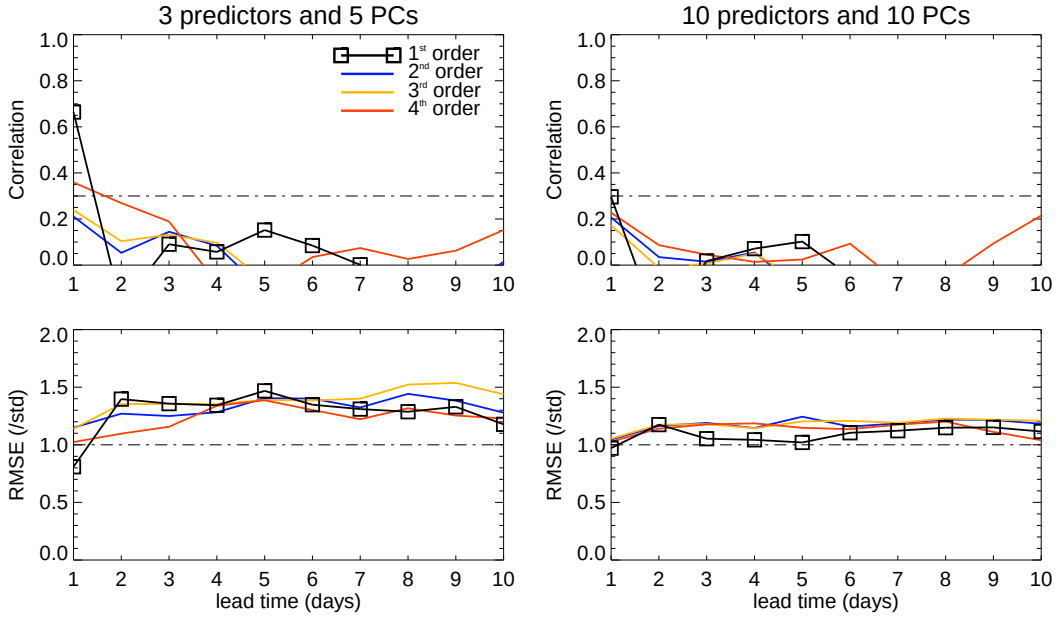

Figure 26: Same as in Fig. 25, but using an autoregressive model of PCs forecast. The left panel corresponds to the result using the 3 first time series shown in Table 2 and using 5 PCs forecast. The right panel corresponds to the result using the 10 first time series shown in Table 2 and using 10 PCs forecast. The colored lines correspond to AR models of order 1, 2, 3 and 4 as shown by the caption in Fig. 26a.

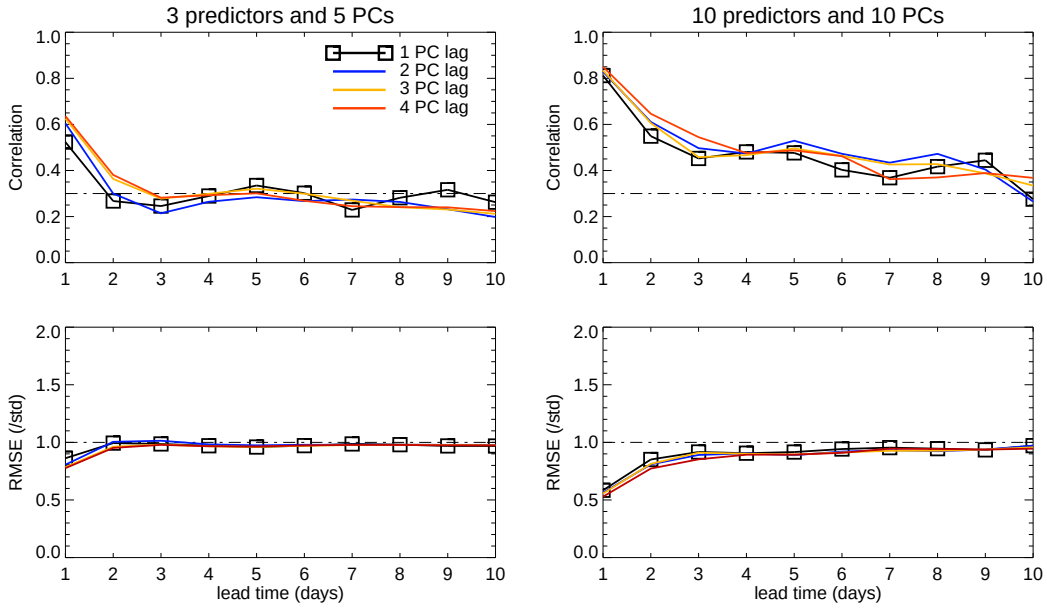

Figure 27: Same as in Fig. 26, but using a multiple linear regression model for PCs forecast. The continuous black, blue, yellow and red lines correspond to the regression using 1, 2, 3 and 4 lagged PCs (i.e., increasing λ in Eq. 5), respectively.

Figure 28 shows the forecasting skill of AOD using the multiple regression model described by Equations 2 and 3. The correlation and the RMSE were calculated using the regression model with the three first time series shown in Table 2 (left panel in Fig. 28) and with the first ten time series (right panel in Fig. 28). The skill of the AOD forecast using a multiple regression model based only on ERA-interim predictors (i.e., Eq. 2) produces poor results compared to the same regression model with the inclusion of regressed AOD variables as predictors (i.e., Eq. 3). The inclusion of regressed AOD variables as predictors increases the correlation for the first day of the forecast up to 0.8 and decreases the error down to about 0.6 (blue lines in Figs. 28a, b). However, the skill is very poor after day 3 of forecast lead-time. There is a very small increment in forecasting skill with the inclusion of more predictors in the regression model (e.g., from 3 to 10 predictors) and with the inclusion of previous AOD values (e.g., increasing m in Eq. 3).

The results presented in Figure 25–28 were calculated using the raw observations

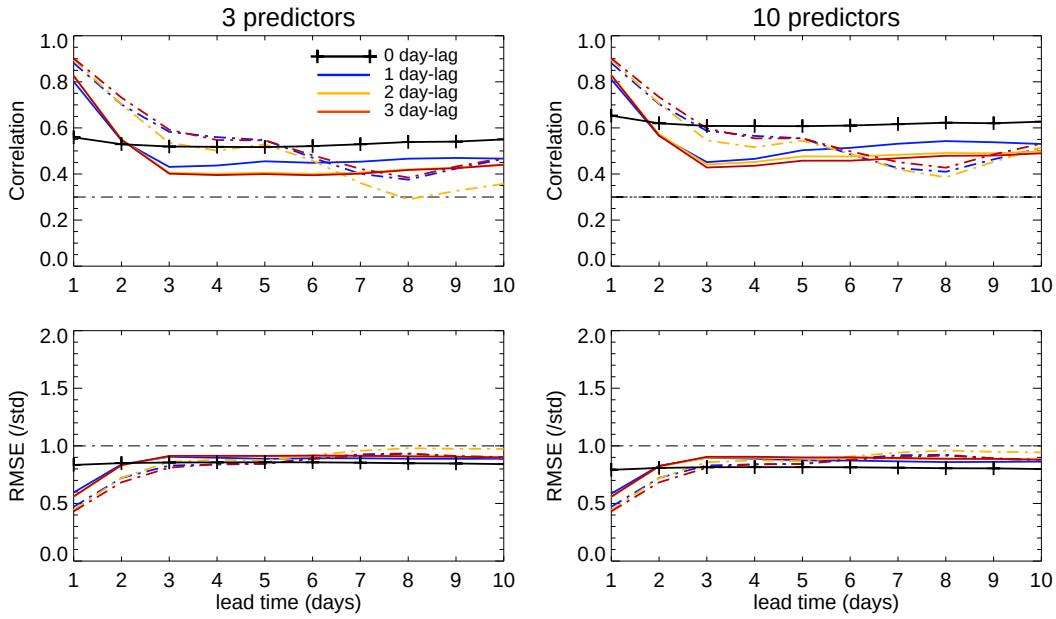

Figure 28: Same as in Fig. 25, but using multiple regression models. The black line corresponds to the regression model defined by Eq. 2, and using raw observations. Colored lines correspond to the regression model defined by Eq. 3, and using 1 (blue), 2 (yellow) and 3 (red) day-lag AOD. Solid lines correspond to the forecast skill using raw observations and broken lines using anomalies of the observations.

to test forecast performance of different regression models. In a similar way, instead of using the raw observations we use anomalies of AOD time series and ERA-interim predictors in order to test model sensitivity. Only the results for the multiple regression model (i.e., Eq. 3) are presented because they represented the only improvement of forecast skill compared to previous models. The broken lines in Fig. 28 show the forecast skill improvement. Correlation up to 0.9 for the first day of forecast and RMSE about 0.45 is given by the forecasting of AOD anomalies using the regression model of ERA-interim predictors and regressed AOD as in Eq. 3. Finally, the inclusion of more predictors and previous AOD values does not provide a significant increment of the forecast skill as shown by the solid lines in Fig. 28.

5.3 Discussion

The use of a multiple regression model in the forecasting of anomalies of AOD time series with the use of ERA-interim variables as predictors, gives a useful forecasting skill up to three days of lead-time as was shown in Fig. 28. This model was the only one of the five models analyzed that would provide a useful forecast. The three-day value was smaller that the one would expect considering that the AOD exhibits a coherent pattern of evolution, highly modulated the timing of the African Easterly Waves (e.g., 3–9 days) that modulate the AOD distribution over the region. We speculate some reasons why the forecast had poor skill using the regression models presented in Figs. 25–28.

The use of a smaller region for the averaging of AOD time series would lead into the presence of higher variability the series that will make hard for the statistical forecast to be able to give significant results. However, sensitivity analysis was made increasing the area of the reference region by a factor of two (i.e., 12°N–22°N, 28°W–18°W). Figure 29 shows the forecasting skill of AOD anomalies based on this bigger region and using the multiple regression model described by Eq. 3 (similar as Fig. 28). The correlation and RMSE values are slightly improved; the correlation for the first day of the forecast is about 0.9 and the RMSE is about 0.4. However, the skill is still poor after the 3^{rd} day of forecast in similar way as the skill presented in Fig. 28 and using a smaller region. In conclusion, the forecasting skill is not improved with the use of a bigger region to construct the time-series average.

The non-linearity of the process that is hard to capture with the use of multiple linear regression models. Figure 30 shows scatter plots between the AOD time series and the three first ERA-interim variables in Table 2 used as predictors in Figs. 27–29. The use of a regression model always assumes linearity between the variables involved in the regression. In fact, Fig. 30 shows that a linear regression is not the best way to describe the relationship between the AOD time series and potential

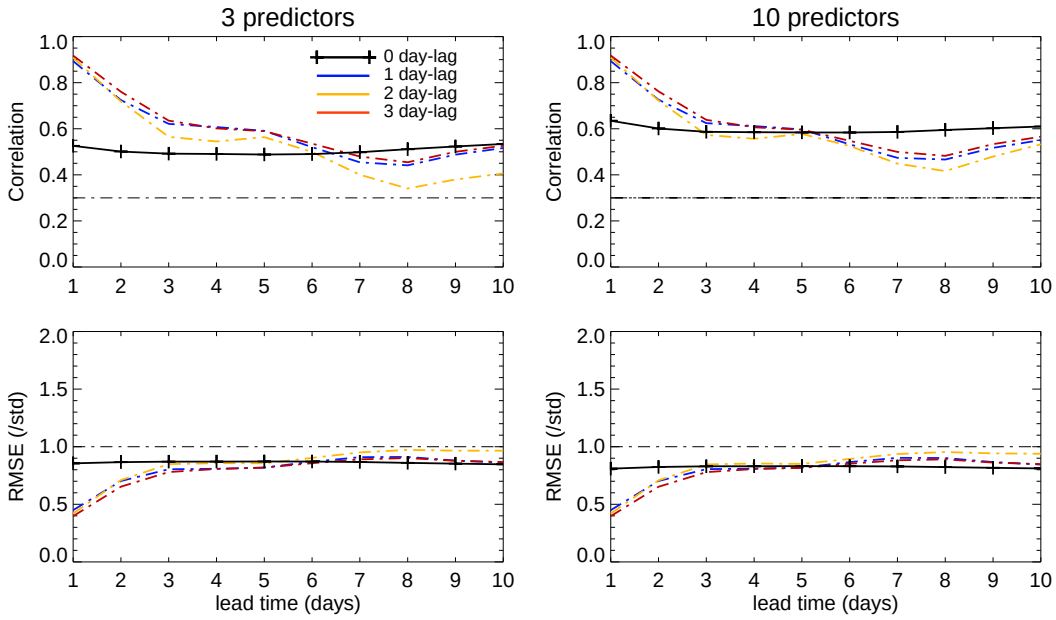

Figure 29: Same as Fig. 28, but using a multiple regression model to forecast AOD anomalies. Time series used to construct the regression model are averaged in a bigger region than the region used for Fig. 29 (i.e., 12°N–22°N, 28°W–18°W).

temperature, geopotential height, and zonal wind at 700 hPa. One possible solution to improve the forecast using regression models would be that instead of using the full time series as predictors to construct the linear regression, split the time series in parts to improve the linearity of the regression coefficients. This would help to capture the non-linearity of the relationship using different regression coefficients for different values of the AOD in the regression models.

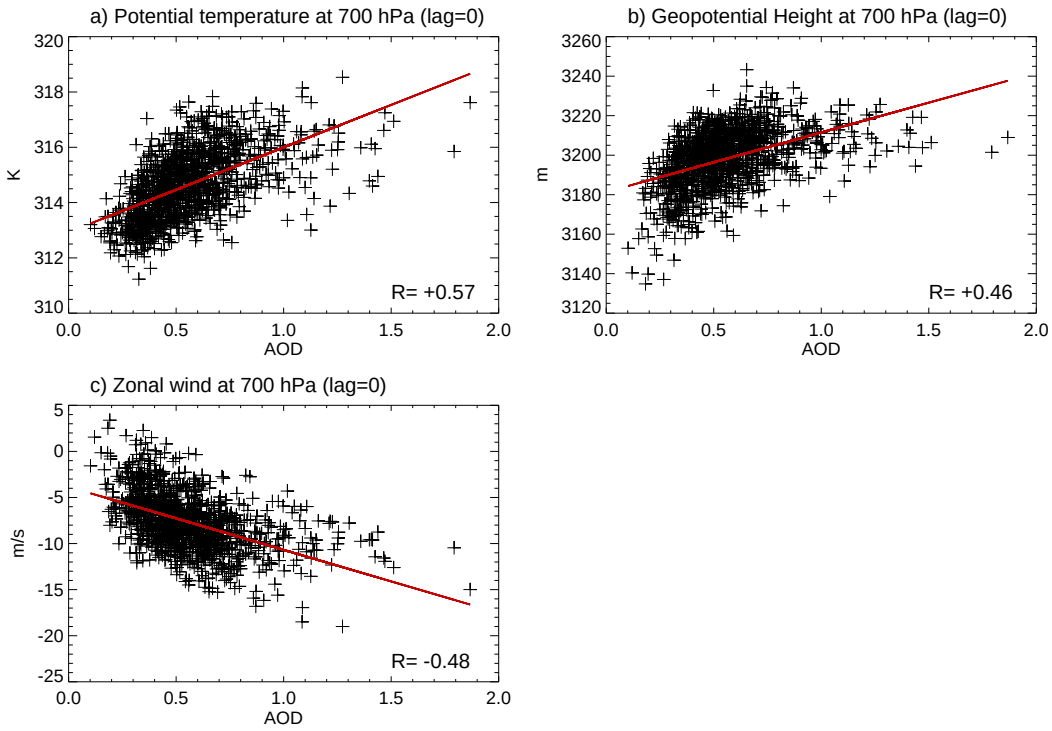

Figure 30: Scatter plots of AOD and (a) potential temperature, (b) geopotential height, and (c) zonal wind time series used as predictors for the 3 first locations in Table 2. The level and time-lag of each ERA-interim time series are indicated on the top of each diagram. The red line corresponds to the linear fit and the correlation coefficient is indicated at the bottom of each plot.

CHAPTER VI

CONCLUSIONS

In order to determine the impact of aerosols on weather, climate and air quality, a basic analysis of aerosol loading relative to the atmospheric and ocean environments is undertaken. A large database of remotely sensed aerosol loading is used to analyze the spatio-temporal variability of aerosol load in the tropics and to explore how this load interacts with the dynamic and thermodynamic states of the environment. We base the analysis on the use of seven satellite derived aerosol products to compile a long and diverse aerosol database. The diversity of this database results from the different retrieval techniques and calibration procedures inherent to each satellite product. Aerosol Index and Aerosol Optical Depth (defined in Chapter 2) are used as measures of the atmospheric aerosol load. The analysis uses the strength of each dataset separately to provide a general picture on how the aerosols vary across different regions around the world and how this variability relates with the atmospheric and oceanic environments.

Comparisons of the distribution of the aerosol load between TOMS AI and MODIS AOD, find similar characteristics on the representation of the main sources of aerosol across the Tropical Atlantic, South Africa, Middle East, and parts of South Asia regions. Both products are able to represent the maximum values of aerosols, especially for those regions affected by dust and biomass burning aerosols. In addition, there is similitude in the representation of the asymmetry in latitudinal distribution of aerosols between the Northern and Southern Hemispheres. The greatest difference in the aerosol distribution between datasets is found over the South Asia and eastern China regions. We hypothesize that the high diversity of aerosol types that affect

these regions and the different retrieval technique between AI and AOD are perhaps the reasons why the datasets do not agree.

We selected six regions across the globe to compare the spatio-temporal variability of aerosol distributions. High interannual and intraseasonal variability is seen over the Tropical Atlantic Ocean, North Africa, South Africa, Middle East, South Asia, and East China regions. As with the spatial distributions of AI and AOD, time series share notable similarity over the Tropical Atlantic Ocean, Middle East and South Africa, but less similarity over South Asia and East China. This difference among retrievals confirms that in continuous long-term retrieval of aerosol distributions, it is critical to select the proper aerosol retrieval technique for a particular region of interest. Without such selection, discrepancies may arise even with the use of more advanced aerosol retrieval techniques, such as those used by the MODIS and the MISR sensors.

Several studies have used aerosol satellite datasets to analyze regional or global average aerosol trends. Instead of computing an average trend, we use a non-parametric technique (i.e., Mann-Kendall) to study the spatial distribution of aerosol trends over the 45°N to 45°S latitudinal band. Positive AI tendencies are found over much of the tropics from 1979 and 1984. From 1987 to 1992, the positive tendencies remained over South Africa, Middle East, South Asia and Australia; whereas over the Tropical Atlantic Ocean and Northern Africa negative AI tendencies are seen. Negative aerosol tendencies continue to be seen over North Africa, the Mediterranean Ocean and Europe when calculated using AOD from MODIS and MISR during the 2000s. The positive tendency over the Middle East, Arabian Sea and South Asia is reported to have been strongly influenced by an increase in dust events, while the changes in aerosol tendencies over the Mediterranean Ocean and Europe has been attributed to changes in aerosol emissions governed by economic developed nations and air pollution regulations. Even if the analysis reports considerable tendencies over the South

Pacific Ocean, South Atlantic and Australia regions, more study is needed in order to evaluate the significance of the trends. Is hypothesized that satellite aerosol retrieval deficiencies such as cloud contamination and sun glint may affect the results on these areas.

The results reported in the Chapter 4 provide analyses describing how the climatological African Easterly Wave variability modify the dust aerosol burden in the Tropical Atlantic region and how the environment is modified by dust intrusions. The use of the ECMWF-ERA reanalysis, and satellite observations of atmospheric and oceanic variables help to characterize the co-variability of aerosol dust. Two modes of westward aerosol propagation are apparent in both TOMS AI and MODIS AOD datasets, one with a period near 5–7 days and another with a period near 9–11 days. These two regimes represent the wave speeds of the two AEW forms crossing the region. The modes of aerosol variability were tested with the use of two different spectral techniques to investigate the statistical significance. Good correspondence is found between positive 700 hPa geopotential height anomalies and positive aerosol anomalies, each sharing the same periodicity. In a similar fashion, wind vector anomalies show that the direction of circulation changed depends on the timing of the maximum/minimum aerosol anomalies over the region. As positive anomalies of aerosol increase towards the day of maximum loading, there is a reversal from easterly to westerly in zonal wind direction, a change of sign from negative values (low pressure) to positive values (high pressure) in geopotential height and an increase towards a maximum in wind speed. While the pattern progression of the propagation of aerosol load has been validated before using reanalysis models and satellite observations (e.g., Karyampudi et al. 1999), we present extensions to these studies; Evaluating the performance of the long series of satellite aerosol retrievals into the determination of the modes of aerosol variability in relation to the two forms of AEW, using reanalysis and satellite retrievals of atmospheric and oceanic variables

to show how the atmosphere and the ocean are impacted by dust aerosol variability, and documenting how those impacts are represented in the Carlson and Prospero (1972) model for dust transport over the Atlantic Ocean.

The environmental impact produced by the variation of aerosol loading on the surrounding atmosphere and ocean shows a decrease towards minimum values of SST, precipitable water vapor and rainfall rate and to a maximum in OLR as aerosol loading increase over the study region. These changes are in concert with a reduction in precipitation, humidity and surface shortwave radiation as a warmer and drier dust plume is transported over the desert surface towards the Atlantic Ocean. These characteristics are apparent independent of the use of a particular aerosol dataset (i.e., TOMS-N7T or MODIS-Aqua) or the period of analysis (i.e., 1979–1993 or 2002–2010).

The vertical state of the atmosphere during the evolution of aerosol loading is also investigated. Four days before the maxima in aerosol is reached in the study area, a middle troposphere cyclone characterizes the atmosphere near the latitude of minimum aerosol loading. We hypothesize that the subsidence, located in the same place as the minimum in aerosol, acts to prevent aerosol build up. At the same time, the atmosphere is also found to be cool and humid. However, during the day of aerosol maximum, the middle level circulation reverses towards an anticyclonic flow with the development of a middle level easterly jet, characteristics of the favorable conditions for dust transport over the Atlantic Ocean. The previous cool and dry lower- to middle-level atmosphere is then replaced by an anomalously warm and dry air mass forming a temperature inversion around 875 hPa near the base of the SAL. This change in structure occurs with a continuous transition from cyclonic to anticyclonic circulation, a shift between negative to a positive geopotential height anomalies, a shift from positive to negative vertical velocity and with a considerable warming and drying of the lower-to-middle layers of the atmosphere. Moreover, the evolution of these variables occurs with the same temporal scale as the AEW passing thought

the region. The vertical extension of aerosol extinction coefficient provided by the CALIPSO profiles show that during most of the cases where there was a maximum in AOD values over the study region, the aerosol plume reached a maximum concentration around 700 hPa. In contrast, smaller values of aerosol extinction coefficient are found for events during the fourth day prior to the maximum in AOD over the study region.

The analysis described above suggests the existence of a coherent evolution pattern between the aerosol load and the dynamics of the atmosphere, and ocean over the Tropical Atlantic region. This covariability motivated an experimental exercise to use five statistical regression models to test the significance of the forecasting skill of daily AOD time series. The regression models are calibrated using atmospheric variables as predictors from the ERA-interim reanalysis. The predictors are selected based on the significance of linear relationships with the observed AOD time series. We find that time series of potential temperature, geopotential height and zonal, and meridional wind located in certain regions and with different time-lags correlate well with the AOD time series. A serial integration experiment is designed to evaluate the forecasting skill of the regression models, and correlation and root mean square error are used to compute the skill.

Poor forecasting skill was found when we use autoregressive models and the model based on principal component forecast, with errors growing after the 2^{nd} day without subsequent skill. The only improvement in the forecast skill, up to three days of lead-time, was appreciable with the use of a multiple regression model to forecast anomalies of AOD time series. The three-day value is smaller than the one that would be expected considering that the AOD exhibits a coherent pattern of evolution, highly modulated the timing of the AEW (e.g., 3–9 days) that modulate the AOD distribution over the region. We test the sensitivity of the forecasting skill with the increase in the area of the region for the averaging of AOD variables and find that the

skill is not improved. We speculate that the non-linearity of the aerosol variability process is hard to capture with the use of linear regression models. The scatter plots constructed between the selected AOD and the ERA-interim predictors time series showed the poor linearity between these variables. One possible solution to improve the linear-based forecast is that instead of using the complete time series as predictors to construct the linear regression coefficients, use parts of the series that represent linearity to calculate the regression coefficients.

Future research work should explore physical reasons of why the distribution of aerosol tendencies changes thought the years and include sensitivity of aerosol retrievals that affect the results. The use of reanalysis data will be helpful to construct interannual relationships of aerosol-environment. In addition, the methodology used to investigate the covariability between aerosols and dynamic and thermodynamics variables can be extended to other regions of the globe (e.g., South Africa or the Middle East). However, it would be necessary to differentiate aerosol type in the analysis for regions affected by multiple sources of aerosols. The use of the capabilities of the MODISs fine fraction in conjunction with the aerosol scene classification product of CALIPSO sensor can be useful in order to differentiate the distribution of aerosol type over diverse regions of the globe. A better refinement on the statistical forecast is suggested including not only changes in the linear methodology but also the inclusion of surface process variables such as wetness, vegetation cover, wind speed and rainfall as source predictors variables in order to increase the representativeness of dust mobilization and dust transport over any region that is affected by dust events.

APPENDIX A

SENSITIVITY OF MODIS-AQUA SAMPLING PATTERNS TO SPECTRAL VARIABILITY MODES IN AEROSOL TIME SERIES

Quantitative analyses of aerosol satellite data products require a good understanding of the uncertainties of the aerosol optical depth (AOD) retrieval algorithm, as well as a detailed knowledge of the temporal and spatial sampling of the aerosol products. Uncertainties in the retrieval algorithm (i.e., the quality of the MODIS AOD value) are generally assessed by comparing satellite data to *in situ* ground observations. Such comparison had been previously conducted (Remer et al. 2005) and it was found that the satellite AOD retrievals agree with the ground observations.

Since the aerosol statistics (e.g., generation of daily time series of AOD for a particular region) are created based on incomplete samples with spatially and temporally inhomogeneous field (Levy et al. 2009), one needs to investigate the uncertainties in the sampling aggregation of the AOD. For example, MODIS AOD values are derived only during clear-sky conditions, with missing values for non-visible locations (e.g., overcast) and at night time. Figure 31a shows an example of the typical AOD data coverage for one day over North Africa and tropical Atlantic Ocean from the NASA Earth Observing System platform dataset (http://ladsweb.nascom.nasa.gov/, see Chapter 2). In addition, the polar orbit of MODIS satellite exacerbates the gap in some regions of the tropics and the poles because the interaction between the orbital geometry and the swath coverage of the sensor, leaving such regions without retrieval (Levy et al. 2009). Therefore, the data coverage of MODIS sensor during certain times of the day leads to spatially and temporally non-uniform and incomplete AOD

sampling. These sampling biases have been evident in climatologies of monthly aggregation of MODIS-Aqua and MISR AOD (Leptoukh 2010). Sampling biases lead to "pulsating data" when temporal and spatial average maps are compiled. This is apparent especially over the ocean, affecting the time variability of the MODIS AOD aggregations (G. Leptoukh 2010, personal communication). Such pulsating areas may affect the temporal representativeness of the sample and induce spurious frequencies into the AOD analyses.

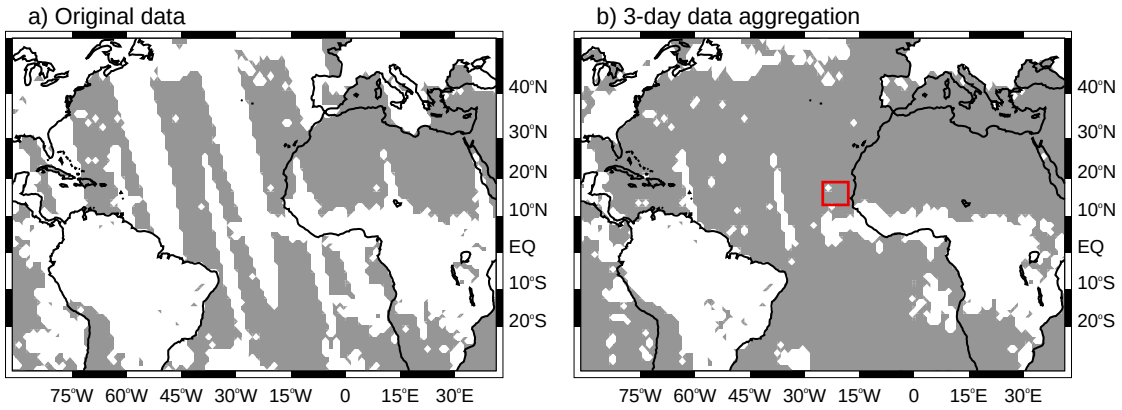

Figure 31: Coverage of MODIS AOD data during July 10, 2004 for (a) original data and (b) for the 3-day running mean aggregation. Grey regions in maps represent areas with daily AOD retrieval, while white regions indicate *missing values*. The red box in (b) represents the region basis of the spectral analysis.

In order to test how much the modes of variability calculated in Chapter 4 are affected by data availability, a set of data simulations was performed. The simulation procedure is now described: We first construct synthetic time series of known periodicity (i.e., a sinusoidal function) and with similar spatial and temporal characteristics of the MODIS AOD dataset (i.e., 1° x 1° grid resolution and covering the MODIS-Aqua period). Thus, these synthetic AOD-like series have known theoretical periodicity. This set was next aggregated using a 3-day running mean in a similar manner to that described for the spectral analysis section in Chapter 4. Next, the real coverage of the MODIS AOD data used in Chapter 4 (i.e., the original daily AOD with a 3-day running mean aggregation) was superimposed on the synthetic

data set. Figure 31b shows an example of the increase in AOD data coverage after using the 3-day running mean for the same day as in Fig. 31a. With this combination we guarantee an increase in data coverage although, at the same time, variability on time scales of less than 3 days cannot be resolved. The effect of the MODIS AOD coverage aggregation on the time variability of the modes was investigated using different combinations of synthetic deterministic periodicities. The modes of variability for each time series were calculated using the same Fourier spectral technique as in Chapter 4.

Figure 32a shows a simulated daily time series with two known periods, 5 and 10 days (black dashed line). A 3-day running mean was applied to the time series (black solid line). The MODIS-AOD coverage over spectral analysis test region (i.e., 15°N–17°N, 22°W–20°W, box in Fig. 31b) was then applied *keeping* the simulated value when there is AOD retrieval in the daily MODIS time series. Instances with no AOD retrieval were set to a *missing value* indicator. The red line in Fig 32b represents the simulated time series after the application of the AOD coverage. The missing values were then estimated using nearest neighbor interpolation (Fig. 32c). A spectral analysis was performed to obtain the modes of variability. Figure 32d represents the power spectrum of the 3-day running mean and known periodicity time series. As expected, spectral peaks at 5 and 10 days are very apparent in the power spectrum. Figure 32e shows the power spectrum for the time series in which the AOD coverage and interpolation was applied. The power spectrum analysis shows similar peaks at 5 and 10 days. This indicates that the aggregation of 3-day running mean data and interpolation of the missing values are not affecting the main modes of variability of the original data. The same procedure was used for other periodicities and similar results were obtained, with no significant change of the modes of variability after the application of the MODIS-AOD coverage. The only noticeable change in these simulations is that the variance of the power spectrum is reduced by the application of

data aggregation. In our case, this does not affect the results since the focus is on the periodicity of the events (in relationship to the African Easterly Waves periodicity) and not on the amplitude of the variance obtained with the spectrum analysis of the aerosol data.

To evaluate further the influence of AOD data aggregation in the spectral analyses, the spatial distribution of the simulated main modes of variability were investigated. The same procedure mentioned above was used to test the data aggregation for synthetic time series in each of the 1° x 1° pixels of the region shown in Figure 33a. Figure 33 represent the results of the simulation using known periods of 5 and 10 days and only the spatial distribution of the highest three explained variances are presented in the left panel of Fig. 33. In addition, the corresponding resolved period for each maximum explained variance is presented on the right of Fig. 33. Periods higher than those presented in Fig. 33 were not considered since they represent a small percentage of the variance and hence, are not significant. Figure 33b shows a characteristic period of 10 days over mostly all the Tropical Atlantic and North Africa regions corresponding to the highest resolved period that the Fourier analysis provides. In similar way, for the second maximum variance, a period of 5 days is appreciable over the Tropical Atlantic and North Africa regions (Fig. 33d). The third highest variance is also representing the 10-day periodicity originally assumed (Fig. 33f). These results show that the modes of variability obtained after the aggregation analysis are equal to those originally assumed (i.e., 5 and 10 days). In addition, the maps do not show significant spatial variability in the order of the resolved modes. In conclusion, the data aggregation did not affect the time representation of the sample, and thus did not affect the resolved modes of variability obtained with the spectral analysis.

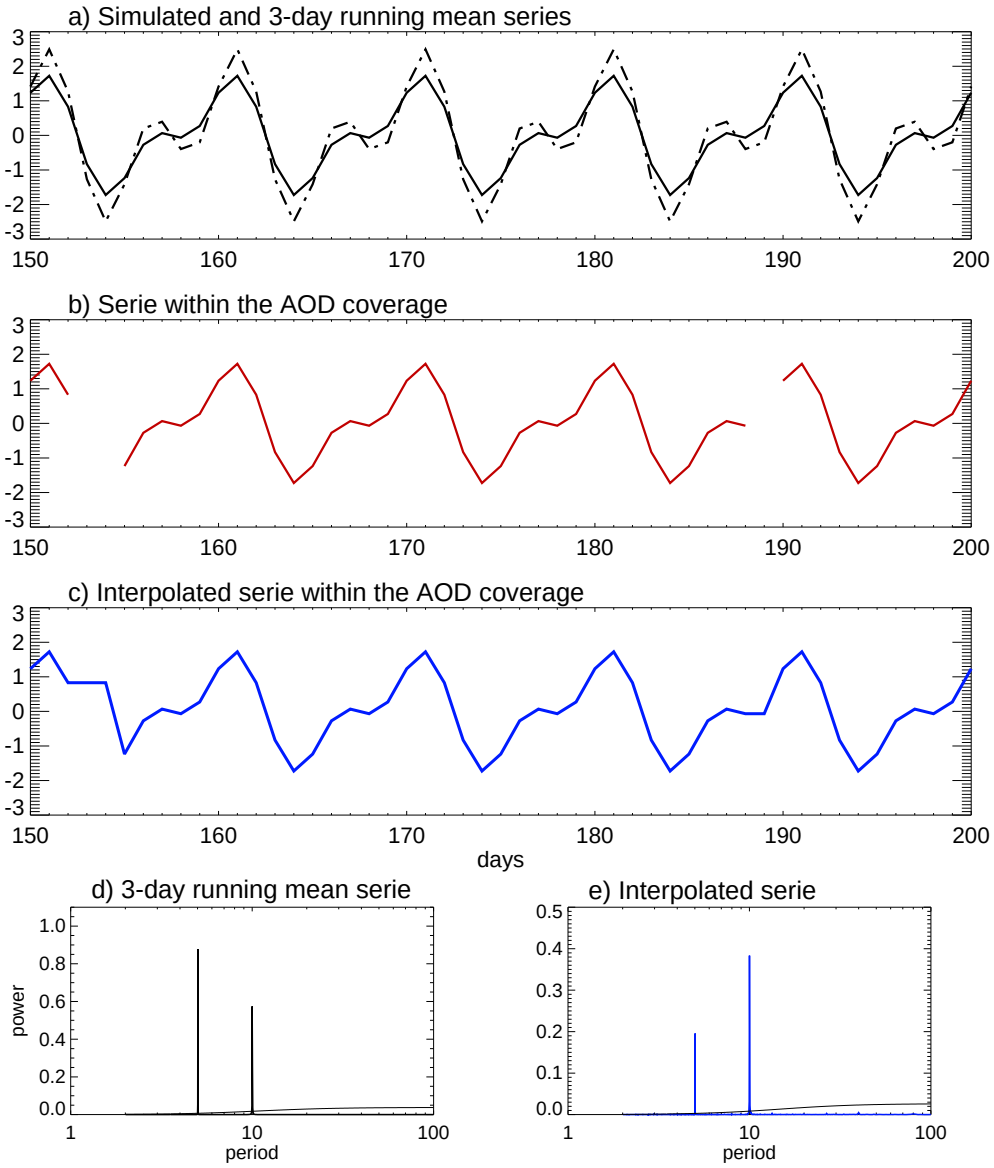

Figure 32: (a) Simulated daily time series (black dashed line) with two known periods (i.e., 5 and 10 days) and after applying a 3-day running mean (black solid line). (b) Same 3-day running mean series as in (a) but after applying the MODIS AOD coverage (notice the gaps in the time series corresponding to AOD *missing values*). (c) Same as in (b) but after filling the gaps with interpolation. Notice that only days from 150 to 200 are shown in the (a), (b) and (c) time series. (d) Spectral analysis for the time series in (a). (b) Spectral analysis for the time series in (c).

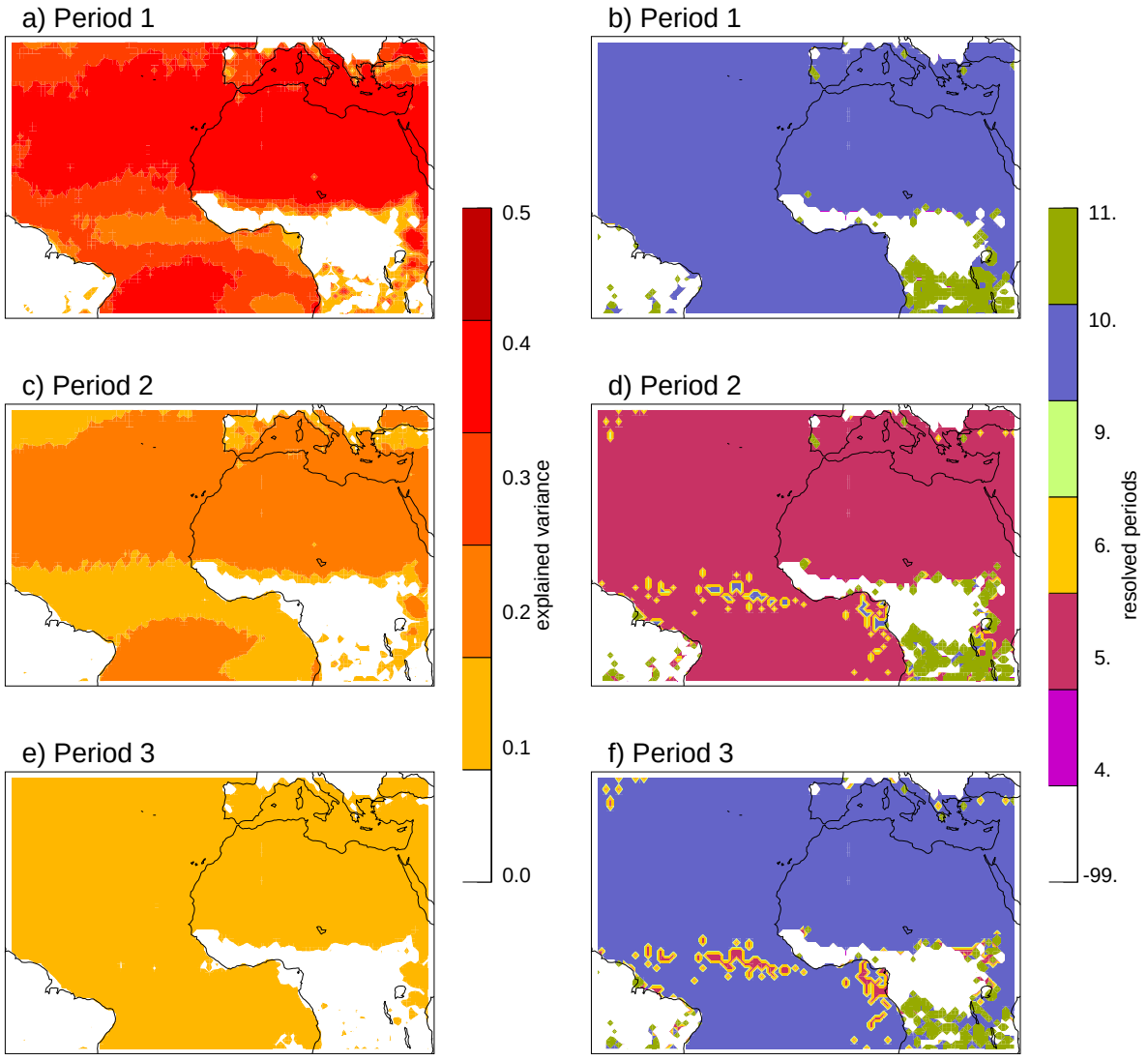

Figure 33: Spatial distribution of the three highest explained variances (left panel) and corresponding periodicity (right panel) for simulated time series in each of the 1° x 1° pixels over the Tropical Atlantic and North Africa regions. The same procedure to test the data aggregation in Fig. 32 was used for each time series and 5- and 10-day periodicity was assumed. The white regions in maps represent areas with missing values in the MODIS-AOD coverage.

APPENDIX B

SIGNIFICANCE OF AEROSOL VARIABILITY MODES USING THE EMPIRICAL MODE DECOMPOSITION TECHNIQUE

Empirical Mode Decomposition (EMD) (Huang et al. 1998) is an adaptive method used to decompose any time series into a set of Intrinsic Mode Function (IMF) components. The set of IMF becomes the basis for representing the data. The decomposition method is adaptive because the definition of the basis function representing the data is based and derived from the data itself and not, as for example Fourier analysis which requires a trigonometric basis (Huang et al. 1998). Because the EMD basis is adaptive, it usually offers a meaningful physical representation of the underlying process based on the local characteristics of the data (Duffy 2004). Also, because the adaptive nature of the basis, there is no need for harmonics; therefore EMD is ideally suited for analyzing data from non-stationary and non-linear processes. We used the EMD method to compare the modes of variability in the aerosol series extracted using the Fourier filter analysis (Chapter 4). In addition, the variability modes were evaluated using a statistical significance test.

The EMD technique consists in a decomposition of the original series through a "sifting" process. The sifting starts with identifying all the local maxima and minima in the original series. The extreme values are then connected using cubic spline lines to form an upper and a lower envelope. The mean of the derived envelope is subtracted from the original series and then, the envelope of the residual is again found using a spline interpolation. The envelope mean is then subtracted from the residual and the process is repeated with a series of iterations. Once the mean of the envelope is close

enough to zero, the first IMF is obtained. Details of the technique and the criterion for the determining the number of iterations are described in Huang et al. (1998; 2008). The first IMF should contain the shortest period of oscillation in the signal, which is then extracted from the original series. The residual of this extraction still contains variability with longer periods and is treated as new data using the same iterative process as described above to obtain an IMF of a higher period. The process is repeated sequentially until all the modes are extracted from the original series.

B.1 Aerosol variability modes using the EMD technique

Figure 34a shows the TOMS-N7T AI daily time series averaged over the test region near the coast of Africa (i.e., 15°N–17°N, 22°W–20°W; box Fig. 2a) used for the composite analysis in Chap. 4. To obtain a representative sample of data, a 3-day running mean was applied to the AI time series similar to the analysis in Chap. 4 and discussed in Appendix A. The Fourier spectrum of this daily time series highlights the annual cycle peak and significant shorter time cycles (Fig. 34b). The EMD technique was applied to the time series in Fig. 34a and only the 1^{st}, 2^{nd} and 7^{th} modes are shown in the lower panels of the same figure. The 1^{st} and 2^{nd} modes correspond to the shortest variability modes having periods around 5 to 6 and 10 to 12 days, respectively (Figs. 34d and 34f). These periods have similar magnitude to the two modes of variability of AEW over the region (see Chap. 4). For illustrative purposes, the 7^{th} mode is shown in Fig. 34g and corresponds to the annual cycle predominant in the original time series (see Chap. 3). The remaining modes (i.e., 3^{rd}, 4^{th}, etc), are not considered in this analysis because they do not represent periodicities related with AEW activity and are outside the scope of the present work. A similar analysis was used on the remaining aerosol dataset (i.e., OMI AI, MODIS-Aqua and -Terra AOD) and Table 3 shows the average periodicity of the 1^{st}, 2^{nd} and 7^{th} modes. Variability periods around 5–6, 10–12 and 360 days, for the corresponding 1^{st}, 2^{nd} and 7^{th} modes,

are repeated for each of the analyzed aerosol satellite datasets. The similitude of the variability modes among datasets confirms that the periods found are representative of the aerosol variability over the region, having similar periodicity as the two modes of AEW and annual cycle that modify the aerosol burden over the Tropical Atlantic region.

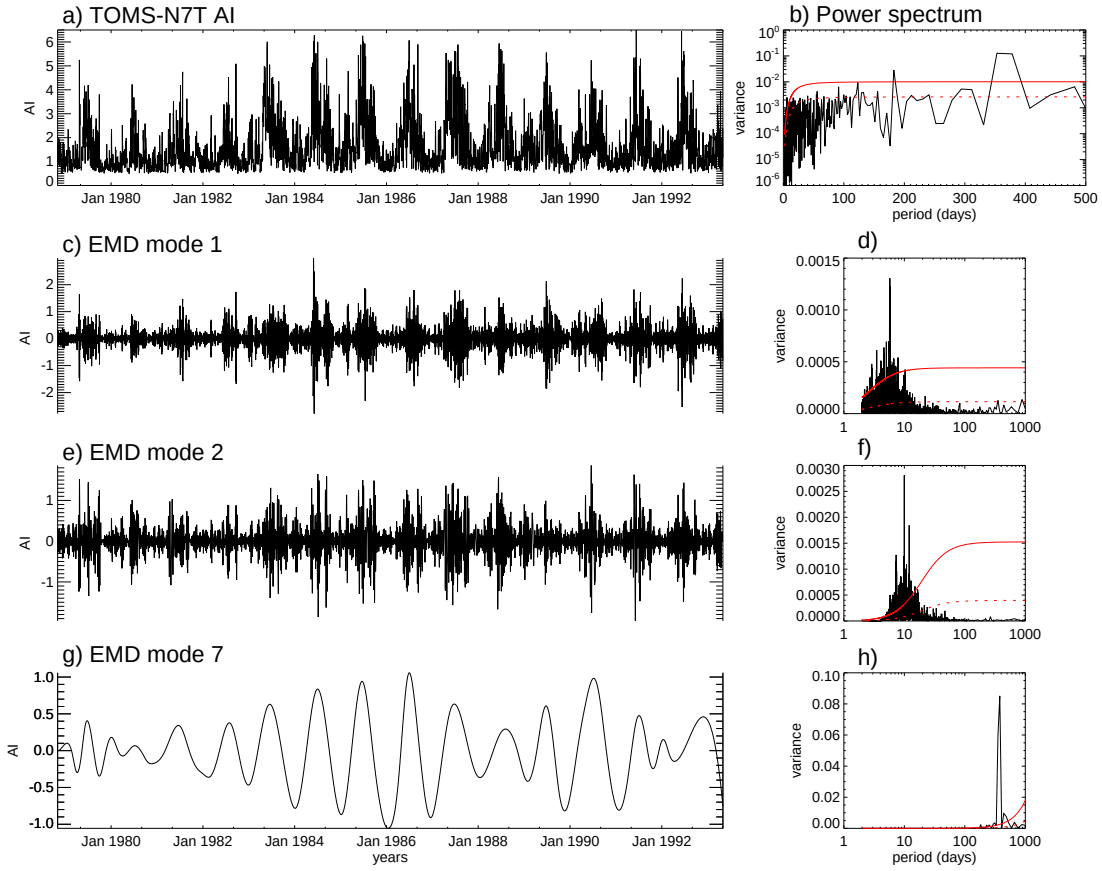

Figure 34: (a) Daily time series of TOMS-N7T AI averaged over a region near the coast of Africa (box Fig. 2a). (b) Fourier power spectrum of time series in (a). IMF time series for the 1^{st} (c), 2^{nd} (e) and 7^{th} (g) modes calculated for the time series in (a). Fourier spectrums for the IMF time series of the 1^{st} (d), 2^{nd} (f) and 7^{th} (h) modes. The continuous red line in each spectrum corresponds to the significance compared with a red noise process with a 95% of confidence level.

To test the statistical significance of the modes of variability of the aerosol time series calculated with the EMD technique, a method described in Coughlin and Tung (2005) was applied. The test is based on a comparison of the energy computed in

Table 3: Average period of variability (in days) in aerosol time series calculated from the different datasets used in this study. The modes of variability were extracted from the calculation of IMF to each time series using the EMD technique. The average period was estimated from the application of a Fourier spectrum to the IMF time series.

Mode	TOMS N7T	OMI	MODIS Terra	MODIS Aqua
1^{st}	5–6	4–5	5–6	5–6
2^{nd}	10–12	10–12	10–12	10–12
7^{th}	360	360	360	360

each IMF to the energy distribution of a red noise process. To perform the test, Monte-Carlo simulations of time series having the same variance as the original series were constructed using an autoregressive model of 1^{st} order. This "red" time series was used to compute IMF series using the EMD technique and the energy of the averaged modes was next compared to the one calculated for the original time series. We compared how different the original IMF modes were from the modes calculated for a red noise process and evaluated the statistical significance. Figure 35 shows the average period and power for the 1^{st}, 2^{nd} and 7^{th} modes of the IMF series calculated using 500 time series generated using Monte-Carlo simulations. The average period and power of the IMF time series modes using TOMS-N7T AI and MODIS-Aqua AOD were compared to those 500 modes (Fig. 35). The statistical significance is given by how different the aerosol modes are from the ones simulated with the red noise process. For this, Coughlin and Tung (2005) suggested a comparison of the calculated aerosol mode with a line displaced +1 standard deviation of the linear square best fit of the simulations. As the modes calculated for the AI and AOD using the EMD technique were different from this line we conclude that they are statistical significant.

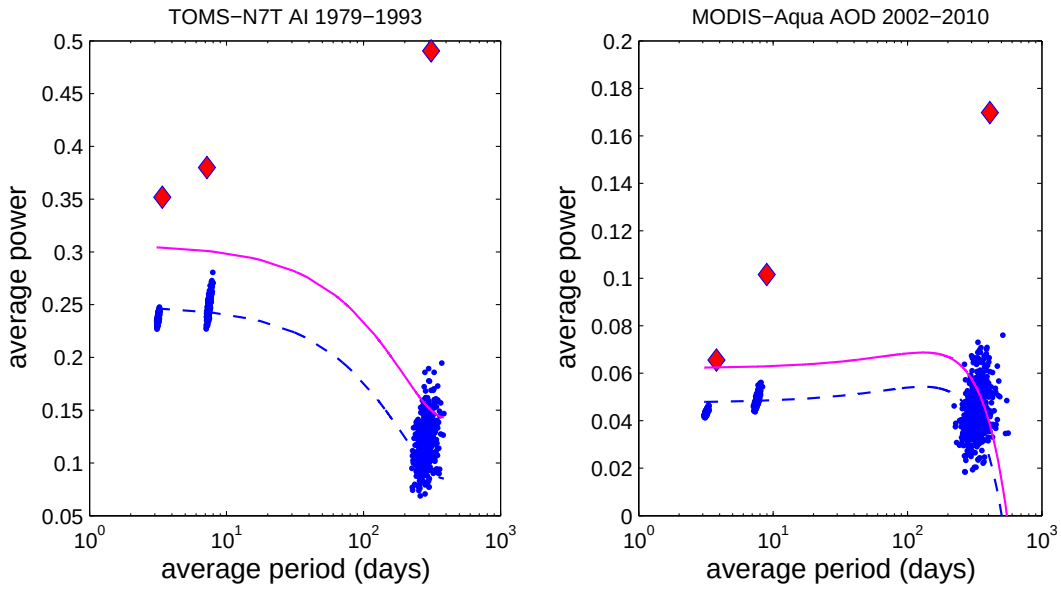

Figure 35: Average power and periods (blue dots) of time series based on Monte-Carlo simulations with equal variance as the IMF time series for the 1^{st}, 2^{nd} and 7^{th} modes presented in Fig. 34, for TOMS-N7T AI (left) and MODIS-Aqua AOD (right) time series. The red diamonds are the averaged modes of variability for the original AI and AOD time series calculated using the EMD technique. The dashed blue line represents a linear least square fit of the Monte-Carlo simulation periods and the red line is one standard deviation from the best fit line to test the significance of the IMF modes.

B.2 Composite analysis

Using the IMF time series calculated with the EMD technique, one can characterize the temporal evolution of aerosols relative to AEW variability in a similar way to the analysis presented in Chapter 4. Positive values greater than +1 standard deviation in the 1^{st} and 2^{nd} IMF time series were selected and the date of the maximum value in each period was chosen as the day 0 to compute the composites. To construct the composites, daily anomalies of gridded TOMS and MODIS data were computed with respect to a 30-day running mean of the daily climatology fields in each of the analyzed periods. For the TOMS daily data, 137 days of maximum AI were found using the IMF time series for the 1^{st} mode and 76 days for the 2^{nd} mode. In similar way, MODIS indicated 67 and 40 days of maximum AOD for the 1^{st} and the 2^{nd}

modes, respectively.

Figure 36 shows a longitude-time plot of TOMS AI and MODIS AOD anomalies for the 1^{st} and 2^{nd} modes calculated from the EMD analysis. Day 0 in each plot represents a maximum in aerosol loading over the reference region. In addition, positive geopotential height anomalies at 700 hPa were plotted in the same figure. Similar to Fig. 11, two westward propagating modes of aerosol loading are evident in both datasets, one with a period of near 5-6 days (for the 1^{st} mode) and another with a period near 10-12 days (for the 2^{nd} mode). Those modes have similar values of the characteristic wave speed and period to those calculated using the 5-15 and 10-30 day bands using the Fourier filter analysis (see Chap. 4). There is also good relationship between positive 700 hPa geopotential height anomalies with positive aerosol anomalies and negative heights with negative aerosol anomalies, as concluded in Chap. 4. In summary, periods calculated using the EMD technique also show the two distinctive modes of variability in the aerosol datasets matching the wave speed of AEW regimes affecting the dust variability in the Tropical Atlantic region.

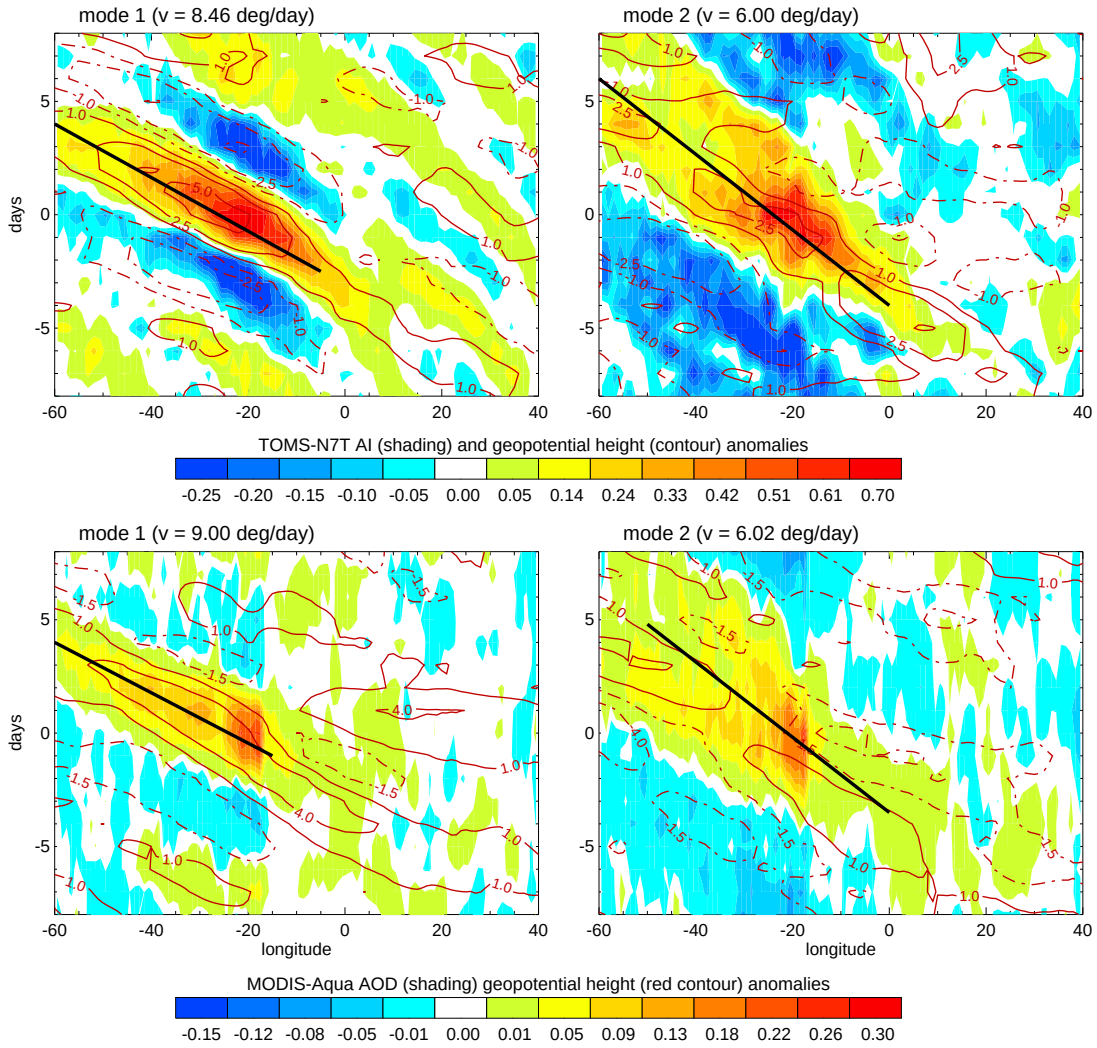

Figure 36: Longitude-time plots of aerosol (shading, relative to the color palette) and geopotential height (contours in [m], continuous line positive values) anomalies averaged between 15°N and 20°N. Upper panel corresponds to TOMS-AI variability composites using the 1^{st} (left) and 2^{nd} (right) modes from the EMD analysis. Lower panel corresponds to MODIS-AOD composites using the 1^{st} (left) and 2^{nd} (right) modes. For each plot a black solid line represents the mean average propagation of the positive aerosol anomalies and the speed of this propagation is indicated at the top of each diagram.

REFERENCES

[1] Agudelo, P. A., and J. A. Curry, 2004: Analysis of spatial distribution in tropospheric temperature trends. *Geophys. Res. Letters*, 31, L22207.

[2] Agudelo, P. A., C. D. Hoyos, P. J. Webster, and J. A. Curry, 2009: Application of a serial extended forecast experiment using the ECMWF model to interpret the predictive skill of tropical intraseasonal variability. *Climate Dyn.*, 32(6), 855-872.

[3] Al-Saadi, J., and Coauthors, 2005: Improving national air quality forecasts with satellite aerosol observations. *Bull. Amer. Meteor. Soc.*, 86(9), 1249-1261.

[4] Albrecht, B. A., 1989: Aerosols, Cloud Microphysics, and Fractional Cloudiness. *Science*, 245, 1227-1230.

[5] Bao, Z. H., Z. P. Wen, and R. G. Wu, 2009: Variability of aerosol optical depth over east Asia and its possible impacts. *J. Geophys. Res. Atmos.*, 114, 13.

[6] Barkan, J., H. Kutiel, P. Alpert, and P. Kishcha, 2004: Synoptics of dust intrusion days from the African continent into the Atlantic Ocean. *J. Geophys. Res. Atmos.*, 109(D8), 9.

[7] Berrisford, P., D. Dee, K. Fielding, M. Fuentes, P. Kallberg, S. Kobayashi, and S. Uppala, 2009: *The ERA-Interim Archive*. ERA Report Series. European Center for Medium Range Weather Forecast, Shinfield Park, Reading, UK. 16 pp.

[8] Bollasina, M., S. Nigam, and K. M. Lau, 2008: Absorbing aerosols and summer monsoon evolution over South Asia: An observational portrayal. *J. Climate*, 21(13), 3221-3239.

[9] Burpee, R. W., 1972: Origin And Structure Of Easterly Waves in Lower Troposphere Of North Africa. *J. Atmos. Sci.*, 29(1), 77-90.

[10] Cakmur, R. V., R. L. Miller, and I. Tegen, 2001: A comparison of seasonal and interannual variability of soil dust aerosols over the Atlantic Ocean as inferred by the TOMS AI and AVHRR AOT retrievals. *J. Geophys. Res. Atmos.*, 106(D16), 18287-18303.

[11] Carlson, T. N., 1969: Some Remarks On African Disturbances And Their Progress Over Tropical Atlantic. *Mon. Wea. Rev.*, 97(10), 716-726.

[12] Carlson, T. N., and J. M. Prospero, 1972: The Large-Scale Movement of Saharan Air Outbreaks over the Northern Equatorial Atlantic. *J. Appl. Meteor.*, 11(2), 283-297.

[13] Charlson, R. J., S. E. Schwartz, J. M. Hales, R. D. Cess, J. A. Coakley, J. E. Hansen, and D. J. Hofmann, 1992: Climate Forcing by Anthropogenic Aerosols. *Science*, 255(5043), 423-430.

[14] Chiapello, I., J. M. Prospero, J. R. Herman, and N. C. Hsu, 1999: Detection of mineral dust over the North Atlantic Ocean and Africa with the Nimbus 7 TOMS. *J. Geophys. Res. Atmos.*, 104(D8), 9277-9291.

[15] Chin, M., A. Chu, R. Levy, L. Remer, Y. Kaufman, B. Holben, T. Eck, P. Ginoux, and Q. X. Gao, 2004: Aerosol distribution in the Northern Hemisphere during ACE-Asia: Results from global model, satellite observations, and Sun photometer measurements. *J. Geophys. Res.*, 109(D23), 15.

[16] Chin, M., P. Ginoux, S. Kinne, O. Torres, B. N. Holben, B. N. Duncan, R. V. Martin, J. A. Logan, A. Higurashi, and T. Nakajima, 2002: Tropospheric aerosol optical thickness from the GOCART model and comparisons with satellite and Sun photometer measurements. *J. Atmos. Sci.*, 59(3), 461-483.

[17] Coakley, J., and R. Cess, 1985: Response Of The NCAR Community Climate Model To The Radiative Forcing By The Naturally-Occurring Tropospheric Aerosol. *J. Atmos. Sci.*, 42(16), 1677-1692.

[18] Colarco, P., A. da Silva, M. Chin, and T. Diehl, 2010: Online simulations of global aerosol distributions in the NASA GEOS-4 model and comparisons to satellite and ground-based aerosol optical depth. *J. Geophys. Res. Atmos.*, 115, D14207.

[19] Coughlin, K., and K. K. Tung, 2005: Empirical mode decomposition and climate variability. *Hilbert-Huang Transform and Its Applications*, N. E. Huang, and S. S. P. Shen, Eds., World Scientific Publ. Co Pte Ltd, 149-165.

[20] Diedhiou, A., S. Janicot, A. Viltard, and P. de Felice, 1998: Evidence of two regimes of easterly waves over West Africa and the tropical Atlantic. *Geophys. Res. Letters*, 25(15), 2805-2808.

[21] Diedhiou, A., S. Janicot, A. Viltard, P. de Felice, and H. Laurent, 1999: Easterly wave regimes and associated convection over West Africa and tropical Atlantic: results from the NCEP/NCAR and ECMWF reanalyses. *Climate Dyn.*, 15(11), 795-822.

[22] Diner, D. J., and Coauthors, 1998: Multi-angle Imaging SpectroRadiometer (MISR) - Instrument description and experiment overview. *IEEE Tran. Geosc. Remo. Sens.*, 36(4), 1072-1087.

[23] Duffy, D. G., 2004: The application of Hilbert-Huang transforms to meteorological datasets. *J. Atmos. Oceanic Technol.*, 21(4), 599-611.

[24] Dunion, J. P., and C. S. Velden, 2004: The impact of the Saharan air layer on Atlantic tropical cyclone activity. *Bull. Amer. Meteor. Soc.*, 85(3), 353-365.

[25] Eva, H., and E. F. Lambin, 1998: Remote sensing of biomass burning in tropical regions: Sampling issues and multisensor approach. *Remote Sens. Environm.*, 64(3), 292-315.

[26] Evan, A. T., D. J. Vimont, A. K. Heidinger, J. P. Kossin, and R. Bennartz, 2009: The Role of Aerosols in the Evolution of Tropical North Atlantic Ocean Temperature Anomalies. *Science*, 324(5928), 778-781.

[27] Foltz, G. R., and M. J. McPhaden, 2008: Impact of Saharan dust on tropical North Atlantic SST. *J. Climate*, 21(19), 5048-5060.

[28] Gao, B., and Y. Kaufman, 2003: Water vapor retrievals using Moderate Resolution Imaging Spectroradiometer (MODIS) near-infrared channels. *J. Geophys. Res. Atmos.*, 108(D13), 4389.

[29] Gao, H., and R. Washington, 2009: The spatial and temporal characteristics of TOMS AI over the Tarim Basin, China. *Atmos. Environ.*, 43(5), 1106-1115.

[30] Geogdzhayev, I. V., M. I. Mishchenko, W. B. Rossow, B. Cairns, and A. A. Lacis, 2002: Global two-channel AVHRR retrievals of aerosol properties over the ocean for the period of NOAA-9 observations and preliminary retrievals using NOAA-7 and NOAA-11 data. *J. Atmos. Sci.*, 59(3), 262-278.

[31] George, J. P., L. Harenduprakash, and M. Mohan, 2008: Multi year changes of Aerosol Optical Depth in the monsoon region of the Indian Ocean since 1986 as seen in the AVHRR and TOMS data. *Anna. Geophys.*, 26(1), 7-11.

[32] Gislason, S. R., and Coauthors, 2011: Characterization of Eyjafjallajokull volcanic ash particles and a protocol for rapid risk assessment. *Proc. Natl. Acad. Sci. U. S. A.*, 108(18), 7307-7312.

[33] Hansen, J., M. Sato, and R. Ruedy, 1997: Radiative forcing and climate response. *J. Geophys. Res. Atmos.*, 102(D6), 6831-6864.

[34] Haywood, J., and O. Boucher, 2000: Estimates of the direct and indirect radiative forcing due to tropospheric aerosols: A review. *Rev. Geophys.*, 38(4), 513-543.

[35] Haywood, J. M., V. Ramaswamy, and B. J. Soden, 1999: Tropospheric aerosol climate forcing in clear-sky satellite observations over the oceans. *Science*, 283(5406), 1299-1303.

[36] Heinold, B., and Coauthors, 2009: Regional Saharan dust modelling during the SAMUM 2006 campaign. *Tellus B*, 61(1), 307-324.

[37] Herman, J. R., P. K. Bhartia, O. Torres, C. Hsu, C. Seftor, and E. Celarier, 1997: Global distribution of UV-absorbing aerosols from Nimbus 7/TOMS data. *J. Geophys. Res. Atmos.*, 102(D14), 16911-16922.

[38] Hirsch, R. M., J. R. Slack, and R. A. Smith, 1982: Techniques Of Trend Analysis for Monthly Water-Quality Data. *Water Reso. Res.*, 18(1), 107-121.

[39] Holben, B. N., and Coauthors, 2001: An emerging ground-based aerosol climatology: Aerosol optical depth from AERONET. *J. Geophys. Res. Atmos.*, 106(D11), 12067-12097.

[40] Hollingsworth, A., and Coauthors, 2008: Toward a monitoring and forecasting system for atmospheric composition: The GEMS project. *Bull. Amer. Meteor. Soc.*, 89(8), 1147-.

[41] Hoyos, C. D., 2006: *Intraseasonal variability processes, predictability and prospects for prediction*. Ph. D. Thesis. Georgia Institute of Technology, Atlanta, GA., 188 pp.

[42] Hsu, N. C., S. C. Tsay, M. D. King, and J. R. Herman, 2004: Aerosol properties over bright-reflecting source regions. *IEEE Tran. Geosc. Remo. Sens.*, 42(3), 557-569.

[43] Hsu, N. C., and Coauthors, 1996: Detection of biomass burning smoke from TOMS measurements. *Geophys. Res. Letters*, 23(7), 745-748.

[44] Huang, J. F., C. D. Zhang, and J. M. Prospero, 2010: African dust outbreaks: A satellite perspective of temporal and spatial variability over the tropical Atlantic Ocean. *J. Geophys. Res. Atmos.*, 115, D05202.

[45] Huang, N. E., and Z. H. Wu, 2008: A review on Hilbert-Huang transform: method and its applications to geophysical studies. *Rev. Geophys.*, 46, RG2006.

[46] Huang, N. E., and Coauthors, 1998: The empirical mode decomposition and the Hilbert spectrum for nonlinear and non-stationary time series analysis. *Proc. R. Soc. London Ser. A.*, 454, 903-995.

[47] Huffman, G. J., and Coauthors, 2001: Global precipitation at one-degree daily resolution from multisatellite observations. *J. Hydrometeor.*, 2, 36-50.

[48] Huneeus, N., Schulz, M., Balkanski, Y., Griesfeller, J., Kinne, S., Prospero, J., Bauer, S., Boucher, O., Chin, M., Dentener, F., Diehl, T., Easter, R., Fillmore, D., Ghan, S., Ginoux, P., Grini, A., Horowitz, L., Koch, D., Krol, M. C., Landing, W., Liu, X., Mahowald, N., Miller, R., Morcrette, J.-J., Myhre, G., Penner, J. E., Perlwitz, J., Stier, P., Takemura, T., and Zender, C.: Global dust model intercomparison in AeroCom phase I. *Atmos. Chem. Phys. Discuss.*, 10, 23781-23864

[49] Husar, R. B., J. M. Prospero, and L. L. Stowe, 1997: Characterization of tropospheric aerosols over the oceans with the NOAA advanced very high resolution radiometer optical thickness operational product. *J. Geophys. Res. Atmos.*, 102(D14), 16889-16909.

[50] IPCC, 2007: *Climate Change 2007: The Physical Science Basis*. Contribution of Working Group I to the Fourth Assessment Report of the Intergovernmental Panel on Climate Change. Cambridge University Press, 996 pp.

[51] Jacobson, M. Z., 1997: Development and application of a new air pollution modeling system .2. Aerosol module structure and design. *Atmos. Environm.*, 31(2), 131-144.

[52] Jeong, M. J., and Z. Q. Li, 2005: Quality, compatibility, and synergy analyses of global aerosol products derived from the advanced very high resolution radiometer and Total Ozone Mapping Spectrometer. *J. Geophys. Res.*, 110, D10S08.

[53] Jickells, T. D., and Coauthors, 2005: Global iron connections between desert dust, ocean biogeochemistry, and climate. *Science*, 308(5718), 67-71.

[54] Jones, C., N. Mahowald, and C. Luo, 2003: The role of easterly waves on African desert dust transport. *J. Climate*, 16(22), 3617-3628.

[55] Jones, C., N. Mahowald, and C. Luo, 2004a: Observational evidence of African desert dust intensification of easterly waves. *Geophys. Res. Letters*, 31, L17208.

[56] Jones, C., L. M. V. Carvalho, R. W. Higgins, D. E. Waliser, and J. K. E. Schemm, 2004b: A statistical forecast model of tropical intraseasonal convective anomalies. *J. Climate*, 17, 2078-2095.

[57] Jury, M. R., and M. J. Santiago, 2010: Composite analysis of dust impacts on African easterly waves in the Moderate Resolution Imaging Spectrometer era. *J. Geophys. Res. Atmos.*, 115, D16213.

[58] Kahn, R. A., B. J. Gaitley, J. V. Martonchik, D. J. Diner, K. A. Crean, and B. Holben, 2005: Multiangle Imaging Spectroradiometer (MISR) global aerosol optical depth validation based on 2 years of coincident Aerosol Robotic Network (AERONET) observations. *J. Geophys. Res. Atmos.*, 110, D10S04.

[59] Kahn, R. A., and Coauthors, 2009: MISR Aerosol Product Attributes and Statistical Comparisons With MODIS. *IEEE Tran. Geosc. Remo. Sens.*, 47(12), 4095-4114.

[60] Kalashnikova, O. V., and R. Kahn, 2006: Ability of multiangle remote sensing observations to identify and distinguish mineral dust types: 2. Sensitivity over dark water. *J. Geophys. Res. Atmos.*, 111, D11207.

[61] Kang, I. S., and H. M. Kim, 2010: Assessment of MJO Predictability for Boreal Winter with Various Statistical and Dynamical Models. *J. Climate*, 23(9), 2368-2378.

[62] Karyampudi, V. M., and T. N. Carlson, 1988: Analysis And Numerical Simulations Of The Saharan Air Layer And Its Effect On Easterly Wave Disturbances. *J. Atmos. Sci.*, 45(21), 3102-3136.

[63] Karyampudi, V. M., and Coauthors, 1999: Validation of the Saharan dust plume conceptual model using lidar, Meteosat, and ECMWF data. *Bull. Amer. Meteor. Soc.*, 80(6), 1045-1075.

[64] Kaufman, Y. J., D. Tanré, and O. Boucher, 2002: A satellite view of aerosols in the climate system. *Nature*, 419(6903), 215-223.

[65] Kaufman, Y. J., D. Tanré, L. A. Remer, E. F. Vermote, A. Chu, and B. N. Holben, 1997: Operational remote sensing of tropospheric aerosol over land from EOS moderate resolution imaging spectroradiometer. *J. Geophys. Res. Atmos.*, 102(D14), 17051-17067.

[66] Kim, H. M., and P. J. Webster, 2010: Extended-range seasonal hurricane forecasts for the North Atlantic with a hybrid dynamical-statistical model. *Geophys. Res. Letters*, 37, L21705.

[67] King, M. D., Y. J. Kaufman, D. Tanré, and T. Nakajima, 1999: Remote sensing of tropospheric aerosols from space: Past, present, and future. *Bull. Amer. Meteor. Soc.*, 80(11), 2229-2259.

[68] Kinne, S., Schulz, M., Textor, C., Guibert, S., Balkanski, Y., Bauer, S. E., Berntsen, T., Berglen, T. F., Boucher, O., Chin, M., Collins, W., Dentener, F., Diehl, T., Easter, R., Feichter, J., Fillmore, D., Ghan, S., Ginoux, P., Gong, S., Grini, A., Hendricks, J., Herzog, M., Horowitz, L., Isaksen, I., Iversen, T., Kirkevg, A., Kloster, S., Koch, D., Kristjansson, J. E., Krol, M., Lauer, A., Lamarque, J. F., Lesins, G., Liu, X., Lohmann, U., Montanaro, V., Myhre, G., Penner, J., Pitari, G., Reddy, S., Seland, O., Stier, P., Takemura, T., and Tie, X.: 2006. An AeroCom initial assessment optical properties in aerosol component modules of global models. *Atmos. Chem. Phys.*, 6, 1815-1834.

[69] Kishcha, P., B. Starobinets, and P. Alpert, 2007: Latitudinal variations of cloud and aerosol optical thickness trends based on MODIS satellite data. *Geophys. Res. Letters*, 34, L05810.

[70] Kiss, P., I. M. Janosi, and O. Torres, 2007: Early calibration problems detected in TOMS Earth-Probe aerosol signal. *Geophys. Res. Letters*, 34, L07803.

[71] Knippertz, P., and M. C. Todd, 2010: The central west Saharan dust hot spot and its relation to African easterly waves and extratropical disturbances. *J. Geophys. Res. Atmos.*, 115, D12117.

[72] Koren, I., L. A. Remer, and K. Longo, 2007: Reversal of trend of biomass burning in the Amazon. *Geophys. Res. Letters*, 34, L20404.

[73] Koren, I., L. A. Remer, K. Longo, F. Brown, and R. Lindsey, 2009: Reply to comment by W. Schroeder et al. on "Reversal of trend of biomass burning in the Amazon". *Geophys. Res. Letters*, 36, L03807.

[74] Lau, K. M., and K. M. Kim, 2006: Observational relationships between aerosol and Asian monsoon rainfall, and circulation. *Geophys. Res. Letters*, 33, L21810.

[75] Lau, K. M., and K. M. Kim, 2007: Cooling of the Atlantic by Saharan dust. *Geophys. Res. Letters*, 34, L23811.

[76] Levy, R. C., G. G. Leptoukh, R. Kahn, V. Zubko, A. Gopalan, and L. A. Remer, 2009: A Critical Look at Deriving Monthly Aerosol Optical Depth From Satellite Data. *IEEE Tran. Geosc. Remo. Sens.*, 47(8), 2942-2956.

[77] Leptoukh, G. G., 2010: Towards Consistent Characterization of Quality and Uncertainty in Multi-sensor Aerosol Level 3 Satellite Data. Abstract A21J-03 presented at *2010 Fall Meeting*, AGU, San Francisco, CA., 13-17 December

[78] Li, J., B. E. Carlson, and A. A. Lacis, 2009: A study on the temporal and spatial variability of absorbing aerosols using Total Ozone Mapping Spectrometer and Ozone Monitoring Instrument Aerosol Index data. *J. Geophys. Res. Atmos.*, 114, D09213.

[79] Liebmann, B., and C. A. Smith, 1996: Description of a complete (interpolated) outgoing longwave radiation dataset. *Bull. Amer. Meteor. Soc.*, 77(6), 1275-1277.

[80] Liu, L., and M. I. Mishchenko, 2008: Toward unified satellite climatology of aerosol properties: Direct comparisons of advanced level 2 aerosol products. *J. Quant. Spectrosc. Rad. Trans.*, 109(14), 2376-2385.

[81] Mangold, A., and Coauthors, 2011: Aerosol analysis and forecast in the European Centre for Medium-Range Weather Forecasts Integrated Forecast System: 3. Evaluation by means of case studies. *J. Geophys. Res. Atmos.*, 116, D03302.

[82] Massie, S. T., O. Torres, and S. J. Smith, 2004: Total Ozone Mapping Spectrometer (TOMS) observations of increases in Asian aerosol in winter from 1979 to 2000. *J. Geophys. Res. Atmos.*, 109, D18211.

[83] Miller, R. L., and I. Tegen, 1998: Climate response to soil dust aerosols. *J. Climate*, 11(12), 3247-3267.

[84] Mishchenko, M. I., I. V. Geogdzhayev, L. Liu, A. A. Lacis, B. Cairns, and L. D. Travis, 2009: Toward unified satellite climatology of aerosol properties: What do fully compatible MODIS and MISR aerosol pixels tell us? *J. Quant. Spectrosc. Rad. Trans.*, 110(6-7), 402-408.

[85] Mishchenko, M. I., and Coauthors, 2007: Past, present, and future of global aerosol climatologies derived from satellite observations: A perspective. *J. Quant. Spectrosc. Rad. Trans.*, 106(1-3), 325-347.

[86] Molnar, P., and J. A. Ramirez, 2001: Recent trends in precipitation and streamflow in the Rio Puerco Basin. *J. Climate*, 14(10), 2317-2328.

[87] Papadimas, C. D., N. Hatzianastassiou, N. Mihalopoulos, X. Querol, and I. Vardavas, 2008: Spatial and temporal variability in aerosol properties over the Mediterranean basin based on 6-year (2000-2006) MODIS data. *J. Geophys. Res. Atmos.*, 113, D11205.

[88] Philipona, R., K. Behrens, and C. Ruckstuhl, 2009: How declining aerosols and rising greenhouse gases forced rapid warming in Europe since the 1980s. *Geophys. Res. Letters*, 36, L02806.

[89] Prospero, J. M., and T. N. Carlson, 1972: Vertical and Areal Distribution of Saharan Dust Over Western Equatorial North-Atlantic Ocean. *J. Geophys. Res.*, 77(27), 5255-5265.

[90] Prospero, J. M., P. Ginoux, O. Torres, S. E. Nicholson, and T. E. Gill, 2002: Environmental characterization of global sources of atmospheric soil dust identified with the Nimbus 7 Total Ozone Mapping Spectrometer (TOMS) absorbing aerosol product. *Rev. Geophys.*, 40(1), 31.

[91] Prospero, J. M., W. M. Landing, and M. Schulz, 2010: African dust deposition to Florida: Temporal and spatial variability and comparisons to models. *J. Geophys. Res. Atmos.*, 115, D13304.

[92] Ramanathan, V., and Coauthors, 2001: Indian Ocean Experiment: An integrated analysis of the climate forcing and effects of the great Indo-Asian haze. *J. Geophys. Res.*, 106(D22), 28371-28398.

[93] Reed, R. J., D. C. Norquist, and E. E. Recker, 1977: Structure And Properties Of African Wave Disturbances As Observed During Phase Iii Of Gate. *Mon. Wea. Rev.*, 105(3), 317-333.

[94] Remer, L. A., and Coauthors, 2008: Global aerosol climatology from the MODIS satellite sensors. *J. Geophys. Res. Atmos.*, 113, D14S07.

[95] Remer, L. A., and Coauthors, 2005: The MODIS aerosol algorithm, products, and validation. *J. Atmos. Sci.*, 62(4), 947-973.

[96] Reynolds, R. W., T. M. Smith, C. Liu, D. B. Chelton, K. S. Casey, and M. G. Schlax, 2007: Daily high-resolution-blended analyses for sea surface temperature. *J. Climate*, 20(22), 5473-5496.

[97] Seftor, C. J., and Coauthors, 1997: Detection of volcanic ash clouds from Nimbus 7/total ozone mapping spectrometer. *J. Geophys. Res.*, 102(D14), 16749-16759.

[98] Shao, Y. P., and Coauthors, 2003: Northeast Asian dust storms: Real-time numerical prediction and validation. *J. Geophys. Res.*, 108(D22), 4691.

[99] Sokolik, I. N., D. M. Winker, G. Bergametti, D. A. Gillette, G. Carmichael, Y. J. Kaufman, L. Gomes, L. Schuetz, and J. E. Penner, 2001: Introduction to special section: Outstanding problems in quantifying the radiative impacts of mineral dust. *J. Geophys. Res. Atmos.*, 106(D16), 18015-18027.

[100] Stephens, G. L., 2005: Cloud feedbacks in the climate system: A critical review. *J. Climate*, 18(2), 237-273.

[101] Streets, D. G., and Coauthors, 2009: Anthropogenic and natural contributions to regional trends in aerosol optical depth, 1980-2006. *J. Geophys. Res.*, 114, D00D18.

[102] Swap, R., M. Garstang, S. Greco, R. Talbot, and P. Kallberg, 1992: Saharan Dust In The Amazon Basin. *Tellus B*, 44, 133-149.

[103] Tanré, D., Y. J. Kaufman, M. Herman, and S. Mattoo, 1997: Remote sensing of aerosol properties over oceans using the MODIS/EOS spectral radiances. *J. Geophys. Res.*, 102(D14), 16971-16988.

[104] Tegen, I., and R. Miller, 1998: A general circulation model study on the interannual variability of soil dust aerosol. *J. Geophys. Res.*, 103(D20), 25975-25995.

[105] Tian, B. J., and Coauthors, 2008: Does the Madden-Julian oscillation influence aerosol variability? *J. Geophys. Res. Atmos.*, 113, D12215.

[106] Torres, O., J. R. Herman, P. K. Bhartia, and Z. Ahmad, 1995: Properties Of Mount-Pinatubo Aerosols As Derived From Nimbus-7 Total Ozone Mapping Spectrometer Measurements. *J. Geophys. Res.*, 100(D7), 14043-14055.

[107] Torres, O., P. K. Bhartia, J. R. Herman, Z. Ahmad, and J. Gleason, 1998: Derivation of aerosol properties from satellite measurements of backscattered ultraviolet radiation: Theoretical basis. *J. Geophys. Res.*, 103(D14), 17099-17110.

[108] Torres, O., P. K. Bhartia, J. R. Herman, A. Sinyuk, P. Ginoux, and B. Holben, 2002: A long-term record of aerosol optical depth from TOMS observations and comparison to AERONET measurements. *J. Atmos. Sci.*, 59(3), 398-413.

[109] Torres, O., and Coauthors, 2007: Aerosols and surface UV products from Ozone Monitoring Instrument observations: An overview. *J. Geophys. Res. Atmos.*, 112, D24S47.

[110] Torres, O., Z. Chen, H. Jethva, C. Ahn, S. R. Freitas, and P. K. Bhartia, 2010: OMI and MODIS observations of the anomalous 2008-2009 Southern Hemisphere biomass burning seasons. *Atmos. Chem. Phys.*, 10(8), 3505-3513.

[111] Twomey, S. A., 1977: The influence of pollution on the short-wave albedo of clouds. *J. Atmos. Sci.* 34, 11491152.

[112] Twomey, S. A., M. Piepgrass, and T. L. Wolfe, 1984: An Assessment Of The Impact Of Pollution On Global Cloud Albedo. *Tellus B*, 36(5), 356-366.

[113] Uppala, S. M., and Coauthors, 2005: The ERA-40 re-analysis. *Quart. J. Roy. Meteor. Soc.*, 131(612), 2961-3012.

[114] Viltard, A., P. deFelice, and J. Oubuih, 1997: Comparison of the African and the 6-9 day wave-like disturbance patterns over West-Africa and the tropical Atlantic during summer 1985. *Meteor. Atmos. Phys.*, 62(1-2), 91-99.

[115] Wang, K. C., R. E. Dickinson, and S. L. Liang, 2009: Clear Sky Visibility Has Decreased over Land Globally from 1973 to 2007. *Science*, 323(5920), 1468-1470.

[116] Washington, R., and M. C. Todd, 2005: Atmospheric controls on mineral dust emission from the Bodele Depression, Chad: The role of the low level jet. *Geophys. Res. Letters*, 32, L17701.

[117] Washington, R., M. C. Todd, G. Lizcano, I. Tegen, C. Flamant, I. Koren, P. Ginoux, S. Engelstaedter, C. S. Bristow, C. S. Zender, A. S. Goudie, A. Warren, and J. M. Prospero: 2006. Links between topography, wind, deflation, lakes and dust: The case of the Bodele Depression, Chad. *Geophys. Res. Letters*, 33(9), L09401

[118] Webster, P. J., and Coauthors, 2010: Extended-Range Probabilistic Forecasts Of Ganges and Brahmaputra Floods in Bangladesh. *Bull. Amer. Meteor. Soc.*, 91(11), 1493-1514.

[119] Westphal, D. L., C. A. Curtis, M. Liu, and A. L. Walker, 2009: Operational Aerosol and Dust Storm Forecasting. *Wmo/Geo Expert Meeting on an International Sand and Dust Storm Warning System*, J. C. Perez, and J. M. Baldasano, Eds., IOP Publishing Ltd. 6 pp.

[120] Wild, M., 2009: Global dimming and brightening: A review. *J. Geophys. Res. Atmos.*, 114, D00D16.

[121] Wilks, D. S., 2006: *Statistical methods in the atmospheric sciences*. International Geophysics Series, 2nd ed., Academic Press. 627 pp.

[122] Winker, D. M., and Coauthors, 2009: Overview of the CALIPSO Mission and CALIOP Data Processing Algorithms. *J. Atmos. Oceanic Technol.*, 26(11), 2310-2323.

[123] Xie, J. X., and X. G. Xia, 2008: Long-term trend in aerosol optical depth from 1980 to 2001 in north China. *Particuology*, 6(2), 106-111.

[124] Yu, H. B., R. E. Dickinson, M. Chin, Y. J. Kaufman, B. N. Holben, I. V. Geogdzhayev, and M. I. Mishchenko, 2003: Annual cycle of global distributions of aerosol optical depth from integration of MODIS retrievals and GOCART model simulations. *J. Geophys. Res.*, 108(D3), 4128.

[125] Zhang, J., and J. S. Reid, 2010: A decadal regional and global trend analysis of the aerosol optical depth using a data-assimilation grade over-water MODIS and Level 2 MISR aerosol products. *Atmos. Chem. Phys.*, 10(22), 10949-10963.

[126] Zhao, T. X. P., and Coauthors, 2008: Study of long-term trend in aerosol optical thickness observed from operational AVHRR satellite instrument. *J. Geophys. Res. Atmos.*, 113, D07201.